Mitigation of Hot Electrons from Laser-Plasma Instabilities in Laser-Generated X-Ray Sources

by

Jeffrey R. Fein

A dissertation submitted in partial fulfillment
of the requirements for the degree of
Doctor of Philosophy
(Nuclear Engineering and Radiological Sciences)
in the University of Michigan
2017

Doctoral Committee:

Professor James P. Holloway, Co-chair
Professor R. Paul Drake, Co-chair
Associate Research Scientist Paul A. Keiter
Associate Professor Alec G.R. Thomas
Assistant Professor Louise Willingale

Dedication

To José Luis Osorio

ACKNOWLEDGMENTS

The work presented in this thesis would not have been possible without the contributions and unique support by many individuals. I first would like to express sincere gratitude to my advisor James Holloway for his patience, advice and support throughout my career at Michigan. I very much enjoyed our meetings over the years and appreciate greatly his enthusiasm and insightfulness therein. I am also grateful to my co-advisor, Paul Drake who provided me the many experimental and collaborative opportunities that made this thesis possible, as well as for his invaluable, critical feedback on the work I have produced throughout. In addition, I would like to thank Paul Keiter for his guidance in both designing and carrying out experimental campaigns on the OMEGA and Titan laser facilities. Carolyn Kuranz was also a valuable mentor during this time. Furthermore, I would like to acknowledge my committee, consisting of the first three indivuals as well as Alec Thomas and Louise Willingale, for taking the time to critically evaluate the work presented in this thesis.

Sallee Klein and Rob Gillespie provided key experimental support in the way of target design and fabrication. I appreciate their flexibility and inventiveness to meet my experimental needs. Jan Beltran provided much appreciated administrative support.

Several past mentors helped me along my path to Michigan, including Steve Dytman at the University of Pittsburgh and Erik Brubaker at Sandia.

I will remember much of my time in Ann Arbor through my enriching interactions with many friends and colleagues, including Pat Belancourt, Steven Brown, Josh Davis, Archis Joglekar, Will Koehler, Mario Manuel, Alex Rasmus, Michael Streicher, Matt Trantham and Willow Wan. Many of our discussions led to key insights into this work.

I owe a great deal to my parents, Rich and Ruthellen, who have helped motivate me and have taken a serious interest in my work over the years. I am very fortunate for their support in nearly all aspects of my life. I'm especially indebted to my fiancé, Miranda, for her love and encouragement throughout our time in Michigan, and for making fun of all my scribbling.

*This work was funded by the National Science Foundation Graduate Research Fellowship Program, the Defense Threat Reduction Agency, and multiple contracts through the National Nuclear Security Agency and the DOE Office of Fusion Energy Sciences.

TABLE OF CONTENTS

Dedication . . . . **ii**

Acknowledgments . . . . **iii**

List of Figures . . . . **vi**

List of Abbreviations . . . . **xii**

Abstract . . . . **xiv**

Chapter

1 Introduction **1**

- 1.1 Physical Picture of Laser Plasmas 2
- 1.2 High-Energy-Density Physics and Laboratory Astrophysics 5
- 1.3 Laser-produced x-ray sources 7
  - 1.3.1 X-ray Backlighting Techniques 8
- 1.4 Inertial Confinement Fusion 14
- 1.5 Laser-plasma instabilities and hot electrons 16
- 1.6 High-Energy-Density Facilities 19
- 1.7 Contributions by the author 21
- 1.8 Description of Subsequent Chapters 22

2 Laser-Plasma Interactions **24**

- 2.1 Description of a plasma 24
- 2.2 The two-fluid model of a plasma and plasma waves 25
  - 2.2.1 Electron plasma waves 26
  - 2.2.2 Ion acoustic waves 28
- 2.3 Electromagnetic waves in plasma 29
- 2.4 Wave-wave interactions and parametric instabilities 31
- 2.5 Two-plasmon decay 33
  - 2.5.1 Single-beam, homogeneous TPD 35
  - 2.5.2 Multi-beam TPD 38
  - 2.5.3 Multi-beam SRS 42
- 2.6 Growth rates and instability threshold 42
  - 2.6.1 Multi-beam LPIs and hot electrons 46
- 2.7 Wave-particle interactions 47

3 Investigation of Hard X-ray Background in Backlit Pinhole Imagers **49**

3.1 Detection of X-rays 49
3.2 Experiments on OMEGA 52
3.2.1 Radiography 53
3.2.2 Varying pinhole substrate material 57
3.3 Conclusions 58
4 Experiments to Study Hot-Electron Production in High-Z Plasmas 60
4.1 Experimental Geometry 61
4.2 Hard x-ray measurements 62
4.2.1 Modeling of hard x-ray meaurements 65
4.2.2 Estimates of hot electron parameters 70
4.3 Angular Filter Refractometry to measure electron density profiles 71
4.3.1 Reconstructing Plasma Density Profiles 74
4.3.2 Processing of AFR data 76
4.3.3 Modeling of density profiles 77
4.3.4 Estimates of electron density profiles and length-scales 81
4.4 Conclusions 87
5 Radiation Hydrodynamic Simulations 88
5.1 CRASH Simulations 89
5.1.1 Comparison to Measurements 91
5.2 Evaluation of profile steepening 95
5.2.1 1D HYADES Simulations 98
5.3 Conclusions 99
6 Models of Hot-Electron Production 100
6.1 Discussion 100
6.1.1 Variation of plasma conditions 106
6.1.2 Linear instability thresholds 108
6.2 Conclusion 112
7 Mitigation of the Hard X-ray Background in Backlit Pinhole Imagers . . . 114
7.1 Experimental Design 114
7.1.1 X-ray diagnostics 116
7.2 Experimental Results 120
7.2.1 Radiography 120
7.2.2 Assessment of nonuniformities and other characteristics 121
7.2.3 Reconstruction of X-ray Spectra 129
7.2.4 Signal-to-background ratio 134
7.2.5 Future design of backlit pinhole imagers 137
7.3 Conclusions 140
8 Conclusions and Future Directions 141
Appendices 145
Bibliography 147

LIST OF FIGURES

1.1 Schematic of electron density, n_e and temperature, T_e profiles in a laser-produced plasma. 3

1.2 Right: False-color image of the Puppis A supernova remnant. Image from http://www.nasa.gov/sites/default/files/puppisa.jpg. Left: a time-sequence of x-ray radiographs observing the evolution dense clump broken apart by a laser-driven blast wave, from [1]. 6

1.3 X-ray backlighting techniques using laser-produced plasmas. I) Area backlighting, II) point-projection backlighting, III) backlit pinhole imaging. 9

1.4 a) Diagram of cylindrical and tapered pinholes (not to scale). In both cases, x-rays can cause ablation of the pinhole walls. The cylindrical pinhole will close more rapidly than the tapered case because the ablated plasma has less distance to travel and can stagnate on-axis. The tapered pinhole has a larger cutoff angle, θ_{tap} than the cylindrical pinhole ($\theta_{cyl} < \theta_{tap}$), making it less sensitive to rotational misalignment. b) Backlit pinhole imager target with CH scaffold holding a 300-μm diameter V dot away from the 7x7 mm Ta pinhole substrate. The laser irradiates a spot larger than the V dot. 12

1.5 a) Radiograph of a radiative shock experiment recorded on a layer of Agfa D7 film produced using a backlit pinhole imager (courtesy of Carolyn Kuranz). b) Lineouts of the recorded signal unattenuated by anything in the object plane (green) and the recorded signal behind aluminum calibration steps (black) in the object plane. The blue line is the expected signal behind the aluminum calibration steps calculated by transmitting the unattenuated profile through the steps, assuming it consists of He-α x-rays only. 13

1.6 Left: Direct-drive ICF, in which capsule implosion is driven by direct laser irradiation. Right: Indirect-drive ICF, in which capsule implosion is driven by x-rays converted from laser energy deposited in the walls of a high-Z hohlraum. 15

1.7 a) Computer rendering of the OMEGA-60 laser facility with photo of the target chamber. b) OMEGA EP laser facility showing the four long-pulse beamlines coupled to the target chamber. Credit: Laboratory for Laser Energetics . 19

2.1 The normalized homogeneous temporal growth rate squared, γ_0^2 for single-beam TPD in k-space. Arrows represent a decay diagram of the laser ($\mathbf{k}_0$) into decay EPWs ($\mathbf{k}_1$ and $\mathbf{k}_2$) along the maximum-growth hyperbolas from Eq. 2.41. 37

2.2 a) General decay diagram for two laser beams ($\mathbf{k}_{01}$ and $\mathbf{k}_{02}$) sharing a common EPW, $\mathbf{k}_c$. Regions of common-wave maximum growth geometries for b) two laser beams and c) more than two laser beams. 39
2.3 Left: Absolute instability, where an initial disturbance grows everywhere in time, t at the homogeneous growth rate, γ. Right: Convective instability, where an initial disturbance grows by a finite amount, $\exp(\pi G)$ as it propagates in space. 43

3.1 Spectral sensitivities of DEF x-ray film (black) from Brown et al. [2] and the MS-type image plate (magenta) calculated using GEANT4 and provided by Barukh Yaakobi at the Laboratory for Laser Energetics. 51
3.2 Side-on schematic of the backlit pinhole imager target, and orientation relative to experimental diagnostics, laser beams and an imaged object. 52
3.3 a) Radiograph recorded on image plate showing parylene calibration steps adjacent to plasma flow, from shot 69936. b) Beer's law fit to the step intensities (red circles), showing the expected signal as a function of an object's depth at the V He-α energy. 55
3.4 Relative error in estimates of optical depth, τ_α of unknown object. Estimates of I_α, I_{BG} and their respective errors are retrieved from fits to measurements of signal behind polystyrene steps, recorded on an a) Agfa D7 film and b) Fuji$^{\text{TM}}$ MS-type image plate. Black lines are the nominal case and red lines have I_{BG} set to zero, showing potential improvements for background mitigation. 56
3.5 a) The comparison of measured Background/Laser energy between different PH substrate materials. b) Response of image plate to x-rays of different energies for the 3 PH substrate materials, calculated as the product of transmission through the PH substrate + filtering and the image plate's spectral sensitivity. 57

4.1 Target and beam geometry for experiments studying hot electron production in high-Z materials 63
4.2 a) Scan of exposed image plate from the HXIP detector with labeled channels. Signals and background were calculated as averages over the blue and black boxes, respectively. b) Response curves for the 9 channels in the HXIP from the filter transmission multiplied by the IP spectral sensitivity. 64
4.3 a) Weighted least-squares functions that are minimized to estimate $\hat{\mathbf{p}}_{\text{cold}}$ and $\hat{\mathbf{p}}_{\text{hot}}$ vs. iteration in the two-temperature fitting procedure. b) HXIP channel signals from the Ti shot (squares) compared to fitted values (+), where the $\times$'s are the predicted signals of channels not used in the fit (1 and 2 here). The red dots (blue triangles) show the signal contribution from the hot (cold) spectral component only for channels 3 through 6. 69
4.4 Estimates of a) hot electron fraction, f_{hot} and b) hot electron temperature, T_{hot} and c) effective temperature of the thermal emission, T_{cold} vs target atomic number, Z_{nuc} from fits to HXIP measurements. The error bars on T_{cold} are smaller than the data points in most cases. 70

4.5 Simplified optical diagram of the AFR diagnostic. A 263-nm probe beam refracts through the plasma expanding from the target and is focused to the Fourier plane by an f/4 collection lens. Concentric angular filters in the Fourier plane block regions of the probe beam corresponding to specific bands of refraction angle. An image is formed with bands, along which the total refraction angle, θ_{ref} is constant. Adapted from Haberberger et al. [3]. 72
4.6 Visual representation of refraction contour fitting procedure. Refraction angle, $\theta(x, y)$ is represented as a surface in the $x - y$ plane. The purple dots represent the total refraction, $\theta_{\text{ref},i}$ along the y-axis at the locations of the contours in the image. The model refraction profile, $\tilde{\theta}(\mathbf{p})$ is shown in black for a given set of fit parameters, $\mathbf{p}$, where the black dots are the model refraction at the positions of the contours on-axis. The parameters are varied to minimize the difference between the true refraction and model refraction along the contours (i.e. make the black dots lie as close to the purple dots as possible). Only the axis is shown for clarity, but this procedure is applied to the entire refraction contours in the $x - y$ plane. 75
4.7 a) Image of undriven target with AFR probe beam without angular filters, showing the original target surface and fiducial sphere. b) AFR image of driven CH target with angular filters. c) Demonstration of contour extraction from thresholded image. Contours used in the fit for this image are shown in red. 78
4.8 a) Comparison between the AFR data and resulting refraction contours (dashed lines) from the fit for the CH plasma. b) The corresponding electron density profile with density contours at $n_c/4$ (solid line) and $n_c/10$ (dotted line). The corresponding plots for the Au plasma are shown in c) and d). 83
4.9 a) Best-fit electron density profiles on-axis ($r = 0$) vs. position from original target surface for several materials. Bands represent the one-sigma confidence interval and dotted lines are the fit extrapolated beyond the region where data was present. b) Estimates of electron density gradient length-scale on-axis vs. n_c/n_c from the profiles in (a). Again, the bands represent one-sigma confidence intervals and dotted lines are the fits extrapolated outside the data region. 84
4.10 Estimates of L_n from fits to data on-axis vs. Z_{nuc}, where open diamonds, gray circles and black triangles are at $n_c/50$, $n_c/10$ and $n_c/4$, respectively. 85
4.11 a) Estimates of coronal electron temperature using measured length-scales, calculated from relationships between sound speed and density profile from simple-planar and mass-limited models, compared to estimates of T_{cold} from HXIP measurements. b) Corresponding estimates of average ionization. . . . 86

5.1 Spatial profiles at 1.5 ns predicted by CRASH simulation of an irradiated Ti target. a) Electron density, b) electron temperature, c) axial velocity, d) radial velocity. 90
5.2 2D Electron density profiles at 1.5 ns, predicted by CRASH simulations for a) CH and b) Ag targets. Plots c) and d) are the corresponding density profiles from fits to refraction measurements. 92

5.3 Spatial profiles at 1.5 ns from CRASH simulations at a target radius of 50μm for a) CH and b) Ag targets. The electron density profile from the simulation is depicted as the black solid line and that from the fit to the data at the same position is shown as the solid gray line with one-sigma error band, all with relation to the left vertical axis. Dotted lines are the fit extrapolated outside the range of data. The electron temperature profile is shown by the solid red line, with relation to the right vertical axis. 93
5.4 Electron density gradient length scales for the different target materials at $n_c/50$, $n_c/10$ and $n_c/4$ from simulations (red) and fits to refraction data (blue) at 1.5 ns. 95
5.5 Electron density (solid) and temperature (dashed) profiles on axis from 2D CRASH simulations for each material, separated by color. 96
5.6 Electron density (solid lines) and temperature in keV (dashed lines) from 1D HYADES simulations at 0.8 ns, in a coordinate system where n_c is at the origin. The absorption and emission opacity multiplier, M is reduced to 0.5 for Cu and increased to 2 for Al to show the effect of radiation on the profiles. 97

6.1 a) Hot electron fraction and b) temperature estimates from hard x-ray measurements described in Ch. 4. 101
6.2 Convective thresholds for the MBSRS instability calculated along the target axis, using the length-scales from the fits to refraction data. Dotted lines represent where no refraction data was present 102
6.3 Normalized multi-beam TPD growth rate for the 4-beam OMEGA EP geometry along the common wave line, coinciding with the y axis ($\mathbf{k}_c = k_c\hat{\mathbf{y}}$) vs. wavenumber. The kinetic energy of an electron moving at the common wave's phase velocity, $v_p = \omega_c/k_c$ is shown on the right axis. 104
6.4 Plasma parameters from CRASH simulations vs target atomic number. Squares are at $0.18n_c$ and triangles are at $n_c/4$. a) Electron temperature, b) overlapped intensity ($\times 10^{14}$ W/cm^2). All are evaluated at 1.5 ns into the laser pulse. . . . 107
6.5 Predicted IAW damping rate divided by the real component of the frequency, ω_r evaluated at $0.18n_c$ and 1.5 ns into the laser pulse. 108
6.6 a) Damping parameter at $n_c/4$ for for multi-beam TPD, and b) TPD convective gains with (open) and without (red) damping of EPWs. 109
6.7 a) Threshold parameter, $\eta = I/I_{\text{thr}}$ vs. Z_{nuc} calculated from simulations at 1.5 ns for the absolute MBSRS instability at $0.18n_c$, the single-beam stimulated Raman backscatter (SBSRS) at $n_c/10$ and the convective multi-beam TPD instability at $n_c/4$ with the effects of damping. b) f_{hot} from Fig. 6.1 vs the multi-beam threshold parameters from a), where the lines are exponential fits for guidance. 111

7.1 Side-on schemata of the backlit pinhole imagers: design with A) bare CH scaffold; B) Al intermediate layer; C) V intermediate layer. 115
7.2 a) Photograph of backlit pinhole imager with Al scaffold. b) Rendering of resolution test target. 116

7.3 Diagram of backlit pinhole radiography to test strategies to mitigate hard x-ray background. A resolution test target was imaged onto 2 film layers and an image plate loaded in an RSPCA mount. A cannon spectrometer detected hard x-rays from the irradiated side of the pinhole imager, opposite the imaging direction. 116
7.4 Detector response (sensitivity × total transmission) for each of the 16 spectral filter channels listed in Table 7.1. a) Response for the IP and b) response for the film layer closest to TCC. Curves c) and d) are the differences in detector response between filters i and j, $K(E)\Delta T_{ij}(E)$ for the IP and film, respectively for selected Ross pairs. 118
7.5 a) Radiograph from recorded on the image plate from shot 74180 using a V scaffold target. Labeled spectral filters are placed in the detector plane. Scale corresponds to the object plane. b) Lineouts across the highest-Z filters (1 - 4) for each shot. The black line corresponds to the CH scaffold, and the blue and red lines correspond to the Al and V scaffolds, respectively, where solid and dashed lines indicate separate shots. 120
7.6 Illustration of how radiograph signal non-uniformities may originate for the different scaffold materials. Hard x-rays can produce a flare just beyond the aperture shadow, seen with the CH scaffold. Misalignment of the microdot would create a sharp cutoff in signal along the radiograph, seen possibly with the Al scaffold. Uncollimated expansion of the V plasma (expected with the V scaffold) may cause an extended source of soft x-ray emission beyond the edge of the pinhole substrate that would expose a large area of the detector, well into the aperture's shadow. 122
7.7 Radiographs from a pinhole imager using the nominal CH scaffold recorded on a) the first layer of film and b) the IP. c) Lineouts across the radiographs in a) and b) of the central unattenuated region (green lines) and across the acrylic fiducial ramp (black lines). Regions where lineouts were taken correspond to the boxes of same color and linestyle as in the radiographs. Dashed and solid lineouts are from the film and IP radiographs with intensity units OD and mPSL/μm^2, respectively. Lineouts from the IP radiograph show significant nonuniformity. The film fog has not been subtracted in the lineout. 124
7.8 a) Radiograph recorded on first layer of film from shot 74176 with Al scaffold, showing nonuniformity from right-to-left. The cyan dashed line represents the edge of the x-ray cone from a potentially misaligned V microdot. b) Radiograph recorded on first layer of film from shot 74181 with Al scaffold, with considerably lower overall signal. c) The green line is the lineout from the boxed region in a) showing the magnitude of the nonuniformity. The purple dashed line is the simulated intensity profile from a microdot that is misaligned 140 μm to the left of center. 125

7.9 a) Radiograph from shot 74180 the V scaffold recorded on the first layer of film. b) Zoom-in on region in radiograph near the edge of the aperture's shadow, focusing on the shadow of the V filter overlapped with the Cirlex filter holder. The diagram underneath describes this overlap. c) Lineouts across the radiograph and corresponding IP of the central unattenuated region (green lines) and across the acrylic fiducial ramp (black lines). As in Fig 7.7, dashed lines correspond to the film and solid lines correspond to the image plate. 127
7.10 Absolute values of covariances matrices, $\mathbf{S}_c$ of coefficients, c_b for individual-channel reconstruction using channels of a) IPs only, b) film only and c) both IP and film. Standard errors of the signals data were taken from shot 74188 to calculate $\mathbf{S}_y$ for each detector. 133
7.11 Reconstructed spectra from the filters in the radiograph plane. Colors and line style (solid/dashed) correspond to the lineouts in Fig. 7.5b. a) Reconstruction from individual channels using image plate signals only. b) Reconstruction from individual channels utilizing signals from both the image plate and film. 134
7.12 a) Inferred cumulative intensity distributions on the image plate from the reconstructed spectra for setup A, the current experiment. b) Signal and background on the image plate in units of mPSL/μm^2·kJ and the dimensionless signal-to-background ratio (SB) vs. scaffold atomic number, Z. The corresponding plots for setup B with a 30-μm V discriminator filter and no film are shown in c) and d). 135
7.13 Transmission (blue) of proposed radiography setup with 30 μm of V and no film and the transmission relative (orange) to that used in these experiments. 138
7.14 Proposed designs of future backlit pinhole imagers. Top: design using a transparent SiO_2 scaffold and V microdot. Bottom: design using a V foil embedded in a collimating cone that is symmetric about the horizontal axis. 139

A.1 Angular filter refractometry images for all targets in the experiments presented in Ch. 4. 146

LIST OF ABBREVIATIONS

AFR Angular Filter Refractometry

DAF Double Ablation Front

DT Deuterium-Tritium

EM Electromagnetic

EMW Electromagnetic Wave

EOS Equation of State

EPW Electron Plasma Wave

HED High Energy Density

HEDP High-Energy-Density Physics

IAT Ion-Acoustic Turbulence

IAW Ion-Acoustic Wave

ICF Inertial Confinement Fusion

IP Image Plate

LEH Laser-Entrance Hole

LLE Laboratory for Laser Energetics

LPI Laser-Plasma Instability

LTE Local Thermodynamic Equilibrium

MBSRS Multi-Beam Stimulated Raman Scattering

MCP Micro-channel Plate

OD Optical Density

PH Pinhole

PSL Photo-Stimulated Luminescence

RSPCA Rotational Static Pinhole Camera Array

RT Rayleigh-Taylor

SB Signal-to-Background Ratio

SBS Stimulated Brillouin Scattering

SRS Stimulated Raman Scattering

TPD Two-Plasmon Decay

TIM Ten-Inch Manipulator

ABSTRACT

Mitigation of Hot Electrons from Laser-Plasma Instabilities in Laser-Generated X-Ray Sources

by

Jeffrey R. Fein

Co-Chairs: James P. Holloway, R. Paul Drake

This thesis describes experiments to understand and mitigate energetic or "hot" electrons from laser-plasma instabilities (LPIs) in an effort to improve radiographic techniques using laser-generated x-ray sources. Initial experiments on the OMEGA-60 laser show evidence of an underlying background generated by x-rays with energies over 10 keV on radiographs using backlit pinhole radiography, whose source is consistent with hard x-rays from LPI-generated hot electrons. Mitigating this background can dramatically reduce uncertainties in measured object densities from radiographs and may be achieved by eliminating the target components in which LPIs are most likely to grow.

Experiments were performed on the OMEGA-EP laser to study hot electron production from laser-plasma instabilities in high-Z plasmas relevant to laser-generated x-ray sources. Measurements of hard x-rays show a dramatic reduction in hot-electron energy going from low-Z CH to high-Z Au targets, in a manner that is consistent with steepening electron density profiles that were also measured. The profile-steepening, we infer, increased thresholds of LPIs and contributed to the reduced hot-electron production at higher Z. Possible mechanisms for generating hot electrons include the two-plasmon decay and stimulated Raman scattering instabilities driven by multiple laser beams. Radiation hydrodynamic simulations using the CRASH code predict that both of these instabilities were above threshold with linear threshold parameters that decreased with increasing Z due to steepening length-scales, as well as enhanced laser absorption and increased collisional and Landau damping of electron plasma waves.

Another set of experiments were performed on the OMEGA-60 laser to test whether hard x-ray background could be mitigated in backlit pinhole imagers by controlling laser-plasma instabilities. Based on the results above, we hypothesized that LPIs and hot electrons that lead to hard x-ray background would be reduced by increasing the atomic number of the irradiated components in the pinhole imagers. Using higher-Z materials we demonstrate significant reduction in x-rays between $30 - 70$ keV and a 70% increase in the signal-to-background ratio. Based on this, a proposed backlighter and detector setup predicts a signal-to-background ratio of up to 4.5:1.

CHAPTER 1

Introduction

Soon after the invention of the laser in 1960, it was recognized that focused electromagnetic radiation could be used to rapidly heat materials to temperatures exceeding 10 million degrees Kelvin—approximately that of the sun's core—in less than a nanosecond [4,5]. At such high temperatures a material exists typically as a multiply-ionized plasma, and through various processes emits x-rays with energies ranging from a few eV to several keV. Such laser-produced plasmas have become a basis for laboratory studies of matter at extreme conditions, and their application has yielded insights into phenomena ranging from astrophysics to the physics of nuclear weapons. They play integral roles in both creating extreme conditions, as a mediator of immense pressure, and in probing them, through the creation of bright x-ray sources.

The physics of such plasmas can be considerably complex and has become a major topic of study in the pursuit of laser fusion, among other fields. For nanosecond lasers with irradiances between $10^{10} - 10^{16}$ W/cm^2, plasma hydrodynamic motion is determined in large part by the collisional absorption of laser energy, but can be strongly influenced by electron heat conduction, radiation transport and even laser-generated magnetic fields. In addition, the lasers can parametrically excite an assortment of waves within the plasma that may grow unstably and alter the plasma energetics. When these excited waves are electron plasma waves, electrons with energies in excess of 100 keV can be generated.

Such “hot electrons” are typically undesirable in most experiments, as they can heat up target components altering initial conditions of an experiment, as well as degrade diagnostics. This thesis presents results on the role that hot electrons play in producing unwanted background in x-ray radiography using laser-produced x-ray sources. In addition it demonstrates how to mitigate this background based on a detailed understanding of the laser-plasma interactions involved.

1.1 Physical Picture of Laser Plasmas

A laser can deposit its energy in a solid material to create a hot plasma in a variety of ways. For the experiments discussed in this thesis, the plasmas are heated primarily by collisional absorption of laser energy. An initially cold target will practically always have some number of free electrons near its surface, typically generated by cosmic rays. The strong electric field of a laser incident on the target’s surface will accelerate the electrons, which then scatter off nearby ions through Coulomb collisions with frequency,

$$\nu_{ei} = 3 \times 10^{-6} \frac{n_e Z_{\text{eff}}}{T_e^{3/2}} \ln \Lambda \ \ \text{s}^{-1} \tag{1.1}$$

Here, n_e and T_e are the plasma electron density and temperature in units of cm^{-3} and eV, respectively. The quantity, $Z_{\text{eff}} = \langle Z^2 \rangle / \langle Z \rangle$ where Z is the ion charge state and $\langle \rangle$ represents an average over all species present, and $\Lambda = 9N_D/\langle Z \rangle$, with N_D being the number of particles in a Debye sphere [6]. The presence of ions is necessary for the electrons to gain net energy over the oscillation period of the laser’s electric field. This scattering process is called *inverse bremsstrahlung* (Sec. 2.3), and is indeed the inverse of bremsstrahlung radiation, where an electron loses energy though emission of a photon while decelerating in an ion’s Coulomb potential. The coefficient for inverse-bremsstrahlung absorption of

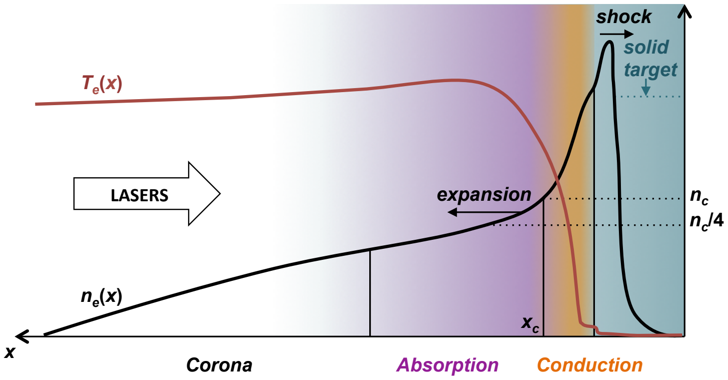

Figure 1.1: Schematic of electron density, n_e and temperature, T_e profiles in a laser-produced plasma.

a laser with frequency ω_0 is approximately

$$\kappa_{IB} = \frac{\nu_{ei}}{c}\frac{\omega_{pe}^2}{\omega_0^2}\frac{1}{\sqrt{1-\omega_{pe}^2/\omega_0^2}}, \tag{1.2}$$

with dimensions of inverse-length. Here, c is the speed of light, and ω_{pe} is the electron plasma frequency, or natural oscillation frequency of electrons in the plasma,

$$\omega_{pe} = \sqrt{\frac{e^2 n_e}{m_e \varepsilon_0}}, \tag{1.3}$$

where e and m_e are the electron charge and mass, respectively, and ε_0 is the permittivity of free space and n_e is in SI units. As the electrons gain energy over several oscillation periods, they will further ionize the solid target in a cascading fashion through collisions with bound electrons—resulting in the formation of a plasma. (Alternatively, at sufficiently high intensities, the potential energy of an electron in the laser's electric field can exceed the ionization energy of the atom and the laser will ionize the atom directly.)

The subsequent dynamics are described with reference to the illustration of electron density and temperature profiles depicted in Fig. 1.1. Immediately, a hot, low-density plasma *corona* expands away from the target at high velocities. The corona typically remains isothermal through absorbing some of the laser energy or by rapid heat conduction from higher densities where the majority of laser absorption occurs. If the laser does not deposit its energy fully in this *absorption* region, it will propagate up to the critical density surface, where $\omega_{pe} = \omega_0$. The *critical density*, n_c corresponding to this condition is

$$\begin{aligned} n_c &= \frac{\omega_0^2 m_e \varepsilon_0}{e^2} \qquad (1.4) \\ &= \frac{1.12 \times 10^{21}}{\lambda_\mu^2}\ \mathrm{cm}^{-3} \qquad (1.5) \end{aligned}$$

where λ_μ is the laser's wavelength in vacuum in microns. Here, the laser will either reflect or be absorbed completely by resonant processes, depending on its incident angle and polarization [7]. With reference to Eq. 1.2, collisional absorption is most efficient near the critical surface as a consequence of the EM wave coupling most strongly when the plasma electrons are resonantly oscillating at the EM wave's natural frequency.

As absorption ceases beyond the critical density, the temperature drops rapidly and the dynamics become dominated by transport of heat towards the solid target via electron thermal *conduction*. The mass in this region ablates away from the target up to a location known as the ablation front, producing an outward energy flux that roughly balances thermal energy-transport inward. By conservation of momentum, the ablating mass induces a reactionary ablation pressure, P_a normal to the target's surface, which compresses the solid material and launches it inward. Low-Z targets are generally better for generating ablation pressure than higher-Z targets at a given intensity for a variety of reasons. The low charge states and therefore collisions help localize laser absorption near the critical surface, rather than wasting excess energy by heating the coronal plasma. Fewer collisions also improve electron thermal conductivity, such that energy can be transported to the dense material more efficiently. Lastly, energy losses by radiation are nearly always less efficient (and typically negligible) in low-Z plasmas.

Using a 1D planar stationary ablation model for low-Z targets [8], the ablation pressure and coronal electron temperature, T_{c} can be approximated as,

$$T_{\mathrm{c}} = 2.8\,(I_L\lambda_\mu^2)^{2/3}\frac{\langle Z\rangle^{2/3}A^{1/3}}{(\langle Z\rangle+1)}\ \text{keV}, \tag{1.6}$$

$$P_{\mathrm{a}} = 6.7\,(I_L/\lambda_\mu)^{2/3}\frac{(\langle Z\rangle+1)}{\langle Z\rangle}\ \text{Mbar}, \tag{1.7}$$

where I_L is the absorbed laser intensity near n_c in units of 10^{14} W/cm^2 and A is the material's atomic mass. The coefficient in front varies according to model specifics concerning electron heat transport and plasma expansion velocity near the critical surface [8–10]; however, the overall magnitude does not change drastically. For a UV laser with 0.35-μm wavelength incident on a CH target ($\langle Z\rangle = 3.5$) at an irradiance of 10^{15} W/cm^2, we have $T_{\mathrm{c}} \approx 3$ keV and $P_{\mathrm{a}} \approx 80$ Mbar. At these pressures, the compression produces a shock wave, heating the solid material while driving it inward.

1.2 High-Energy-Density Physics and Laboratory Astrophysics

The extremely high temperatures and densities that can result under ablation pressures ranging from 10 Mbar – 1 Gbar grant access to material conditions much like those at the center of stars and planets, as well as those produced in a thermonuclear explosion. Such systems are said to be at "high energy density," (HED).

One exciting application of high-energy-density physics (HEDP) is the study of astrophysically relevant properties and processes in a terrestrial laboratory. Here, aspects of an astrophysical system that is evolving on the scale of millions of kilometers-to-light-years, over days-to-millions of years, can be scaled to a laboratory system evolving on the scale of millimeters, over a matter of nanoseconds. This is done through the scaling

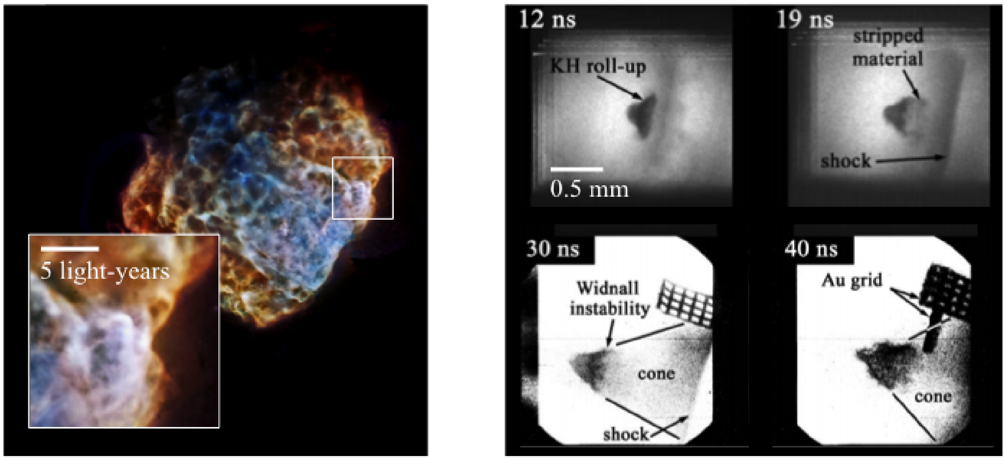

Figure 1.2: Right: False-color image of the Puppis A supernova remnant. Image from http://www.nasa.gov/sites/default/files/puppisa.jpg. Left: a time-sequence of x-ray radiographs observing the evolution dense clump broken apart by a laser-driven blast wave, from [1].

of hydrodynamic equations, by conserving dimensionless quantities that describe both systems' key hydrodynamic behavior. As an example, Fig. 1.2 shows an image taken by the Chandra x-ray telescope of the Puppis A supernova remnant. The inlet image of the "Bright Eastern Knot" shows what has been identified as a dense cloud of interstellar matter several light-years across being crushed by the supernova's shock wave [11]. On the right is a time-sequence of x-ray radiographs showing the temporal evolution of a scaled experiment from [1], in which a 120-μm-diameter aluminum sphere is crushed as a laser-driven blast-wave passes over. The experiment provided insight into the mass-stripping process that would occur in the astrophysical system, which is thought to affect the rate of star formation throughout the universe. Many other experiments like these can and have helped bridge the gap between astrophysical observation and theory [12–14]. Diagnosing these experiments requires bright x-ray sources, much like the backlit pinhole imager used to produce the radiographs above. These sources are described in the next section.

1.3 Laser-produced x-ray sources

Laser plasmas from mid- to moderately high-Z elements heated to 2–4 keV have significant populations of atoms in multiply-ionized states. Recombination of free electrons and de-excitation of bound electrons into shell vacancies in these atoms will produce characteristic x-ray emission with energy equal to the difference in potential energy of the states involved in the transition, ΔE. For elements with $17 \lesssim Z \lesssim 32$ (chlorine to germanium) resonant He-like transitions from the $n = 2, 3$ (L-and M-shell) to $n = 1$ (K-shell) state become dominant with x-ray energies ranging from $2.7 - 10$ keV. Without further increases in temperatures, ionization beyond the K-shell to form H-like atoms is rare. The continuum emission from thermal bremsstrahlung near the He-α energy is usually significantly lower in magnitude. Using elemental filters to attenuate the He-β and other lines, one can therefore produce a quasi-monoenergetic x-ray spectrum from these plasmas. Previous work has demonstrated conversion efficiencies of laser energy into He-α energy emitted into 4π steradians up to 3% for irradiances between $10^{14} - 10^{16}$ W/cm^2, with a peak around 10^{15} W/cm^2 [15–18]. Hence, even moderate laser energies of 2 kJ and intensities $\sim 5 \times 10^{14}$ W/cm^2 available at many facilities can produce $>10^{15}$ He-α photons/steradian. The conversion efficiency decreases with Z because more energy is required to strip the atoms down to He-like states.

In steady-state in these optically thin plasmas, collisional excitation dominates the $1s^2 \rightarrow 1s^1 2p^1$ transition and is approximately in balance with the radiative $1s^1 2p^1 \rightarrow 1s^2$ transition. The text by Salzmann [19] provides a good overview of the atomic physics involved in both of these processes. A main result is that the rate of collisional excitation peaks when $T_e \approx \Delta E/3$. When the temperature decreases by dropping the laser power, the reduction in collisional excitation will soon quench line-emission. As a consequence, lasers can produce a bright flash of x-rays whose duration is on the order of the laser pulse. These x-rays can be used to diagnose high-density hydrodynamic flows evolving over nanoseconds [13, 14, 20–24].

Line-emission x-ray sources can be made using much higher-intensity lasers with much shorter durations, on the order of several fs to a few ps [25, 26]. For these sources, electrons are directly accelerated by the laser to energies ranging from hundreds of keV to several MeV and induce K-shell x-ray emission through electron-impact ionization of atoms in the cold target. However, this process of producing x-rays is much less efficient than by collisional excitation and radiative de-excitation in a hot plasma. In addition, the very energetic electrons produced can escape the target and interact with diagnostics and neighboring components, leading to MeV bremsstrahlung background x-rays that can overwhelm an experiment [27].

1.3.1 X-ray Backlighting Techniques

X-ray backlighting is a common diagnostic technique, in which an object is backlit with a laser-plasma x-ray source, and a detector some distance away images the transmitted x-rays [28–35]. The signal intensity, $I(x, y)$ on the detector is proportional to the object's transmission, $T_E(x, y)$ or fraction of x-rays at energy, E transmitted, and is given by the Beer-Lambert law, $T_E(x, y) = \exp[-\tau_E(x, y)]$, where τ_E is the object's object depth,

$$\tau_E(x, y) = \int_{s_0}^{s(x,y)} \sigma_{\text{tot}}(E)\rho(s)ds. \tag{1.8}$$

Here, σ_{tot} is the total photon interaction cross section that depends on the probing x-ray energy and the object's material composition, which along with the mass density, ρ, can vary along the ray path coordinate, s. Three separate backlighting techniques using thermal plasmas have been developed for transmission imaging on HEDP laser facilities, shown schematically in Fig. 1.3.

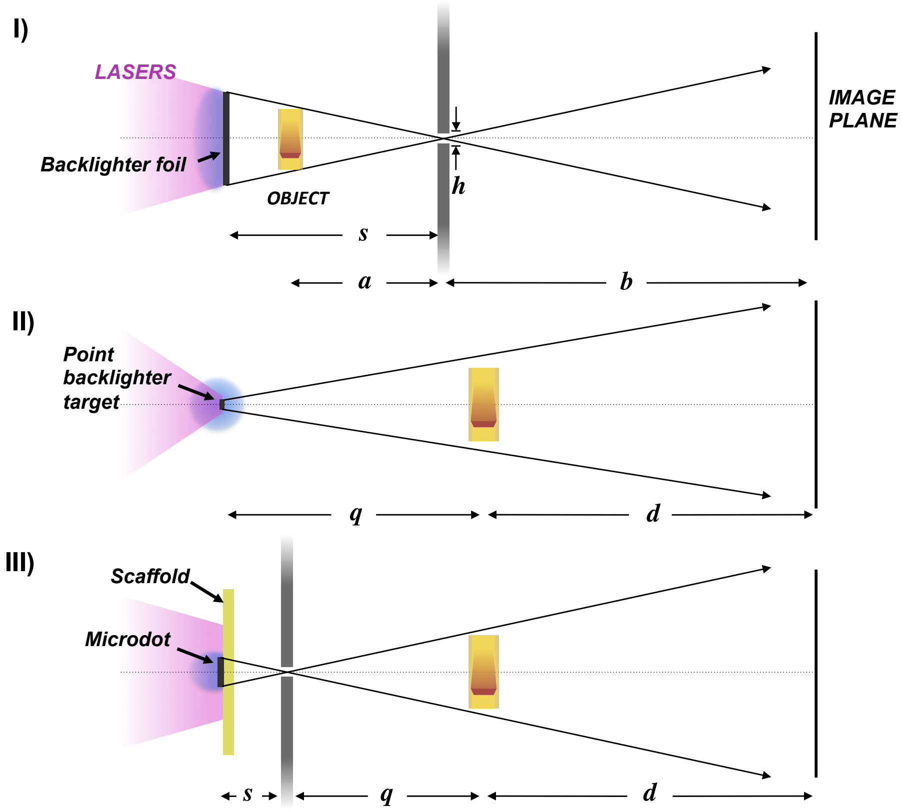

Figure 1.3: X-ray backlighting techniques using laser-produced plasmas. I) Area backlighting, II) point-projection backlighting, III) backlit pinhole imaging.

I) Area backlighting: In this technique [29, 30, 35–38], the object is placed between a large laser-irradiated foil and a substrate containing a pinhole aperture with diameter, h. The x-rays emitted by the backlighter foil image the object onto a detector a distance b away from the aperture, much like in a simple pinhole camera. The magnification is given by the ratio $M_{AB} = b/a$, where a is the object-aperture distance in this case. Area backlighting is attractive in part because in this technique, diffraction from the pinhole places a lower limit on the spatial resolution, and flexibility in placement of the pinhole aperture provides a wide range of possible magnifications. As well, a pinhole array can be used—rather than a single aperture—to acquire three-dimensional information from the parallax between neighboring pinholes, or to provide temporal information when coupled to an x-ray framing camera [29,30]. However, the technique can suffer from low signal due to the need to heat a relatively large foil area of several mm^2 with limited laser energy, as well as from signal nonuniformities that are difficult to avoid when using such an extended x-ray source.

II) Point-projection backlighting: In this case, a small target (e.g. the end of a thin wire) with dimensions of $\sim$10 μm is irradiated by tightly focused lasers [39] creating a point-like x-ray source that images the object onto a detector. The magnification is given by $M_{PP} = (q + d)/q$, where q and d are the source-object and object-detector distances, respectively. These sources tend to be significantly brighter than area backlighters because higher intensities can be achieved and the total optical throughput is much higher since no pinhole aperture is needed to form an image. Their small size mitigates nonuniformities. And as a single-target device, they are also easier to field experimentally. However, spatial resolution is typically worse than in area backlighters because the plasma tends to expand beyond the laser spot. For this reason, the laser pulse must be kept reasonably short ($\lesssim$200 ps) or a gated detector must be used [29]. In addition, the lack of a pinhole substrate means that the object and detector are no longer shielded from plasma and debris ejected from the point backlighter target.

III) Backlit-pinhole imaging: Also referred to as "pinhole-assisted point-projection backlighting," this technique has been developed to alleviate some of the issues encountered with area and point-projection backlighting [29–32, 34, 40, 41]. Here, lasers produce a $\sim 200 - 800$-μm-diameter backlighting plasma either by a properly-sized focal spot or by using a *microdot* backlighter foil attached to a lower-Z substrate. The irradiated foil emits x-rays more-or-less isotropically, similar to the point-projection case. However, now a pinhole substrate is placed at a distance, s, from the microdot, prior to the object. Hence, the spatial resolution is again set by the size of the pinhole, like in area backlighting, but the x-ray throughput ($\propto (h/s)^2$) can be much higher due to the shorter distance between source and aperture, s, providing significant improvements in signal-to-noise ratios. In addition, the pinhole substrate shields the target and detector package from the backlighter plasma. The magnification is identical to the point-projection case, where q becomes the pinhole-object distance.

In initial designs, a cylindrical pinhole was used; however, evidence showed that the large x-ray energy flux, of order 10^{10} W/cm^2, led to ablation of the high-Z pinhole wall, causing it to expand inward at $\sim 4\mu\text{m/ns}$, close and attenuate much of the desirable x-ray signal [31, 34]. The effect worsened the trade-off between spatial resolution and throughput, as a smaller pinhole closed more rapidly than a larger one. This, in part, motivated the use of tapered pinholes, wherein the pinhole diameter linearly increases across the substrate, as shown in Fig. 1.4a. Tapered pinholes also help prevent vignetting and make backlit pinhole imagers less sensitive to rotational misalignment by increasing the angle of the x-ray cone exiting the pinhole [40].

In common designs of backlit pinhole imagers, a microdot is held from the pinhole substrate by a low-Z (typically CH) scaffold, as depicted in Figs. 1.3, and 1.4b [40]. The laser irradiates a spot that is significantly larger than the microdot, creating a fast blow-off

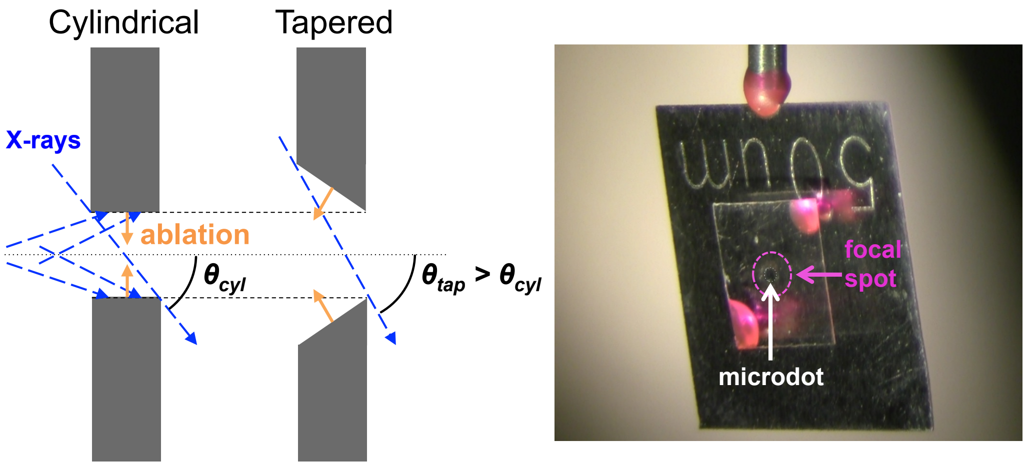

a) b)

Figure 1.4: a) Diagram of cylindrical and tapered pinholes (not to scale). In both cases, x-rays can cause ablation of the pinhole walls. The cylindrical pinhole will close more rapidly than the tapered case because the ablated plasma has less distance to travel and can stagnate on-axis. The tapered pinhole has a larger cutoff angle, θ_{tap} than the cylindrical pinhole ($\theta_{cyl} < \theta_{tap}$), making it less sensitive to rotational misalignment. b) Backlit pinhole imager target with CH scaffold holding a 300-μm diameter V dot away from the 7x7 mm Ta pinhole substrate. The laser irradiates a spot larger than the V dot.

plasma from the low-Z scaffold. The low-Z plasma may surround the microdot plasma, potentially inhibiting its expansion around the pinhole substrate and therefore, emission of x-rays towards the detector at late times—mainly an issue for un-gated detectors such as film and image plates.

While backlit pinhole imagers offer an improvement in spatial resolution and brightness over the other radiographic techniques, the designs have faced issues with low signal-to-background ratio. Figure 1.5a shows a radiograph of a radiative shock experiment recorded on x-ray film with aluminum calibration steps placed in the object plane. The steps provide information about the incident source of x-rays that attenuates through the object since x-ray intensity is unknown and can vary significantly shot-to-shot. The green profile in Fig. 1.5b is a lineout of signal intensity across the region between the steps and shock tube, where no object is present. Non-uniformities are clearly present after partially filtering out shot noise by averaging over 15 pixels in the vertical direction.

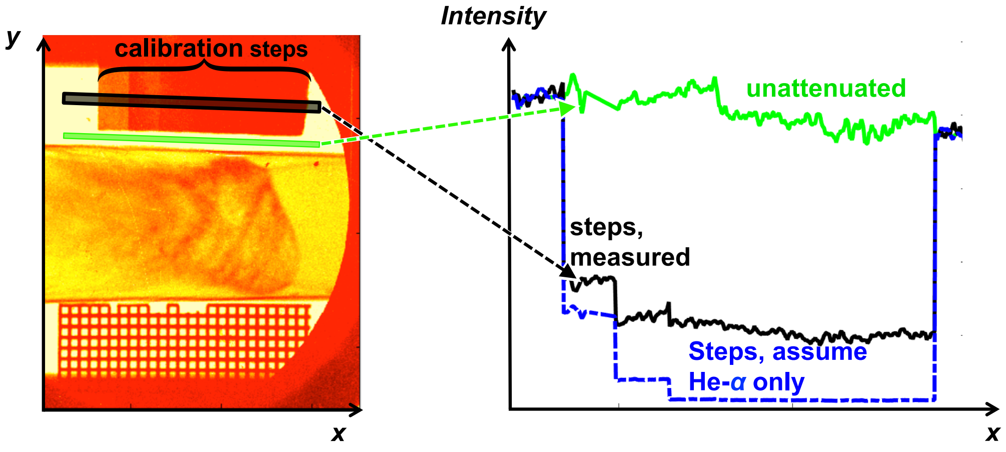

a) b)

Figure 1.5: a) Radiograph of a radiative shock experiment recorded on a layer of Agfa D7 film produced using a backlit pinhole imager (courtesy of Carolyn Kuranz). b) Lineouts of the recorded signal unattenuated by anything in the object plane (green) and the recorded signal behind aluminum calibration steps (black) in the object plane. The blue line is the expected signal behind the aluminum calibration steps calculated by transmitting the unattenuated profile through the steps, assuming it consists of He-α x-rays only.

If we assume that all of this "unattenuated" signal is from 5.18 keV He-α x-rays from the emitting V microdot, we can easily calculate the expected transmission behind the steps of known density and thicknesses (25, 50, and 75 μm). This is shown as the blue-dashed profile–multiplying the green profile by the step transmission–in which the magnitude of the non-uniformities has dropped proportionally with the average signal. A lineout across the steps from the radiograph (black profile) shows both significantly higher signal and larger non-uniformities than would be expected from solely a He-α source. As well, the cross-correlation between the green and black profiles is highly peaked at zero offset from one another, due to similarities in the non-uniformities. All of this evidence supports the notion that a "harder" source of x-rays with energies $\gtrsim$ 10 keV essentially transmits with significantly less attenuation through the aluminum steps and experimental object, and contributes background on the detector. Past work has attributed this hard x-ray background to x-rays produced by hot electrons generated via laser-plasma instabilities occurring in the backlighter and scaffold plasmas [16,42,43]. Some of the background may also arise from thermal emission of these hot plasmas. Part of the work in this thesis helps to confirm the origin of the x-ray background, and to develop mitigation strategies via a thorough understanding of the relevant laser-plasma instabilities. These are introduced below and described in detail in Ch. 2.

1.4 Inertial Confinement Fusion

In nuclear fusion, light atomic nuclei fuse together and release net energy, some of which may be converted into electricity for power consumption. If realized on Earth, nuclear fusion power would offer a virtually unlimited source of clean energy, and therefore a means to drastically reduce humans' burning of fossil fuels and impact on global climate change. The principle concept for achieving net energy gain is to sustain a thermonuclear reaction in a hot plasma for sufficient lengths of time. Here, the increase in energy amongst any electrically-charged fusion reaction products can be distributed to the rest of the plasma via Coulomb collisions, inducing new fusion reactions. *Ignition* occurs when the rate of heating by the fusion products is larger than the rate of energy loss by mechanisms such as expansive cooling and radiation. In inertial-confinement fusion (ICF) the fuel is compressed and heated to high enough densities and temperatures that fusion reactions occur at such a high rate that the fuel does not have time to expand under its own inertia. High-energy lasers can be used for this purpose, to drive the spherical implosion of cryogenic deuterium-tritium targets, either by direct laser-irradiation of the target (direct drive), or by heating the inside of a high-Z enclosure or *hohlraum*, producing x-rays that irradiate a capsule at the hohlraum's center (indirect drive) [44, 45]. These two drive approaches are shown in Fig. 1.6. Both use the "hot-spot" ignition scheme: radiation in the form of lasers or x-rays heats up the surface of a low-Z ablator surrounding a spherical shell of

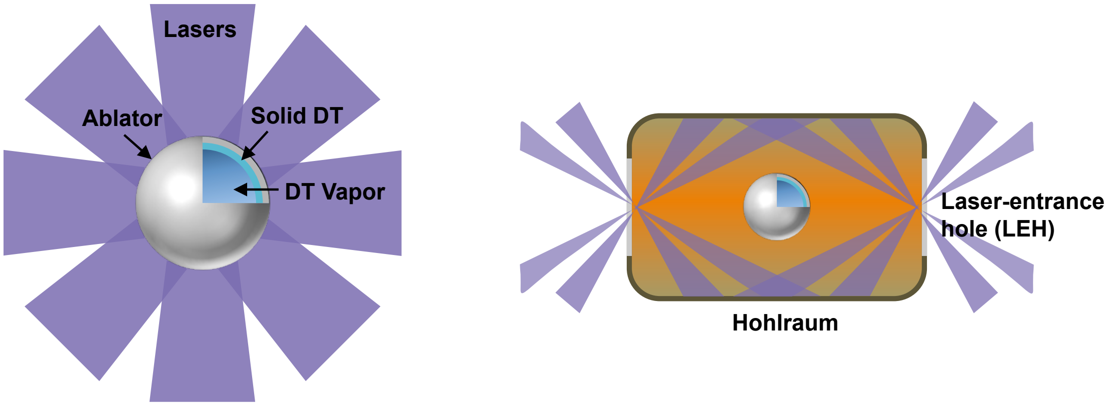

Figure 1.6: Left: Direct-drive ICF, in which capsule implosion is driven by direct laser irradiation. Right: Indirect-drive ICF, in which capsule implosion is driven by x-rays converted from laser energy deposited in the walls of a high-Z hohlraum.

solid deuterium-tritium (DT) fuel enclosing DT vapor. The low-Z ablator plasma that is produced ablates outward, launching a shock and accelerating the remaining ablator and solid DT fuel inward. Upon stagnation, the fuel is compressed to high density and temperature and a hot-spot ignites in the dense vapor, initiating a thermonuclear burn-wave that propagates outward through the solid DT fuel [8].

Many challenges arise in the scheme outlined above. The implosion must be nearly spherically symmetric throughout its duration to achieve maximum performance [46]. Perturbations to spherical symmetry can grow exponentially through Rayleigh-Taylor (RT) instabilities, lowering compression and mixing cold outer-material into the fuel, reducing performance [47]. In direct drive, this puts stringent requirements on uniformity of the laser irradiation profile as laser hot spots can cause pressure perturbations that make the ablation front RT-unstable [48, 49]. The more uniform radiation bath of soft x-rays in indirect drive alleviates this issue while compromising much of the drive energy through the laser light-to-x-ray conversion process. Another challenge is to keep the fuel on a low adiabat to achieve maximum compression efficiency [50]. Using a series of timed shocks can produce an essentially adiabatic compression [8]. However, any preheat of the fuel can increase the adiabat and hence, the work required to achieve a given compression. Hot electrons from laser-plasma instabilities are a major source of preheat in both direct and indirect drive [51–53]. X-rays from the hot coronal plasma also contribute to fuel preheat.

1.5 Laser-plasma instabilities and hot electrons

As the lasers propagate through the plasma they produce, they can drive laser-plasma instabilities (LPIs), whereby a laser's electromagnetic wave parametrically decays into a pair of waves that are normal modes of the plasma: electron plasma waves (EPWs), ion-acoustic waves (IAWs) and/or scattered electromagnetic waves (EMWs). As these waves grow, they remove energy from the laser that would otherwise be absorbed collisionally and converted into ablation pressure. Growth occurs when the driving lasers' irradiance is above a threshold set by the level of inhomogeneity and damping of the decay waves, and depends on plasma conditions throughout the growth region. Even while keeping the average beam irradiances well below threshold, beam speckle as well as filamentation from both ponderomotive and thermal effects can produce local irradiance hot-spots that inevitably lead to instability [49].

In stimulated Raman scattering (SRS) and two-plasmon decay (TPD), one or both of the decay waves are electron plasma waves (EPWs), which can grow to large amplitudes on a timescale much faster than the laser pulse. Electrons from the thermal distribution can be accelerated in the EPWs' electric fields through nonlinear wave-particle damping mechanisms [54, 55]. For TPD in particular, the large phase velocities of the EPWs can lead to electrons with energies in excess of 100 keV [56]. These suprathermal or "hot electrons" are typically detrimental to most experiments. Past experiments have observed as much as $\sim 5\%$ of driving laser energy converted into hot electrons; this was observed through measurements of the hard x-rays produced when the hot electrons interact in the target [57].

In a material of nuclear charge, Z_{nuc}, the mean range x_0 of hot electrons from a Maxwellian distribution with temperature T_{hot} is,

$$x_0 = 3 \times 10^{-6} \frac{A T_{\text{hot}}^2}{Z_{\text{nuc}}^{3/2}} \ \text{g/cm}^2. \tag{1.9}$$

For a typical temperature of $T_{\text{hot}} \sim 30$ keV from either TPD or SRS the mean penetration depth in plastic with a solid density of $\sim$1 g/cm^3, is $\sim$30 μm [10,58,59]. This is on the order of the plastic ablator thickness in direct drive ICF capsules, indicating that hot electrons generated near the target surface can penetrate into the solid DT fuel, preheating it and making it less compressible. Experiments on low-adiabat cryogenic D_2 implosions have estimated $\sim 0.2\%$ of the laser energy was converted into hot-electron preheat, and played an important role in compression degradation [51]. The laser intensity may be increased to achieve a higher compression due to higher implosion velocities. However, hot-electron production also increases with intensity and can counteract this measure [60]. In indirect drive, hot electrons are generated farther from the capsule in the low-density fill-gas plasma between the capsule surface and the hohlraum wall. The capsule subtends, therefore, a smaller solid angle from the point of view of a hot-electron source. This can relieve the issue of hot electron preheat in indirect drive. However, it still poses some threat because of the long scale-lengths present in hohlraum plasmas that lead to low instability threshold [45]. Hot electrons can also be generated from TPD and SRS by lasers interacting with the hohlraum's laser-entrance holes LEHs [61,62]. Recent work has provided evidence that hot-electron preheat may be responsible for shock mistiming in indirect drive implosion experiments, with estimates from simulations that the expected preheat can reduce the peak fuel compression at stagnation by $\sim 30-40\%$ [52].

Preheat by hot electrons can also be an issue for laboratory astrophysics experiments, and is expected to have a much larger effect than radiative preheat. Numerical studies have shown that hot electron preheat is expected to significantly alter interfacial conditions in experiments to study growth of hydrodynamic instabilities. For example, preheat ultimately makes the initial conditions unknown, but may reduce the initial amplitude of a surface perturbation by up to 40% [63,64]. This is undesirable because the initial interface must be well-characterized to make valid comparisons to predictions at later times.

In addition to preheat issues, interaction of hot electrons with the target and surrounding materials can produce K-shell and bremsstrahlung x-rays with many tens- and greater than 100 keV in energy, as mentioned above. These x-rays can become a source of background and noise on x-ray diagnostics, either through direct incidence on detectors, or through secondary x-ray fluorescence in shielding components [42, 65–67]. Of highlight here is the hard x-ray background they produce in backlit pinhole imagers.

For the reasons stated above, it is typically desirable to mitigate LPIs, and some measures have been developed in part for this purpose. Shorter wavelength lasers have drastically reduced the presence of LPIs, as well as increased the efficiency of collisional laser absorption [49, 59]. Different types of beam smoothing, such as induced spatial incoherence and smoothing by spectral dispersion, have been invented and adopted to limit the effect of intensity hot spots. These techniques do not eliminate intense speckles outright, but produce a speckle coherence time as low as $\sim$0.5 ps, limiting the time a hot spots' irradiance is above threshold. However, they are not practical or feasible in many laser facilities.

LPIs can also be mitigated by altering plasma parameters that determine their thresholds and growth rates. In general, plasma density inhomogeneity (i.e. a density gradient) can introduce phase mismatch between the laser and decay waves; shorter density

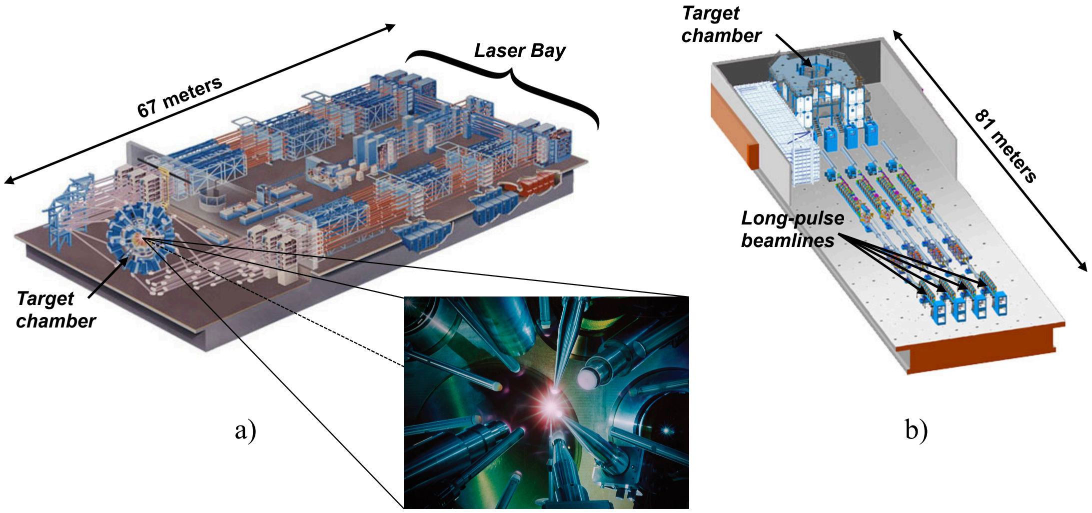

Figure 1.7: a) Computer rendering of the OMEGA-60 laser facility with photo of the target chamber. b) OMEGA EP laser facility showing the four long-pulse beamlines coupled to the target chamber. Credit: Laboratory for Laser Energetics

length-scales lead to higher thresholds [68]. Thresholds can also be increased by raising the amount of damping of the decay waves through collisions or nonlinear wave-particle mechanisms [69]. Turner et al. have shown collisional damping to be important in determining the level of SRS generated in Au and CH targets [70]. Growth of LPI decay waves can also be limited by decreasing the Landau damping of IAWs, which has the effect of lowering the threshold for nonlinear saturation processes. Studies by Fernandez [71] and Kirkwood [72] have shown the SRS reflectivity to be proportional to the IAW damping, which was varied by introducing low- and high-Z dopants. A similar result for TPD has been seen by Seka et al. [73], through the variation of $3\omega_0/2$ and $\omega_0/2$ emission which is characteristic of TPD [74].

1.6 High-Energy-Density Facilities

Several facilities exist worldwide that provide access to high-energy-density physics conditions. Many of these are laser facilities, using Nd-glass as the lasing medium with stimulated light emission centered in the infrared at 1.053 μm (referred to as 1ω light). Several Z-pinch facilities also exist; these use magnetic fields to implode a cylindrical array of current-carrying wires to high temperatures and densities.

The experimental campaigns reported on in this thesis were carried out on the OMEGA-60 and OMEGA-EP (Extended Performance) laser facilities at the Laboratory for Laser Energetics (LLE), University of Rochester [75, 76]. The OMEGA-60 laser (Fig. 1.7a) consists of sixty laser beams arranged in spherical geometry capable of delivering 30 kJ of energy in the form of frequency-tripled 3ω light onto a target positioned approximately at the center of a target chamber. Each beam is polarization-smoothed [77]. Pulse lengths can be varied from $\sim$100 picoseconds to several nanoseconds, with a variety of pulse shapes. The facility has the capability of producing and fielding cryogenic deuterium or tritium spherical targets and was designed to study key issues with direct-drive ICF implosions, including irradiation uniformity, hydrodynamic instabilities, and hot-spot physics among others.

The OMEGA-EP laser (Fig. 1.7b) has a set of four long-pulse beams of 1ω light nominally arranged in a conical geometry with a cone half-angle of 23°. The linearly polarized beams can be frequency tripled and deliver between $\sim 0.2 - 6$ kJ of energy/beam as 3ω light depending on the pulse length, which can vary from 100 picoseconds to 10 nanoseconds. In addition, OMEGA-EP contains two short pulse beams of 1ω light and pulse lengths of 10 to 100 picoseconds. Parabolic mirrors can focus these beams down to spots of 10-μm-diameter, producing peak irradiances $> 10^{19}$ W/cm^2 on-target. Both OMEGA-60 and OMEGA-EP have a variety of phase plates available for each beam capable of producing supergaussian irradiance profiles with FWHM between $\sim 0.1 - 1$ mm on-target.

1.7 Contributions by the author

This section makes the distinction between the contributions by the authors and those of the many individuals that made this work possible.

- Chapters 1 and 2: These chapters introduce the relevance of the thesis to the field of HEDP as well as theoretical background, most of which was adapted from references spanning several decades of prior work.

- Chapter 3: Paul Keiter was the principal investigator for the experiments presented in this chapter. Targets were machined by Rob Gillespie and fabricated by Sallee Klein at the University of Michigan. David Meyerhofer originally suggested changing the pinhole substrate material in the pinhole imagers. The author designed other aspects of the pinhole imagers/radiography system and carried out all data analysis presented in this chapter.

- Chapter 4: The author was the principal investigator for these experiments under the guidance of Paul Keiter, Dana Edgell and Dustin Froula. Targets were fabricated at LLE by Mark Bonino. Dan Haberberger assisted with setup of Angular Filter Refractometry. The author carried out all data analysis presented in this chapter.

- Chapter 5: Matt Trantham performed the 2D CRASH simulations presented in this chapter, with input from Tim Handy. Erez Raicher, Hilik Frank and Moshe Fraenkel conceived of the approach to incorporate non-LTE ionization and opacity tables into CRASH, which was implemented by Bart van der Holst. The author carried out all analysis of results, with input from Dov Shvarts.

- Chapter 6: The author carried out all analysis presented in this chapter, much of which relied on physical models proposed by others.

- Chapter 7: The author was the principal investigator for the experiments presented in this chapter. He designed the targets, which were machined by Rob Gillespie and fabricated by Sallee Klein at the University of Michigan. The author also designed the Ross-pair filter system and carried out all data analysis presented.

1.8 Description of Subsequent Chapters

Chapter 2: This chapter outlines the basic physics of long-pulse lasers interacting with underdense plasmas, with an overview of plasma waves, laser propagation in plasma and LPIs. Simple derivations of single and multi-beam TPD are provided, along with a general discussion of growth rates, thresholds and convective gains for several instabilities.

Chapter 3: This chapter presents an overview of film and image-plate x-ray detectors used in imaging HEDP experiments. Experiments performed on the OMEGA-60 laser are presented, studying the origin of the hard x-ray background in backlit pinhole imaging.

Chapter 4: Experiments on the OMEGA-EP laser are introduced, studying hot electron production from LPIs in high-Z plasmas from laser-irradiated planar foils. We describe hard x-ray measurements from which we infer properties of hot electrons generated in the foil targets. Measurements using Angular Filter Refractometry to image the expanding plasmas are also presented, as well as modeling of the data to reconstruct electron density profiles and calculate gradient length-scales.

Chapter 5: This chapter presents results from 2D radiation hydrodynamic simulations that are compared to the measured density profiles from Ch. 4. The results of these simulations are used in Ch. 6 to predict how the plasma conditions varied across materials to interpret the hot-electron measurements in Ch. 4.

Chapter 6: Models are proposed for hot-electron production observed in Ch. 4. We speculate on the importance of nonlinear saturation mechanisms and Landau damping in determining the hot-electron temperatures inferred from measurements. The results of the simulations from Ch. 5 are used to predict the importance of various laser-plasma instabilities to understand inferred hot-electron levels.

Chapter 7: This chapter describes experiments performed on OMEGA-60 to mitigate LPIs and hard x-ray background from hot electrons in backlit pinhole imagers. New pinhole imager designs were tested in which the scaffold material holding the microdot was changed from low-Z CH to higher Z Al and V, based on the results from Ch. 4 showing mitigation of hard x-rays under similar changes. Incident x-ray spectra are measured and used to estimate signal-to-background ratios on radiographs.

Chapter 8: This chapter summarizes the findings and conclusions of this thesis and provides perspectives on future work.

CHAPTER 2

Laser-Plasma Interactions

This chapter provides an overview of the interaction of intense lasers with plasmas, with the goal of elucidating the necessary physical relations to describe experimental results that follow in subsequent chapters.

2.1 Description of a plasma

Ordinary matter dissociates into its constituent charged particles when their kinetic energy is greater than the electrostatic energy binding electrons to nuclei within atoms, or ions to each other within molecules. As the density of charged particles becomes large in a net-neutral ensemble, the small-scale fluctuations in electric field will be shielded out over distances on the order of the Debye length,

$$\lambda_D = \sqrt{\frac{\varepsilon_0 T_e}{n_e e^2}}, \tag{2.1}$$

where ε_0 is the vacuum permittivity, and e, T_e and n_e are the electron charge, temperature (in energy units) and density, respectively. Such an ensemble is known as a plasma and behaves collectively under the influence of electromagnetic forces, as long as particle collisions are small compared to the plasma frequency, $\omega_{pe} = \sqrt{e^2 n_e / m_e \varepsilon_0}$. The collective behavior of plasmas gives rise to many complex phenomena, and in particular, the excitation and propagation of intrinsic waves as described next in Sec 2.2. In addition, the collective behavior is important in understanding a plasmas' interaction with intense electromagnetic radiation (e.g. laser light).

2.2 The two-fluid model of a plasma and plasma waves

The most detailed description of a plasma would involve keeping track of each particles' position and velocity separately at all times, t. This procedure is impractical for nearly all applications; a truncated approach—known as kinetic modeling—is to describe the k^{th} species of a plasma in terms of its distribution function, $f_k(\mathbf{r}, \mathbf{v}, t)$ in position $(\mathbf{r})$ and velocity $(\mathbf{v})$ space. The evolution of each species' 7-dimensional distribution function can be modeled by a Boltzmann equation accounting for the relevant forces due to both self-consistent and applied electric $(\mathbf{E})$ and magnetic $(\mathbf{B})$ fields as well as collisions with other particles. The vast majority of interesting problems using this kinetic approach still require numerical solutions arrived at with powerful computing resources. A further simplification is to track macroscopic fluid-like quantities that can be acquired by taking particle velocity moments of the distribution function. For example, the zeroth moment gives the particle density, $n_k(\mathbf{r}, t) = \int f_k(\mathbf{r}, \mathbf{v}, t) d^3\mathbf{v}$, and the first moment gives the average velocity, $\mathbf{u}_k(\mathbf{r}, t) = \frac{1}{n_k} \int \mathbf{v} f_k(\mathbf{r}, \mathbf{v}, t) d^3\mathbf{v}$ at each point in space at a given time. One can arrive at the Euler fluid conservation equations for mass, momentum and energy describing the evolution of such quantities by similarly taking moments of the Boltzmann equation for each species:

$$
\begin{aligned}
\frac{\partial n_k}{\partial t} + \nabla \cdot (n_k \mathbf{u}_k) &= 0 && (2.2)\\
m_k n_k \left(\frac{\partial \mathbf{u}_k}{\partial t} + (\mathbf{u}_k \cdot \nabla)\mathbf{u}_k \right) &= -\nabla p_k + q_k n_k \left(\mathbf{E} + \mathbf{u}_k \times \mathbf{B}\right) - \sum_\alpha \mathbf{R}_{k\alpha}, && (2.3)\\
\text{and} \quad \frac{3}{2}\left(\frac{\partial p_k}{\partial t} + \nabla \cdot (p_k \mathbf{u}_k) \right) &= -p_k \nabla \cdot \mathbf{u}_k - \nabla \cdot \mathbf{Q}_k + S_k && (2.4)
\end{aligned}
$$

where m_k, q_k and p_k are the mass, electric charge and pressure of the species, respectively. (The pressure has been taken to be a scalar here, but in general is a rank-2 tensor, $\overline{\overline{P}}_k$.) In addition, the quantity $\mathbf{R}_{k\alpha} = \nu_{k\alpha}(\mathbf{u}_k - \mathbf{u}_\alpha)$ is a drag term accounting for elastic collisions between species k and α, $\mathbf{Q}_k$ is the particle heat flux and S_k are energy sources or sinks. Equations 2.2-2.4 are closed with an appropriate equation of state (Equation of State (EOS)), which for a plasma is well-approximated by that of an ideal gas, $p_k = n_k T_k$ at temperature, T_k. Much behavior concerning the interaction of lasers having $I_L \lambda_0^2 < 10^{15}\,\mathrm{W}\mu\mathrm{m}^2/\mathrm{cm}^2$ with plasmas can be described using a “two-fluid” approach, combining a set of conservation equations for both electrons and ions with Maxwell’s equations. However, this description breaks down when the local velocity distributions are significantly modified by mechanisms such as wave-particle interactions (Sec. 2.7) and nonlocal transport of particles.

2.2.1 Electron plasma waves

Charge density fluctuations can be excited in a plasma from thermal noise or an applied field and will propagate as electrostatic (compressional) waves in the presence of a finite pressure. For a small-amplitude, high-frequency fluctuation in electron density, n_1, we have $n_e = n_1 + n_{e0}$ with $n_1 \ll n_{e0}$ where the background electron density, n_{e0}, varies slowly in space and time relative to n_1. Because of their much larger mass, the ions are assumed to be immobile and simply provide a neutralizing background density, $n_{i0} = n_{e0}/Z_i$, where Z_i is the charge state. For high-frequency fluctuations, the phase velocities of the waves are much larger than the electron thermal velocity ($\omega/k \gg v_e = \sqrt{T_e/m_e}$) and the compressions are adiabatic. Hence, $p_e/n_e^{\gamma_e} =$ const., where $\gamma_e = (N+2)/N$ is the polytropic index for an electron gas with N degrees of freedom. We can plug $n_e(\mathbf{r}, t)$ into Eqs. 2.2 and 2.3 and combine the two, assuming an unmagnetized, collisionless plasma. Making use of Poisson's equation, $\varepsilon_0 \nabla \cdot \mathbf{E} = e(n_e - Z_i n_i)$ and keeping only first-order terms we get the wave equation,

$$\frac{\partial^2 n_1}{\partial t^2} = \frac{e^2 n_{e0}}{\varepsilon_0 m_e} n_1 + \frac{\gamma_e T_e}{m_e} \nabla^2 n_1. \tag{2.5}$$

Considering only a single Fourier mode for simplification, $n_1 \sim \exp(\mathrm{i}\mathbf{k} \cdot \mathbf{r} - \mathrm{i}\omega t)$, we can arrive at the dispersion relation,

$$\omega^2 = \omega_{pe}^2 + 3v_e^2 k^2 \tag{2.6}$$

$$= \omega_{pe}^2 \left(1 + 3k^2 \lambda_D^2\right), \tag{2.7}$$

where $\gamma_e = 3$ has been used for the 1D motion of these longitudinal modes. This is also known as the Bohm-Gross dispersion relation for electron plasma waves (EPWs), also known as Langmuir waves (LWs). Larger k (smaller λ) results in larger pressure gradients and vice versa, implying that as the wavelength shortens, the wave will propagate faster. However, the group velocity will always be less than the thermal speed, due to the opposing electrostatic restoring force as thermal electrons stream from higher to lower pressure regions.

2.2.2 Ion acoustic waves

When the density fluctuations have a much lower-frequency ($v_i \ll \omega/k \ll v_e$), the ions have time to respond to electron motion and both the electron- and ion-fluid motion must be considered. Using a similar procedure as before, inserting a perturbed ion density, $n_i = n_{i0} + n_{i1}$ into Eqs. 2.2 and 2.3 and combining the two we have

$$\frac{\partial^2 n_{i1}}{\partial t^2} = \frac{Z_i e n_{i0}}{m_i}\nabla \cdot \mathbf{E} + \frac{\gamma_i T_i}{m_i}\nabla^2 n_{i1}. \tag{2.8}$$

In the presence of an electron pressure gradient, electrons will drift from ions and set up a space-charge electric field,

$$e n_e \mathbf{E} = -\nabla p_e, \tag{2.9}$$

where electron inertia has been neglected with respect to the ions. Inserting this into Eq. 2.8, we then get

$$\frac{\partial^2 n_{i1}}{\partial t^2} = \frac{\gamma_e Z_i T_e + \gamma_i T_i}{m_i}\nabla^2 n_{i1}, \tag{2.10}$$

and the corresponding dispersion relation,

$$\omega^2 = c_s^2 k^2 \tag{2.11}$$

for ion acoustic waves (IAWs), where $c_s = \sqrt{(\gamma_e Z_i T_e + \gamma_i T_i)/m_i}$ is the ion acoustic sound speed. Since in the regime $v_i \ll \omega/k \ll v_e$ ions behave adiabatically in 1D and electrons are isothermal, we have $\gamma_i = 3$ and effectively, $\gamma_e = 1$.

2.3 Electromagnetic waves in plasma

Electromagnetic (EM) waves can be absorbed, reflected, refracted, as well as scattered in a plasma. All these features make EM radiation a useful probe of plasma conditions. The dispersion relation for an EM wave of frequency, ω_0 in a plasma is

$$\omega_0^2 = \omega_{pe}^2 \frac{1 - \mathrm{i}\nu_{ei}/\omega_0}{1 + (\nu_{ei}/\omega_0)^2} + c^2 k^2, \tag{2.12}$$

where c is the speed of light, and ν_{ei} is the electron-ion collision frequency, given by Eq. 1.1 when the plasma electrons are Maxwellian-distributed. Damping through electron-ion collisions has been included here because it describes the primary mechanism by which laser energy is absorbed in the plasmas: *inverse bremsstrahlung*. Without the presence of ions, the average velocity of an electron in a laser's oscillating electric field will be zero, and it gains zero net energy over a single period. If the electron can scatter off an ion's Coulomb potential, however, it will transfer some of its momentum into the direction perpendicular to the laser's electric field, gaining net energy during the oscillation. Setting the wavenumber to $k = k_0 + \mathrm{i}\kappa_{IB}/2$, the real part, k_0 becomes

$$k_0 = \sqrt{1 - \frac{n_e}{n_c\left(1 - (\nu_{ei}/\omega_0)^2\right)}}. \tag{2.13}$$

We can see that as n_e approaches $\sim$the critical density, n_c (Eq. 1.4) that k_0 goes to zero, at which point the EM wave reflects in the plasma. Below and above n_c, the plasma is referred to as *underdense* and *overdense*, respectively. The quantity κ_{IB} is the inverse-bremsstrahlung absorption coefficient given by Eq. 1.2. In the underdense plasma, transmission and absorption of EM radiation with intensity $I(s)$ along the path coordinate s in the plasma is described by the radiative transfer equation neglecting re-emission of radiation,

$$\frac{dI}{ds} = -\kappa_{IB} I(s), \tag{2.14}$$

with the solution

$$I(s) = I_o \exp\left(-\int_{s_o}^{s} \kappa_{IB}(s')ds'\right) \tag{2.15}$$

where $I_o = I(s_o)$.

To understand refraction in a plasma, we can look at the phase velocity of the wave, v_p. Neglecting collisions altogether,

$$v_p = \frac{\omega_0}{k_0} = \frac{c}{\sqrt{1 - n_e/n_c}} \tag{2.16}$$

$$\approx c\left(1 + \frac{n_e}{2n_c}\right), \tag{2.17}$$

where Eq. 2.17 is accurate to within 5% when $n_e \lesssim n_c/3$. The dependence of v_p on electron density implies that in an inhomogeneous plasma, an initially smooth wavefront will distort as the phase advances more quickly in denser regions compared to in those that are more rarefied. The distortion results in the EM wave refracting through the plasma at varying angles along the wavefront. Over a distance L the phase-difference $\Delta\phi(x, y)$ accumulated is the difference in phase between that from an EM wave propagating through plasma and one propagating in vacuum. For a low-density plasma this is given approximately by

$$\Delta\phi(x, y) = \int_{z=0}^{L} (k_0 - \omega_0/c)dz \tag{2.18}$$

$$\approx \frac{\pi}{n_c \lambda_0} \int_{z=0}^{L} n_e(x, y, z)dz. \tag{2.19}$$

Here, λ_0 is the wavelength of the EM wave in vacuum, where it is assumed to propagate in the $+z$ direction. The corresponding refraction angle, θ_α, into the $\alpha = x, y$ direction is a measure of the phase gradient,

$$\theta_\alpha = \frac{\lambda_0}{2\pi}\frac{\partial \Delta\phi}{\partial \alpha} \tag{2.20}$$

$$= \frac{1}{2n_c}\frac{\partial}{\partial \alpha}\int_{z=0}^{L} n_e(x,y,z)dz. \tag{2.21}$$

For a ray passing through a plasma whose density only varies along one dimension, y say, the angle of refraction perpendicular to this direction, $\theta(y)$ can be related to the angle of incidence in vacuum, θ_v via Snell's law,

$$\sin\theta(y) = \frac{\sin\theta_v}{\sqrt{1 - n_e(y)/n_c}}. \tag{2.22}$$

This results in a turning point of the EM wave in an inhomogeneous plasma at the density $n_c \cos^2\theta_v$.

2.4 Wave-wave interactions and parametric instabilities

Multiple waves can resonantly interact with one another in a plasma, through the nonlinear coupling to density perturbations. Of primary interest for the plasmas studied in this thesis are three-wave interactions that occur when the driving lasers resonantly decay into scattered light waves, EPWs and/or IAWs. Physically, the laser light wave will displace electrons in a density perturbation, producing a transverse current and space-charge electric fields. The transverse current can excite a scattered light wave, and the space-charge fields can excite EPWs. The laser's electric field will beat with the fields of these waves, resulting in a ponderomotive force that increases the magnitude of density perturbations and hence, the coupling strength between the laser and excited waves.

When the growth rate exceeds the rate of damping, the decay waves will grow unstably until saturation mechanisms become important. This phenomenon is known as *parametric instability.* For three-wave parametric instabilities, the wave providing the energy to drive the instability is referred to as the *pump* (the laser, here) with subscript 0 and the driven waves are referred to as the *decay* or *daughter* waves, with subscripts 1 and 2. The three waves can resonantly interact when they are in-phase, given by the matching conditions,

$$\omega_0 = \omega_1 + \omega_2 \tag{2.23}$$

$$\mathbf{k}_0 = \mathbf{k}_1 + \mathbf{k}_2. \tag{2.24}$$

The most common three-wave parametric instabilities in the context of laser-produced plasmas are *Stimulated Raman Scattering* (SRS), for a decay into a scattered light wave and EPW, *Stimulated Brillouin Scattering* (Stimulated Brillouin Scattering (SBS)), for a decay into a scattered light wave and IAW, and *Two-Plasmon Decay* (TPD) for a decay into two EPWs. As discussed in Ch. 1, all of these instabilities typically are undesirable for ICF. For example, SRS and SBS scatter laser light out of underdense plasma region, diverting energy away from compressing the fuel. In addition, SBS can seed a phenomenon known as *cross-beam energy transfer* (CBET), whereby intersecting laser beams can couple energy to one-another through ion density perturbations [78]. This energy transfer can alter the irradiance profile around the capsule in direct-drive and the hohlraum wall in indirect drive ICF, degrading implosion symmetry. Growth of SRS and TPD can also divert drive energy away from inverse-bremsstrahlung absorption of the laser energy. However, some of this energy may be recovered as an anomalous absorption mechanism, by collisional damping of the large-amplitude EPWs [68]. A major concern of SRS and TPD is that the large-amplitude EPWs generated can produce hot electrons through Landau damping and other nonlinear wave-particle interactions (Sec. 2.7) [56,79]. As mentioned previously, the hot electrons themselves can further degrade the implosion by penetrating deep into the fuel and heat it, reducing the efficiency of compression, and can also produce hard x-ray background on diagnostics.

2.5 Two-plasmon decay

To further outline the basic physics of LPIs, we now derive the dispersion relations and growth rates of TPD driven by both single and multiple laser beams using the two-fluid description of a plasma [69, 80]. The basic procedure that follows can be used to arrive at the dispersion relations and growth rates of SRS and SBS as well.

In TPD, the matching conditions, together with the EPW dispersion relations give

$$\omega_0 = \sqrt{\omega_{pe}^2(1+3\lambda_D k_1^2)} + \sqrt{\omega_{pe}^2(1+3\lambda_D k_2^2)} \tag{2.25}$$

$$\Rightarrow \omega_0 \approx 2\omega_{pe} \tag{2.26}$$

since $\lambda_D k_{1,2} \lesssim 0.3$ for Landau-damping to be weak enough for waves to grow (Sec. 2.7). We conclude that the TPD instability only occurs in the neighborhood of the quarter-critical density ($n_e \approx n_c/4$). We also see from Eq. 2.25 that EPWs with small wavevectors and large phase-velocities, $v_p = \omega_{1,2}/k_{1,2}$ are generated closer to $n_c/4$ than EPWs with large wavevectors, which occur at lower densities.

To derive the TPD dispersion relation and growth rate, we linearize the electron fluid equations, defining $n_e = n_{e0} + n_p$. Here n_p is a small perturbation on the electron density field and, in general, may consist of a variety of modes arising from thermal fluctuations. The electron fluid velocity, $\mathbf{u}_e = \mathbf{u}_p + \mathbf{v}_{\text{os}}$ is made up of a longitudinal component, $\mathbf{u}_p$ and transverse component, $\mathbf{v}_{\text{os}}$ equal to the electron oscillation velocity in the laser's EM field, where $\partial \mathbf{v}_{\text{os}}/\partial t = -e\mathbf{E}_0/m_e$. We insert these definitions of n_e and $\mathbf{u}_e$ into Eqs. 2.2 and 2.3, to get the linearized forms of the continuity and momentum equations. Further defining the longitudinal component $\mathbf{u}_p = \nabla\psi$, where ψ is a velocity potential, and using the identity, $(\mathbf{u}\cdot\nabla)\mathbf{u} = \nabla(u^2/2) + (\nabla\times\mathbf{u})\times\mathbf{u}$, we get,

$$\frac{\partial n_p}{\partial t} + n_{e0}\nabla^2\psi + \mathbf{v}_{\text{os}}\cdot\nabla n_p + \nabla\psi\cdot\nabla n_{e0} = 0 \tag{2.27}$$

$$\frac{\partial \psi}{\partial t} - \frac{e}{m_e}\phi + \frac{3v_e^2}{n_{e0}}n_p + (\mathbf{v}_{\text{os}}\cdot\nabla\psi) = 0 \tag{2.28}$$

$$\nabla^2\phi = en_p/\varepsilon_0, \tag{2.29}$$

for the general inhomogeneous case where $\nabla n_{e0} \neq 0$ with mean background density N_0. The substitutions, $\mathbf{E} = -\nabla\phi - \frac{m_e}{e}\frac{\partial \mathbf{v}_{\text{os}}}{\partial t}$ and $\mathbf{B} = \frac{-m_e}{e}\nabla\times\mathbf{v}_{\text{os}}$ have been made where ϕ here is the electrostatic potential from n_p, and again the adiabatic EOS has been used with $\gamma_e = 3$. Damping has also been neglected for simplicity but its effect can be added in later trivially. Equations 2.27 and 2.28 comprise the typical starting point to analyze the behavior of TPD in a variety of regimes [80–82].

We can arrive at a wave equation for ψ by taking $\frac{\partial}{\partial t}$ of 2.28 and substituting in $\frac{\partial n_p}{\partial t}$ from 2.27. A similar procedure applies for n_p, but swapping operations between the two equations. In the end, we get,

$$\left[\frac{\partial^2}{\partial t^2} - 3v_e^2\left(\nabla^2 + \frac{1}{n_{e0}}\nabla n_{e0}\cdot\nabla\right) + 2\mathbf{v}_{\text{os}}\cdot\nabla\frac{\partial}{\partial t} + \frac{\partial \mathbf{v}_{\text{os}}}{\partial t}\nabla\right]\psi = \frac{e}{m_e}\left[\frac{\partial}{\partial t} + \mathbf{v}_{\text{os}}\cdot\nabla\right]\phi \tag{2.30}$$

$$\left[\frac{\partial^2}{\partial t^2} + \omega_{pe}^2\frac{n_{e0}}{N_0} - 3v_e^2\left(\nabla^2 + \frac{1}{n_{e0}}\nabla n_{e0}\cdot\nabla\right) + \frac{\partial}{\partial t}\left(\mathbf{v}_{\text{os}}\cdot\nabla\psi\right)\right]n_p = \nabla\left[n_{e0}\nabla\left(\mathbf{v}_{\text{os}}\cdot\nabla\psi\right)\right] - \frac{e}{m_e}\nabla n_{e0}\cdot\nabla\phi, \tag{2.31}$$

where 2nd-order terms in v_0 have been dropped since $v_0 \ll v_e$ for the laser intensities and temperatures of interest.

2.5.1 Single-beam, homogeneous TPD

Following closely to Ref. [69], we now consider a plane EM wave,

$$\mathbf{v}_{\mathrm{os}} = \frac{1}{2}\mathbf{v}_0 \left[e^{\mathrm{i}(\mathbf{k}_0\cdot\mathbf{r}-\omega_0 t)} + e^{-\mathrm{i}(\mathbf{k}_0\cdot\mathbf{r}-\omega_0 t)}\right] \tag{2.32}$$

propagating through a homogeneous plasma ($\nabla n_{e0} = 0$, $n_{e0} = N_0$) and neglect pump-depletion by the growing decay waves. Inserting Eq. 2.32 into Eq. 2.31 and taking the Fourier transform, we find

$$\begin{aligned}\left(-\omega^2 + \omega_{pe}^2 + 3v_e^2k^2\right)\tilde{n}_p(\mathbf{k},\omega) =& \frac{\omega}{2}\mathbf{k}\cdot\mathbf{v}_0\left[\tilde{n}_p\left(\mathbf{k}-\mathbf{k}_0,\omega-\omega_0\right) + \tilde{n}_p\left(\mathbf{k}+\mathbf{k}_0,\omega+\omega_0\right)\right] \\ &+ \frac{N_0k^2}{2}\mathbf{k}\cdot\mathbf{v}_0\left[\tilde{\psi}\left(\mathbf{k}-\mathbf{k}_0,\omega-\omega_0\right) + \tilde{\psi}\left(\mathbf{k}+\mathbf{k}_0,\omega+\omega_0\right)\right],\end{aligned} \tag{2.33}$$

where the tilde represents a quantity's Fourier transform. Therefore, $\tilde{n}_p$ provides the amplitudes of *all* EPWs present, i.e. both waves driven and un-driven by the laser. We can simplify Eq. 2.33 making use of the continuity equation, 2.27 to find $\tilde{\psi}$:

$$\tilde{\psi}(\mathbf{k},\omega) \approx \frac{\omega}{k^2}\frac{\tilde{n}_p(\mathbf{k},\omega)}{N_0}, \tag{2.34}$$

which gives

$$\begin{aligned}D(\mathbf{k},\omega)\tilde{n}_p(\mathbf{k},\omega) =& -\frac{\mathbf{k}\cdot\mathbf{v}_0}{2}\frac{\omega\left(\mathbf{k}-\mathbf{k}_0\right)^2 + k^2\left(\omega-\omega_0\right)}{\left(\mathbf{k}-\mathbf{k}_0\right)^2} \\ &\times\left[\tilde{n}_p\left(\mathbf{k}-\mathbf{k}_0,\omega-\omega_0\right) + \tilde{n}_p\left(\mathbf{k}+\mathbf{k}_0,\omega+\omega_0\right)\right],\end{aligned} \tag{2.35}$$

simplifying with the Bohm-Gross dispersion relation,

$$D(\mathbf{k}, \omega) = \omega^2 - \omega_{pe}^2 - 3v_e^2 k^2. \tag{2.36}$$

We can see by comparing the left- and right-hand sides of Eq. 2.35 that EPWs at $(\mathbf{k}, \omega)$ are driven by the laser beating ponderomotively with EPWs at $(\mathbf{k} \pm \mathbf{k}_0, \omega \pm \omega_0)$. However, as a result of the wave-matching conditions, only the $(\mathbf{k} - \mathbf{k}_0, \omega - \omega_0)$ modes are resonant, and hence the $(\mathbf{k} + \mathbf{k}_0, \omega + \omega_0)$ terms can be dropped from Eq. 2.35. By substituting $\mathbf{k} \to \mathbf{k} - \mathbf{k}_0$ and $\omega \to \omega - \omega_0$, we arrive at the corresponding equation for the $(\mathbf{k} - \mathbf{k}_0, \omega - \omega_0)$ mode:

$$D(\mathbf{k} - \mathbf{k}_0, \omega - \omega_0)\tilde{n}_p(\mathbf{k} - \mathbf{k}_0, \omega - \omega_0) = -\frac{\mathbf{k} \cdot \mathbf{v}_0}{2} \frac{\omega\,(\mathbf{k} - \mathbf{k}_0)^2 + k^2\,(\omega - \omega_0)}{k^2} \tilde{n}_p\,(\mathbf{k}, \omega) \tag{2.37}$$

where the $(\mathbf{k} - 2\mathbf{k}_0, \omega - 2\omega_0)$ term has been dropped as non-resonant. Combining Eqs. 2.35 and 2.37, and using the wave-matching and EPW dispersion relations, approximating $\omega \approx \omega_0 - \omega \approx \omega_{pe}$ on the RHS, we find

$$D(\mathbf{k}, \omega) D(\mathbf{k} - \mathbf{k}_0, \omega - \omega_0) = \left(\frac{\mathbf{k} \cdot \mathbf{v}_0 \omega_{pe}}{2}\right)^2 \left[\frac{(\mathbf{k} - \mathbf{k}_0)^2 - k^2}{k\,|\mathbf{k} - \mathbf{k}_0|}\right]^2, \tag{2.38}$$

which is the TPD dispersion relation for EPWs excited by a single laser beam interacting in a homogeneous plasma. The homogeneous temporal growth rate, γ_0 for the two EPWs can be found by setting $\omega = \omega_r + \mathrm{i}\gamma_0$ in the Bohm-Gross dispersion relation,

$$D(\mathbf{k}, \omega_r + \mathrm{i}\gamma_0) \approx \omega_r^2 + 2\mathrm{i}\omega_r\gamma_0 - \left(\omega_{pe}^2 + 3v_e^2 k^2\right) \tag{2.39}$$

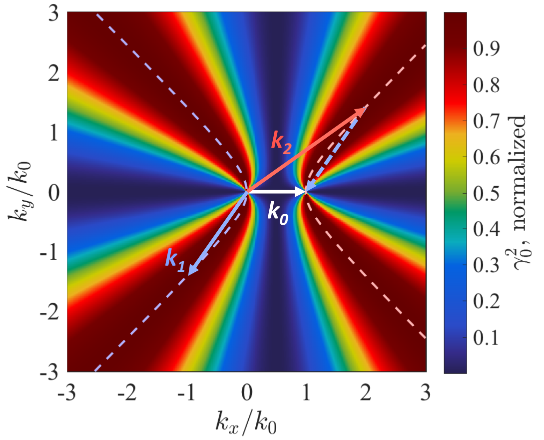

Figure 2.1: The normalized homogeneous temporal growth rate squared, γ_0^2 for single-beam TPD in k-space. Arrows represent a decay diagram of the laser $(\mathbf{k}_0)$ into decay EPWs ($\mathbf{k}_1$ and $\mathbf{k}_2$) along the maximum-growth hyperbolas from Eq. 2.41.

assuming $\gamma_0 \ll \omega_r$. For normal modes of the plasma (i.e. when $\omega_r^2 = \omega_{pe}^2 + 3v_e^2k^2$), we find the well-known result from the TPD dispersion relation,

$$\gamma_0 = \frac{|\mathbf{k}\cdot\mathbf{v}_0|}{4}\frac{|(\mathbf{k}-\mathbf{k}_0)^2 - k^2|}{k\,|\mathbf{k}-\mathbf{k}_0|}. \tag{2.40}$$

The TPD homogeneous growth rate squared is shown in Fig. 2.1 in the plane of polarization, where $\mathbf{k}_0$ has been chosen to lie along the x-axis. The overlaying arrows represent a decay of the laser $(\mathbf{k}_0)$ into two EPWs ($\mathbf{k}_1$ and $\mathbf{k}_2$) at maximum growth, represented by the hyperbolas in this plane,

$$k_x = \frac{1}{2}\Big(k_0 \pm \sqrt{k_0^2 + 4k_y^2}\Big). \tag{2.41}$$

We can see from Eq. 2.40 that for a single beam, plasma waves traveling parallel to $\mathbf{k}_0$ cannot grow, due to there being no electric field component in this direction. When $k \gg$

k_0 the maximum TPD single-beam growth rate (squared) is given by

$$\begin{aligned}\left(\gamma_0^2\right)_{\max} &= \left(\frac{k_0 v_0}{4}\right)^2 \\ &= \frac{2}{c n_c m_e}\left(\frac{k_0}{2}\right)^2 I \end{aligned} \tag{2.42}$$

where I is the laser irradiance.

2.5.2 Multi-beam TPD

When multiple laser beams overlap in the neighborhood of $n_c/4$, they can cooperatively drive resonant EPWs [57,83] through the TPD instability. This is shown pictorially with a wave-diagram in Fig. 2.2a, where the *common* EPW with wavevector $\mathbf{k}_c$ is shared between two lasers with wavevectors $\mathbf{k}_{01}$ and $\mathbf{k}_{02}$. For N plane-wave laser beams with frequency, ω_0 that are in-phase, the electron oscillation velocity is,

$$\mathbf{v}_{\text{os}} = \frac{1}{2}\sum_i^N \mathbf{v}_{0i}\left[e^{\mathrm{i}(\mathbf{k}_{0i}\cdot\mathbf{r}-\omega_0 t)} + e^{-\mathrm{i}(\mathbf{k}_{0i}\cdot\mathbf{r}-\omega_0 t)}\right] \tag{2.43}$$

For the common wave with wave vector, $\mathbf{k}_c$, and frequency, ω_c Eq. 2.35 becomes

$$D(\mathbf{k}_c,\omega_c)\tilde{n}_p(\mathbf{k}_c,\omega_c) = -\frac{\mathbf{k}_c}{2}\cdot\sum_i^N \mathbf{v}_{0i}\left[\frac{\omega_c\left(\mathbf{k}_c-\mathbf{k}_{0i}\right)^2 + (\omega_c-\omega_0)k_c^2}{\left(\mathbf{k}_c-\mathbf{k}_{0i}\right)^2}\right]\tilde{n}_p(\mathbf{k}_c-\mathbf{k}_{0i},\omega_c-\omega_0), \tag{2.44}$$

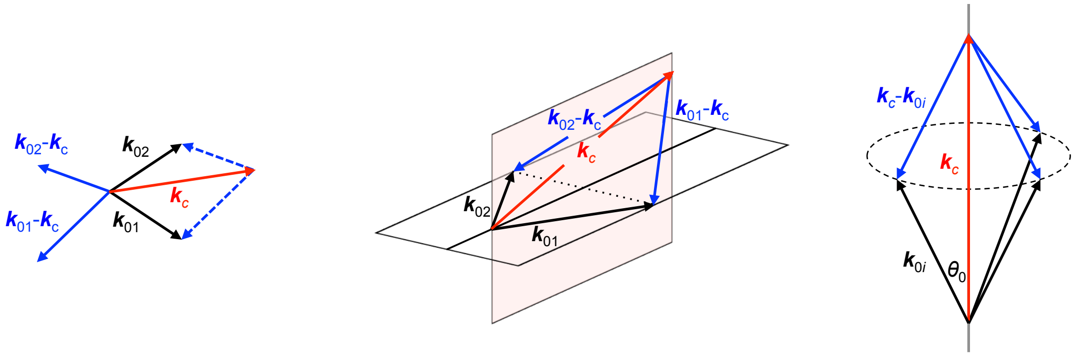

a) b) c)

Figure 2.2: a) General decay diagram for two laser beams ($\mathbf{k}_{01}$ and $\mathbf{k}_{02}$) sharing a common EPW, $\mathbf{k}_c$. Regions of common-wave maximum growth geometries for b) two laser beams and c) more than two laser beams.

and for the $(\mathbf{k}_c - \mathbf{k}_{0i}, \omega_c - \omega_0)$ modes,

$$\begin{aligned} &D(\mathbf{k}_c - \mathbf{k}_{0i}, \omega_c - \omega_0)\tilde{n}_p(\mathbf{k}_c - \mathbf{k}_{0i}, \omega_c - \omega_0) = \\ &-\frac{(\mathbf{k}_c - \mathbf{k}_{0i})}{2} \cdot \sum_j^N \mathbf{v}_{0j} \left[\left\{ (\omega_c - \omega_0) + \frac{(\mathbf{k}_c - \mathbf{k}_{0i})^2 (\omega_c - 2\omega_0)}{(\mathbf{k}_c - \mathbf{k}_{0i} - \mathbf{k}_{0j})^2} \right\} \tilde{n}_p(\mathbf{k}_c - \mathbf{k}_{0i} - \mathbf{k}_{0j}, \omega_c - 2\omega_0) \right. \\ &\qquad \left. + \left\{ (\omega_c - \omega_0) + \frac{(\mathbf{k}_c - \mathbf{k}_{0i})^2 \omega_c}{(\mathbf{k}_c - \mathbf{k}_{0i} + \mathbf{k}_{0j})^2} \right\} \tilde{n}_p(\mathbf{k}_c - \mathbf{k}_{0i} + \mathbf{k}_{0j}, \omega_c) \right]. \end{aligned} \tag{2.45}$$

On the RHS, the $(\mathbf{k}_c - \mathbf{k}_{0i} - \mathbf{k}_{0j}, \omega_c - 2\omega_0)$ modes will always be non-resonant and can be dropped. The $(\mathbf{k}_c - \mathbf{k}_{0i} + \mathbf{k}_{0j}, \omega_c)$ modes will only be resonant when $j = i$, from which Eq. 2.45 simplifies to Eq. 2.37 at $(\mathbf{k}, \omega) = (\mathbf{k}_c, \omega_c)$, replacing $\mathbf{k}_0$ and $\mathbf{v}_0$ with $\mathbf{k}_{0i}$ and $\mathbf{v}_{0i}$, respectively. Substituting the simplified form of Eq. 2.45 into Eq. 2.44 and canceling $\tilde{n}_p(\mathbf{k}_c, \omega_c)$ on both sides,

$$D(\mathbf{k}_c, \omega_c) = \sum_i^N \frac{(\mathbf{k}_c \cdot \mathbf{v}_{0i})^2}{4} \left[\frac{\omega_c (\mathbf{k}_c - \mathbf{k}_{0i})^2 + (\omega_c - \omega_0) k_c^2}{k_c (\mathbf{k}_c - \mathbf{k}_{0i})} \right]^2 \frac{1}{D(\mathbf{k}_c - \mathbf{k}_{0i}, \omega_c - \omega_0)}. \tag{2.46}$$

Approximating $\omega_c \approx \omega_0 - \omega_c \approx \omega_{pe}$ in the bracketed term as before leads to the multi-beam TPD dispersion relation,

$$D(\mathbf{k}_c, \omega_c) = \omega_{pe}^2 \sum_i^N \frac{4\gamma_{0i}^2}{D(\mathbf{k}_c - \mathbf{k}_{0i}, \omega_c - \omega_0)} \tag{2.47}$$

where γ_{0i} is the homogeneous temporal growth rate for the i^{th} beam with irradiance I_i. We can solve for the multi-beam growth rate of the common EPWs by again including an imaginary component $\mathrm{i}\gamma$ in each mode's frequency with $\gamma \ll \omega_r$. To keep notation consistent with [57], we set $\omega_c \to \omega_c + \mathrm{i}\gamma$ and $\omega_0 - \omega_c \to \omega_0 - \omega_c + \mathrm{i}\gamma$ in the dispersion relations. When the common wave is a normal mode (i.e. $\omega_c^2 = \omega_{pe}^2 + 3v_e^2 k_c^2$), then Eq. 2.47 becomes

$$2\mathrm{i}\omega_c\gamma = \omega_{pe}^2 \sum_i^N \frac{4\gamma_{0i}^2}{(\omega_c - \omega_0)^2 - \omega_{pe}^2 - 3v_e^2(\mathbf{k_c} - \mathbf{k}_{0i})^2 + 2\mathrm{i}(\omega_c - \omega_0)\gamma}. \tag{2.48}$$

The growth rate is a maximum when the denominator in the summation is a minimum, which occurs when the dispersion relation from the matching conditions between lasers and common EPW,

$$(\omega_0 - \omega_c)^2 = \omega_{pe}^2 + 3v_e^2(\mathbf{k}_c - \mathbf{k}_{0i})^2 \tag{2.49}$$

is satisfied for all $(\mathbf{k}_c - \mathbf{k}_{0i})$ modes. This happens when all the participating laser beams share the same angle relative to the common waves,

$$\frac{\mathbf{k}_c \cdot (\mathbf{k}_c - \mathbf{k}_{0i})}{k_c|\mathbf{k}_c - \mathbf{k}_{0i}|} = \cos\theta, \text{ for } i = 1, ..., N. \tag{2.50}$$

When two laser beams drive a common wave, the region of maximum growth is limited to the plane bisecting the beams' wavevectors (Fig. 2.1b). For more than two beams, the region of maximum growth is the line defining the axis of a cone that all the beams lie along (Fig. 2.1c). Once Eq. 2.50 is satisfied, the multi-beam growth rate becomes simply

$$(\gamma_0^2)^{\mathrm{MB}} = \sum_i^N \gamma_{0i}^2. \tag{2.51}$$

Evidently the growth of common EPWs depends on the total overlapped irradiance of participating laser beams, $I_\Sigma = \sum_i^N I_i$, rather than the single beam irradiance, leading to larger growth and lower thresholds, depending on the beam geometry and polarizations. To highlight this latter dependence, the multi-beam growth rate can be normalized by the maximum single-beam growth rate squared–Eq. 2.42 evaluated at the total overlapped laser irradiance [57]. The normalized homogeneous TPD multi-beam growth rate then is

$$\left(\Gamma_0^2\right)^{\mathrm{MB}} = \frac{(\gamma_0^2)^{\mathrm{MB}}}{(\gamma_0^2)^{\mathrm{SB}}_{\mathrm{max}}\big|_{I_\Sigma}} \tag{2.52}$$

$$= f_c(\mathbf{k}_c, \theta) \sum_i^N \frac{I_i}{I_\Sigma} \cos^2 \alpha_i \tag{2.53}$$

where

$$f_c(\mathbf{k}_c, \theta) = \frac{k_c^2 - (\mathbf{k}_c - \mathbf{k}_{0i})^2}{k_0 |\mathbf{k}_c - \mathbf{k}_{0i}|} \tag{2.54}$$

and α_i is the angle between the i^{th} beam's polarization vector and $\mathbf{k}_c$ and whose θ-dependence follows from Eq. 2.50. In the case of polarization-smoothed beams, Eq. 2.53 becomes

$$\left(\Gamma_0^2\right)^{\mathrm{MB}}_{\mathrm{PS}} = \frac{1}{2} f_c \sin^2 \theta, \tag{2.55}$$

arrived at by averaging over α_i for each beam [57].

Table 2.1: Laser-plasma instabilities and their growth rates. Subscripts “s”, “p” and “iaw” stand for scattered light wave, electron plasma wave and ion-acoustic wave, respectively. ω_i is the ion plasma frequency.

Instability	Decay Waves	Maximum Growth Rate, γ_0
Stimulated Raman Scattering (SRS)	EMW + EPW	$\sqrt{\frac{\omega_{pe}^2}{\omega_\mathrm{s}\omega_\mathrm{p}}}\frac{k_\mathrm{p}v_\mathrm{os}}{4}$
Stimulated Brillouin Scattering (SBS)	EMW + IAW	$\sqrt{\frac{\omega_{pi}^2}{\omega_\mathrm{s}c_s k_\mathrm{iaw}}}\frac{k_\mathrm{iaw}v_\mathrm{os}}{4}$
Two-Plasmon Decay (TPD)	EPW + EPW	$\frac{k_0 v_\mathrm{os}}{4}$

2.5.3 Multi-beam SRS

A recent model has been proposed suggesting that EPWs may also be driven by multiple laser beams through SRS [84]. The model shares many qualities with the theory of multiple-beam TPD discussed above, where the primary difference is that the $(\mathbf{k}_{0i} - \mathbf{k}_c, \omega_0 - \omega_c)$ modes are scattered light waves in the instability’s more likely form, rather than EPWs. As in multi-beam TPD, the common EPWs in multi-beam SRS must also satisfy Eq. 2.50. A result similar to Eq. 2.51 is found relating the growth rate of common waves from SRS to the individual-beam growth rates for EPWs in oblique SRS.

2.6 Growth rates and instability threshold

The growth rates of other laser-plasma instabilities can be found similarly as was done for TPD, upon deriving the dispersion relation for the coupled modes. The results are given in Table 2.1. These are the undamped rates for modes that grow everywhere in time, which are termed *absolutely unstable* (Fig. 2.3, left). Without damping, we may expect *any* amount of thermal noise to grow exponentially, unabated. For a 0.35-μm laser with an irradiance of $\sim 10^{14}$ W/cm^2, the maximum TPD growth rate is $\sim 10^{13}$ s^{-1}, and would lead to the complete depletion of laser energy virtually instantaneously for a nanosecond pulse. This does not happen in reality because damping mechanisms set a threshold intensity

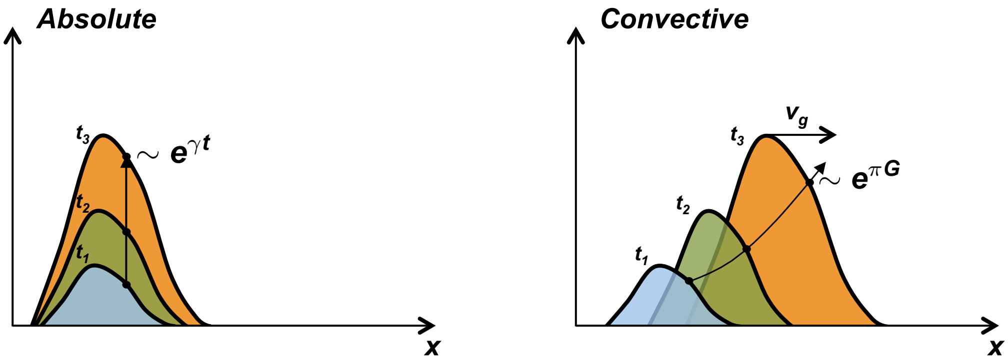

Figure 2.3: Left: Absolute instability, where an initial disturbance grows everywhere in time, t at the homogeneous growth rate, γ. Right: Convective instability, where an initial disturbance grows by a finite amount, $\exp(\pi G)$ as it propagates in space.

that the laser must exceed to transfer net energy to the decay waves, and at large enough amplitudes, nonlinear mechanisms will set in and eventually saturate the instability. To include the effect of damping, we can add the terms $2\nu_1\frac{\partial}{\partial t}$ and $2\nu_2\frac{\partial}{\partial t}$ the wave equations for decay waves 1 and 2, respectively, where $\nu_{1,2}$ is the amplitude damping rate for each wave. The result is the substitution $\omega^2 \rightarrow \omega(\omega + 2\mathrm{i}\nu_{1,2})$ in each waves' dispersion relation (e.g. Eq. 2.36 for EPWs). Following the previous instability analysis with this substitution we would arrive at the general threshold condition [69],

$$\gamma_0^2 \geq \nu_1\nu_2. \tag{2.56}$$

In many cases, damping rates ν_1 and ν_2 arise simply from collisions and Landau damping in the case of EPWs and IAWs. However, finite density gradients in an inhomogeneous plasma can spoil phase-matching between the three waves, resulting in an effective damping as the decay waves convect out of the resonance region at their group velocities, v_{g1} and v_{g2} along the gradient. Assuming the gradient is in the x direction, the wavenumber mismatch is

$$\kappa(x) = k_{0x}(x) - k_{1x}(x) - k_{2x}(x), \tag{2.57}$$

defining $\kappa(0) = 0$. This type of damping leads to a finite growth region, over which a seed pulse is *convectively unstable* (Fig. 2.3, right), growing as it propagates by a factor $\sim \exp(\pi G_c)$, where

$$G_c = \frac{\gamma_0^2}{|\kappa' v_{g1} v_{g2}|} \tag{2.58}$$

and is known as the Rosenbluth or convective gain [68]. Here, κ' is the spatial derivative of the wavenumber mismatch. Collisional and Landau damping have been neglected. A typical method for arriving at this result is to solve the equations for coupled oscillators in the steady-state WKB approximation, assuming linear dependence of the wavenumber mismatch, i.e. $\kappa(x) \approx \kappa' x$. We can find G_c by evaluating κ' and γ_0 of the growing modes for a particular instability. In TPD, we have

$$\begin{aligned}
\kappa'(x) &= \frac{\partial k_0}{\partial x} - \frac{\partial k_{1x}}{\partial x} - \frac{\partial k_{2x}}{\partial x} \\
&= \left(-\frac{1}{2c^2 k_0} + \frac{1}{6v_e^2 k_{1x}} + \frac{1}{6v_e^2 k_{2x}} \right) \frac{d\omega_{pe}^2(x)}{dx} \\
&\approx \frac{1}{6v_e^2} \frac{d\omega_{pe}^2(x)}{dx} \left(\frac{1}{k_{1x}} + \frac{1}{k_{2x}} \right).
\end{aligned} \tag{2.59}$$

Approximating the density profile as linearly varying in x with gradient length-scale L_n near $n_c/4$, i.e. $\omega_{pe}^2(x) \approx \omega_{pe0}^2(1 + x/L_n)$ where ω_{pe0} is the plasma frequency evaluated at the background electron density, N_0, we have

$$\kappa' \approx \frac{\omega_{pe0}^2}{6v_e^2 L_n} \left(\frac{1}{k_{1x}} + \frac{1}{k_{2x}} \right). \tag{2.60}$$

Substituting this expression in Eq. 2.58 along with $v_{g1,2} \approx 3v_e^2 k_{1,2x}/\omega_{pe0}$, and $k_{1x} + k_{2x} = k_0$, the convective gain becomes,

$$G_c = \frac{2\gamma_0^2 L_n}{3v_e^2 k_0}. \tag{2.61}$$

The gain evaluated for the waves along the hyperbola of maximum growth is

$$G_c = 6 \times 10^{-2} \frac{I L_n \lambda_0}{T_e}, \tag{2.62}$$

Here, I is in units of 10^{14} W/cm^2, L_n and λ_0 are in microns and T_e is in keV, and all are evaluated near $n_c/4$. For multi-beam TPD, the gain simply becomes [83]

$$G_c = 6 \times 10^{-2} \frac{I_\Sigma L_n \lambda_0}{T_e} \left(\Gamma_0^2\right)_{\text{max}}^{\text{MB}}. \tag{2.63}$$

For both cases, we note the proportionality to $I L_n \lambda_0 / T_e$; physically, a longer length-scale implies a larger resonance volume over which phase-matching between waves can occur. A lower temperature decreases the EPWs' group velocities, allowing the waves to spend more time propagating through the resonance volume, leading to larger growth. As well, higher laser irradiances provide more energy flux to drive the EPWs. In SRS, the convective gain is similarly proportional to $I L_n$ and does not depend on T_e to first order. This is because the scattered light wave convects out of the growth region at close to the speed of light–much faster than the EPW.

The threshold for the convective modes can be calculated by setting $G_c = 2$ for a minimum of $\exp(2\pi)$ amplification [57]. The resulting multi-beam TPD convective threshold, $I_{c,\text{TPD}}^{\text{MB}}$ is

$$I_{c,\text{TPD}}^{\text{MB}} \geq \frac{94.9 T_e}{L_n \lambda_0 \left(\Gamma_0^2\right)_{\text{max}}^{\text{MB}}}. \tag{2.64}$$

Plasma inhomogeneity similarly affects absolutely unstable modes in LPIs. In TPD, the absolute threshold from inhomogeneity was calculated by Simon [81],

$$I_{\text{abs,TPD}} \geq \frac{81.9T_e}{L_n\lambda_0}, \tag{2.65}$$

where the units of the parameters are the same as those given above. In SRS backscatter, the absolute threshold from inhomogeneity is

$$I_{\text{abs,SRS}} \geq \frac{807}{\lambda_0^{2/3}L_n^{4/3}}. \tag{2.66}$$

2.6.1 Multi-beam LPIs and hot electrons

For multi-beam experiments, growing evidence has demonstrated that the measured fraction of laser energy, E_L converted to hot electrons, $f_{\text{hot}} = E_{\text{hot}}/E_L$, depends on the overlapped intensity, I_Σ of beams that can drive common EPWs, rather than a single beam's intensity [57, 83, 85–87]. Measured f_{hot}'s from CH targets were shown to scale with the TPD common-wave convective gain G_c for a multi-beam geometry with the interpretation that hot electrons are being accelerated by convectively-growing EPWs originating from the TPD common-wave process [83]. Recently, direct observation of multi-beam TPD was reported using Thomson scattering to measure amplitudes of common waves [88].

Recent observations of hot-electron beaming in indirect drive experiments have suggested the presence of multi-beam SRS [62] in the hohlraum LEH. Hard x-ray images showed electron acceleration to be highly directed along the hohlraum axis in the case of low density gas-fill hohlraums when TPD was predicted not to occur because densities were well below $n_c/4$. The observations were consistent with the presence of multi-beam SRS, which would only generate EPWs along the hohlraum axis. For higher density gas-fill hohlraums, with average densities closer to $n_c/4$, electron acceleration was observed to be more isotropic, consistent with the presence of non-common EPWs in multi-beam TPD that could have a variety of directions.

2.7 Wave-particle interactions

As EPWs and IAWs grow to large amplitudes, they can resonantly interact with the individual electrons and ions in the plasma. Electrons moving near an EPW's phase velocity, ω/k can be decelerated or accelerated by the wave's electric field. When more electrons exist with velocities slightly below than with velocities slightly above ω/k, e.g. in a Maxwellian distribution, the distribution around ω/k will flatten. This mechanism is referred to as Landau damping, because the electrons remove net energy from the wave. The rate of Landau damping of the EPW amplitude in a Maxwellian plasma is [89]

$$\nu_L(k) = \sqrt{\frac{\pi}{8}} \frac{\omega}{(k\lambda_D)^3} \exp\left[-\frac{1}{2}\left(\frac{1}{(k\lambda_D)^2} + 3\right)\right], \tag{2.67}$$

which becomes large for waves with $k\lambda_D \gtrsim 0.3$, known as the *Landau cutoff*. IAWs may also undergo Landau damping in a plasma when the ion-acoustic sound speed, c_s is close to the ion thermal velocity $v_i = \sqrt{T_i/m_i}$, occurring when $\langle Z\rangle T_e/T_i \sim 1$.

Electrons can be accelerated to very high energies via Landau damping, resulting in the populations of hot electrons observed in many experiments. Particle-in-cell simulations predict that hot electron production via Landau damping occurs predominantly in the nonlinear regime of TPD. The broad spectrum of EPWs that exists serves to stage-accelerate electrons from short-wavelength/low-phase velocity EPWs to large-wavelength/high-phase velocity EPWs [55]. Plasma inhomogeneity can make the acceleration process more efficient since an EPW's phase velocity increases as it travels up the density gradient.

As an EPW grows to large amplitude, it can also accelerate initially cold electrons very efficiently to velocities on the order of ω/k, into resonance with the wave. This is known as wave-breaking, and provides additional damping of EPWs.

CHAPTER 3

Investigation of Hard X-ray Background in Backlit Pinhole Imagers

This chapter begins with an overview of x-ray detectors used in high-energy-density physics experiments. Experiments are presented to study the origin of hard x-ray background in backlit pinhole imagers. This work was adopted from the article, "Investigation of the hard x-ray background in backlit pinhole imagers" published by the author in *Review of Scientific Instruments*, 2016 [65]. A quantitative description is also provided to demonstrate how the hard x-ray background present in radiography introduces uncertainties in estimates of optical depth or density of an imaged object.

3.1 Detection of X-rays

In laser-driven experiments, instruments and detectors must be able to discriminate among the large fluxes of energetic particles, such as visible photons, x-rays, electrons and neutrons, that are emitted in many directions to gain detailed information about the experiment. In addition to x-ray imaging, detectors used in most x-ray spectroscopic measurements must be position-sensitive to record spectrally dispersed x-rays. Commonly used position-sensitive x-ray detectors include x-ray film, image plates (IPs), x-ray CCDs and micro-channel plates (MCPs)–all of which rely principally on the local deposition of x-ray energy via photoelectric absorption in a sensitive layer. Film and IPs are attractive in many experiments because they are virtually unaffected by the large EMPs generated by laser-plasma interactions that create overwhelming noise on solid state-based detectors and in their electronic components.

X-ray film contains a sensitive emulsion layer consisting of densely packed silver-halide grains (typically AgBr) suspended in gelatin. When a grain absorbs an incident x-ray photoelectrically, it is reduced to create metallic silver crystals. Usually only a single photon need be absorbed for this to occur. The formed silver crystals are then developed into a permanent image using chemical agents that remove unexposed silver-halide grains. The image is darkest at the most-exposed areas, where light is absorbed or highly scattered by the random crystal orientations. Film exposure is typically calculated in terms of the optical density, $\mathrm{OD} = -\log_{10} T$, where T is the fraction of light transmitted through the developed film. For the experiments presented in this thesis Perkin-Elmer PDS microdensitometer measured the film OD and created a digitized image with pixel size 22 μm. The spatial resolution and dynamic range of film scale with grain density and sensitivity scales with grain size. The film development process and cosmic rays produce an inherent uniform background on film, known as fog, and is subtracted off in any quantitative analysis presented in this thesis unless otherwise noted.

In image plates, x-rays interact in a layer containing BaF(Br,I):Eu^{2+} phosphor crystals suspended in plastic. As x-rays are absorbed photoelectrically, they liberate electrons from the Eu^{2+} ions that become trapped in lattice defects. Irradiation of the IP with a red laser stimulates local emission of blue photons from the recombination of trapped electrons with Eu^{3+} ions. This photo-stimulated luminescence (PSL) can be detected and amplified using a photomultiplier tube that scans over the image plate with the laser [90]. The result is a digitized image where the pixel intensity, measured in units of PSL is proportional to the deposited energy. The trapped electron-Eu^{3+} ion pair is in a meta-stable state, that

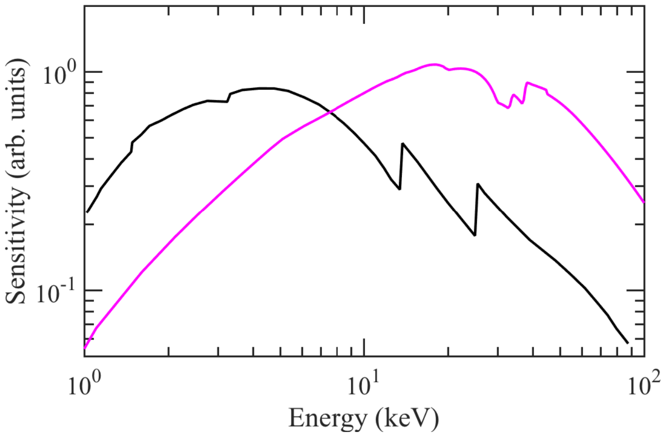

Figure 3.1: Spectral sensitivities of DEF x-ray film (black) from Brown et al. [2] and the MS-type image plate (magenta) calculated using GEANT4 and provided by Barukh Yaakobi at the Laboratory for Laser Energetics.

decays on the order of tens of minutes. Therefore, IPs are typically scanned within $\sim$an hour of exposure to avoid signal fade. Spatial resolution of IPs is limited by (1) the intrinsic energy transport of ionizing radiation in the sensitive layer and (2) scattering of the red laser photons and stimulated blue photons at the IP surface or within the different detector layers; it is typically worse than what can be achieved with x-ray film [91]. Despite this, IPs are preferable over film in many experiments due to their higher detective quantum efficiency, high dynamic range of 5 orders of magnitude, dose linearity, re-usability and lack of chemical development [90, 92, 93]. They are also fairly versatile, being sensitive to other forms of ionizing radiation, such as electrons, ions and neutrons because of their reliance on the production of free electrons to form excited states.

The spectral sensitivities of Kodak Direct Exposure Film (DEF) film (black) and Fuji MS-type IP (magenta) are plotted in Fig. 3.1. The IP sensitivity peaks at higher energies than the film sensitivity in part because of more efficient absorption at higher energies from the presence of high-Z Eu ions. As a result, IPs are more susceptible than film to image degradation from hard x-ray background when the goal is to detect primarily $4-7$ keV x-rays in experimental diagnosis.

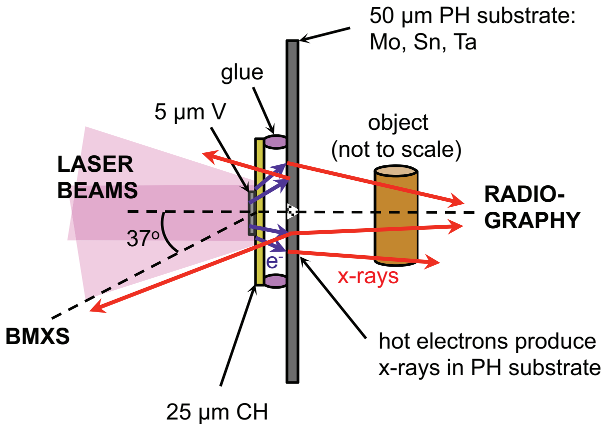

Figure 3.2: Side-on schematic of the backlit pinhole imager target, and orientation relative to experimental diagnostics, laser beams and an imaged object.

3.2 Experiments on OMEGA

Previous work has demonstrated the presence of hard x-rays in the direction of the radiograph in backlit pinhole imagers [42]. It was suspected that hot electrons generated via laser-plasma instabilities in the foil and scaffold plasmas underwent collisions in the high-Z pinhole (PH) substrate, inducing $\gtrsim$10 keV bremsstrahlung and Kα x-rays that reach the radiograph [32, 37].

Here we present additional evidence for a hard x-ray background produced in backlit pinhole imagers from experiments performed on the OMEGA-60 laser. We confirm that the hard x-ray background observed on radiographs comes from the pinhole imager targets. However, we find it plausible that the hard x-rays were only produced in the irradiated target components, rather than the PH substrate.

A schematic of the backlit pinhole imagers used in this experiment is shown in Fig. 3.2. A 5-μm thick, 300-μm diameter V foil (microdot) sits atop a 25-μm$\times$4-mm square CH scaffold fixed a distance 500 μm from the PH substrate. Upon irradiation, the V microdot emits strongly at the 5.18 keV He-α line. The PH substrate is 50-μm$\times$7-mm square and has a tapered PH with 20-μm minimum diameter. The material of the PH substrate was varied in an attempt to alter the spectrum of x-rays produced in the substrate when bombarded with hard x-rays generated by hot electrons, or with the hot electrons themselves. For the data presented here, 5 targets had Ta, 1 had Mo and 1 had a Sn PH substrate. It was hypothesized that if electrons were interacting with the PH substrate, a difference in the hard x-ray signal could be detected between materials.

This investigation of the hard x-ray background in pinhole imagers was a ride-along to a larger experiment studying plasma flows from a laser-irradiated wedge target. In total, three targets were irradiated by lasers during each shot; two orthogonal backlit pinhole imagers and the wedge target. Orthogonal backlighting was used to diagnose a sheet of plasma produced in the wedge target.

The targets were driven by 1-ns square pulses consisting of five laser beams at 351-nm wavelength. A total laser energy, $E_L \sim$ 2.25 kJ was delivered into an 800-μm laser spot, for a corresponding irradiance of 4.5×10^{14} W/cm^2 with less than 6% shot-to-shot variation. The beams were smoothed by distributed phase plates and polarization smoothing. Hot electrons with temperatures in the range $\sim 10 - 30$ keV have been observed from the irradiation of plastic targets with similar laser parameters [87, 94].

3.2.1 Radiography

Radiographs were recorded on 2 layers of Afga D7 film and a Fuji BAS MS-type image plate, stacked such that the film was closer to the target. Parylene fiducial steps were used to calibrate the integrated signal, in order to isolate the signal's distinct spectral contributions. Figure 3.3a shows a radiograph recorded on the image plate of the fiducial steps adjacent to the plasma flow. We note the low contrast in these steps despite recorded signals well above the noise. The right side of the radiograph was over-exposed by emission coming directly from the plasma corona in the wedge target. Radiographs from shots in which the wedge target was un-driven indicated that this emission only produced the localized exposure and did not contaminate the rest of the detector.

The average of the signal over each step is shown as the red points in Fig. 3.3b vs the step's optical depth for the 5.18 keV He-α x-rays, τ_α. Similar to previous analyses [1,13,14], we modeled the total signal as a quasi-monoenergetic source of 5.18 keV x-rays, I_α with an underlying background contribution, I_{BG} that had negligible attenuation through the steps in comparison. Using the Beer-Lambert law, the total signal is then

$$I_{\text{tot}}(\tau_\alpha) = I_\alpha e^{-\tau_\alpha} + I_{BG}. \tag{3.1}$$

The result of this fit is shown by the black solid line, which gives the expected signal vs. optical depth for the He-α x-rays, where the dashed lines are the one-sigma error bars. According to this model, the background was estimated to be almost twice the desirable He-α signal. Over all shots in this experiment, we estimated signal-to-background ratios on the image plate between 1:5 and 1:1 with uncertainty in the background as large as 20% of the desirable signal. The signal-to-background ratio on the film after subtracting off fog was on average 3.4:1.

The presence of the high-energy background on the detector both reduces the dynamic range available for the desirable signal and introduces significant uncertainty in optical depth-estimates of the object that is being imaged (e.g. the plasma flow here). We use the simple model of Eq. 3.1 to calculate the magnitude of this uncertainty. Lower uncertainties may be achieved with a more complicated model, but this requires additional fiducial measurements that take up usable imaging space in the radiograph. Rearranging Eq. 3.1 for optical depth, we have

$$\tau_\alpha = -\ln\left(\frac{I_{\text{tot}} - I_{BG}}{I_\alpha}\right). \tag{3.2}$$

Measurement error in the signal, δI_{tot} propagates through the fit as standard errors, δI_α

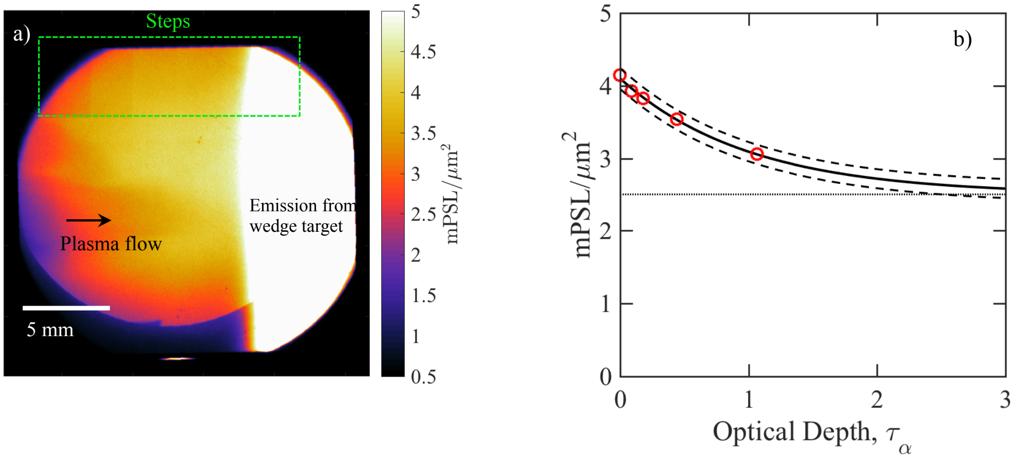

Figure 3.3: a) Radiograph recorded on image plate showing parylene calibration steps adjacent to plasma flow, from shot 69936. b) Beer's law fit to the step intensities (red circles), showing the expected signal as a function of an object's depth at the V He-α energy.

and δI_{BG}. These, in-turn, lead to uncertainty in τ_α. From simple error propagation in Eq. 3.2, we have

$$\begin{aligned}\delta\tau_\alpha^2 &= (\delta I_{\text{tot}}^2 + \delta I_{BG}^2)\frac{1}{(I_{\text{tot}} - I_{BG})^2} + \left(\frac{\delta I_\alpha}{I_\alpha}\right)^2 \\ &= (\delta I_{\text{tot}}^2 + \delta I_{BG}^2)\frac{e^{2\tau_\alpha}}{I_\alpha^2} + \left(\frac{\delta I_\alpha}{I_\alpha}\right)^2 \end{aligned} \tag{3.3}$$

To interpret this result, we plot the relative error, $\delta\tau_\alpha/\tau_\alpha$ against the optical depth of an "unknown" object, shown in Figs. 3.4a-b. Here, values of I_α, I_{BG}, and their respective errors were estimated from fits to calibration step data for shot 69936 on a) film and b) the IP, respectively. The black lines represent the error for the nominal case *with* background, and the red lines represent the error for the same magnitude He-α signal, but with I_{BG} and δI_{BG} set to zero. For either case, when $\tau_\alpha \ll 1$, the resulting attenuation is not observable above fluctuations from Poisson statistics of the detected photons, as well as uncertainty in I_α and I_{BG} if $I_{BG} \sim I_\alpha$; therefore, the relative errors are very large. As τ_α increases, the expected change in I_{tot} from attenuation departs significantly from the Poisson fluc-

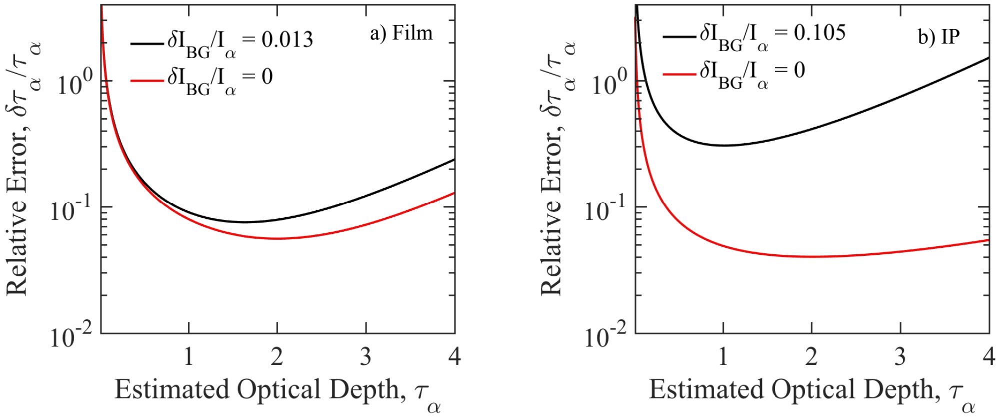

Figure 3.4: Relative error in estimates of optical depth, τ_α of unknown object. Estimates of I_α, I_{BG} and their respective errors are retrieved from fits to measurements of signal behind polystyrene steps, recorded on an a) Agfa D7 film and b) Fuji^{TM} MS-type image plate. Black lines are the nominal case and red lines have I_{BG} set to zero, showing potential improvements for background mitigation.

tuations and background uncertainty and the relative error decreases. Increasing τ_α even further will bring I_{tot} close to I_{BG}, where further changes in signal again become drowned out in particular, by δI_{BG}. The red curves demonstrate the potential improvements from mitigating this background and its associated uncertainty. The majority of improvement comes from eliminating uncertainty in the estimate of background, δI_{BG}. This model

By comparing Figs. 3.4a and b, we can clearly see that the uncertainties in optical depth from the high-energy background are significantly worse for the image plate than the film, due to an order of magnitude increase in $\delta I_{BG}/I_\alpha$. This is in part, a result of image plates being significantly more sensitive than film to hard x-rays with energies >10 keV, relative to lower energy x-rays. Mitigating the hard x-ray background is exceedingly important, therefore, as image plates replace film as the standard x-ray detector in many HEDP experiments for the reasons stated in Sec. 3.1.

In a few radiographs, Eq. 3.1 was a poor model of the total signal on both the image plate and film. For instance, the signal did not always monotonically increase going to thinner steps, which is evidence of signal non-uniformity over the image, potentially in

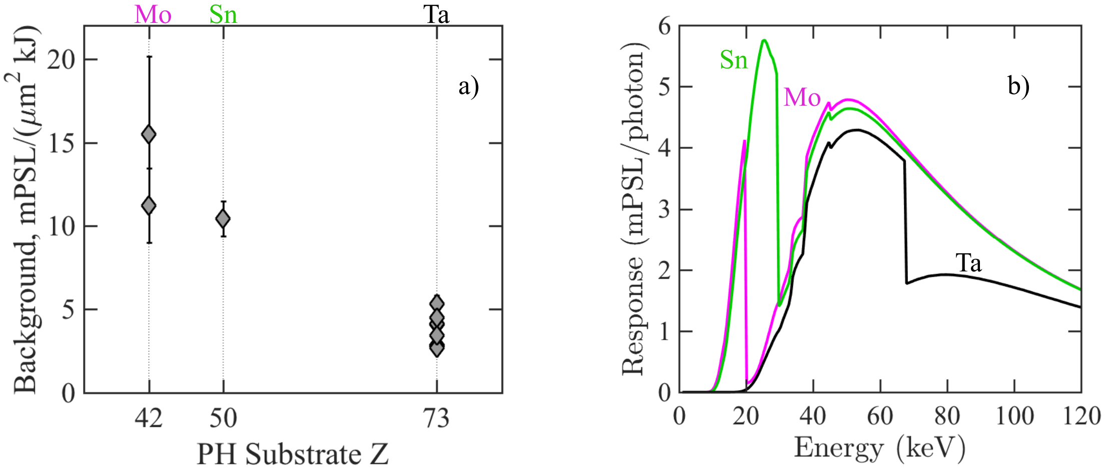

Figure 3.5: a) The comparison of measured Background/Laser energy between different PH substrate materials. b) Response of image plate to x-rays of different energies for the 3 PH substrate materials, calculated as the product of transmission through the PH substrate + filtering and the image plate's spectral sensitivity.

both the He-α and hard x-ray contributions. This observation further motivates gaining a better understanding of the source of x-rays that produces the radiographs.

3.2.2 Varying pinhole substrate material

Figure 3.5 shows the variation of background with PH substrate material by plotting I_{BG}/E_L against material Z. Going from Mo to Ta, I_{BG}/E_L decreases by a factor of $\sim$3, whereas the relative variation between Ta shots is significantly smaller. The first scans of the image plates were saturated in both cases using a Mo PH substrate. As a result, we inferred the background from the second scans, albeit with significantly larger errors.

Using equation 1.9, we estimate that the electron distribution must have a temperature greater than 30 keV for the average electron range to be longer than the 25-μm thickness of the CH scaffold. As well, we expect the majority of electrons that may interact with the PH substrate to lose all their energy within the first few microns. Therefore, any x-rays produced from these interactions would have to transmit through nearly all 50 microns of the PH substrate. Figure 3.5b shows the product of the total transmission through the PH substrate (including the filtering and film preceding the image plate) with the image plate's spectral sensitivity (Fig. 3.1), which we term the "response." The higher transmission and hence, response going from Ta to Sn and Mo is consistent with the increased background from > 10 keV x-rays seen on the radiographs using these substrates. We note, however, that the average image plate response using the Sn PH substrate is higher than when using Mo, which is not consistent with the measured background signals on the radiograph. Additional data are required to understand if the lower background at Sn is real since we only had one target with this material.

The above results add to previous evidence that the source of hard x-ray background from backlit pinhole imagers originates from the region of laser-plasma interactions in these targets. Based on the laser parameters used in this experiment, two-plasmon decay and stimulated Raman scattering are expected to generate hot electrons at the laser spot. Recent two-plasmon decay experimental and theoretical work indicates that the hot electrons are produced primarily at the CH scaffold, rather than the higher-Z V microdot [57, 94].

3.3 Conclusions

Backlit pinhole radiography was performed on the OMEGA laser using V microdots with 5.18 keV probing energy. Significant background from x-rays of energy content well-above 5.18 keV was observed on the radiographs recorded on image plates. Using the Beer-Lambert law to model the radiograph signals, it was demonstrated that the presence of background can lead to large uncertainties in estimates of optical depth. Changing the PH substrate material from Ta to Mo and Sn resulted in higher background on the image plate, consistent with increased transmission of >10 keV x-rays through the lower

Z substrates. We suspect that any LPIs whose hot-electron production contributes to the observed hard x-ray background occurs primarily in the low-Z CH scaffold, rather than the V microdot. More detailed measurements of the spectral content of x-rays incident on the radiograph in Ch. 7 demonstrate this to be the case, but also show that much of the background comes from x-rays produced in the thermal plasma.

CHAPTER 4

Experiments to Study Hot-Electron Production in High-Z Plasmas

This chapter introduces experiments studying hot-electron production from laser-plasma instabilities and its mitigation going from low- to high-Z laser-irradiated targets. The experiments were motivated by the desire to understand and mitigate hot electrons that may lead to hard x-rays in laser-generated x-ray sources, whose presence was evidenced in the previous chapter. Much of the material presented in this chapter and Ch. 6 has been adapted from a manuscript titled, "Mitigation of hot electrons from laser-plasma instabilities in high-Z, highly ionized plasmas," which was accepted to *Physics of Plasmas* in January of 2017.

Past experiments have demonstrated that LPIs can be mitigated by altering plasma conditions at or below $n_c/4$. In Ref. 57, the fraction of laser energy converted to hot electrons, f_{hot} was reduced by a factor of 30 in CH targets when the length-scale was predicted to decrease by a factor of $\sim$2 when switching from planar to a more hydrodynamically-diverging, spherical geometry, both at an overlapped laser irradiance of $I_{\Sigma} = 5{\times}10^{14}$ W/cm^2. In addition, Froula, [87] Hu [94] and Follett [95] all reported a decrease in hard x-ray signal from hot electrons going from low- to mid-Z targets. This was attributed to reduced TPD growth in the mid-Z plasmas. Designs of mid-Z direct-drive capsules have been studied and initial experiments have shown an order of magnitude reduction in hot-electron preheat [96]. The material or Z-dependence of LPIs is linked to (i) a decrease in L_n from slower expansion, (ii) a decrease in I_Σ and increase in T_e through increased laser absorption and (iii) increased electron-ion collisions ($\nu_{ei} \propto Z_{\text{eff}}$, where ν_{ei} is the electron-ion collision rate). Effects (i) and (ii) directly lower gains, while increased collisions can damp the EPWs before they reach large amplitudes. Beyond the linear growth stage, TPD and SRS can depend on Z_{eff} through nonlinear saturation processes whose threshold is set by the Landau damping of IAWs [97, 98]. Zakharov simulations of TPD have shown lower saturation amplitudes of EPWs as well as a decrease in hot-electron production when the IAW damping is lowered [95, 97]. Follett et al. [95] determined this effect to be partially responsible for the observed hot electron levels in irradiated Be capsules.

We extend the previous work on hot electron mitigation by studying its production in planar targets irradiated by multiple lasers beams for materials ranging in average atomic number from 3.5 (CH) to 79 (gold). Hot-electron production is inferred from measurements of hard x-rays produced by electrons interacting in the targets. Refraction imaging is used to measure plasma densities in order to estimate the electron density length-scales which are important in determining thresholds and growth of laser-plasma instabilities. The refraction measurements are also useful to validate radiation-hydrodynamic simulations of laser-produced plasmas. In this chapter, we provide an overview of the experimental techniques and the primary experimental results. A more in-depth interpretation of the experimental results is provided in chapter 6.

4.1 Experimental Geometry

Experiments were performed on the OMEGA EP laser [76] at the Laboratory for Laser Energetics, University of Rochester. Four laser beams of 351-nm light irradiated a planar

Table 4.1: Target materials and thicknesses

Material	CH	Al	Ti	Cu	Mo	Ag	Au
Thickness (μm)	120	60	25	20	25	25	20

foil target 23° from target-normal, producing an expanding plasma (Fig. 4.1a). The beams were linearly polarized with polarization geometry shown in Fig. 4.1b. Each beam was passed through a distributed phase plate, giving an 8th-order super-Gaussian intensity profile with 680-μm FWHM. The laser pulse was 2-ns flat-top with an approximately 240-ps rise time and each beam co-timed to within 50 ps. Beams 1 and 2 had 1.90 ± 0.05 kJ and beams 3 and 4 had 2.25 ± 0.05 kJ energy, resulting in an average overlapped a peak irradiance, $I_{\text{max}} \simeq 1.2{\times}10^{15}$ W/cm^2. The single-layer target materials were: CH, Al, Ti, Cu, Mo, Ag and Au, spanning a wide array of atomic number. Target thicknesses of are listed in Table 4.1 and were chosen based on available materials. A fiducial sphere was attached to the non-irradiated side of the targets to enable spatial registration of the targets for refraction imaging.

4.2 Hard x-ray measurements

Hot electron levels were inferred in these experiments from measurements of hard x-rays produced through the interaction of hot electrons with the foil targets. The HXIP diagnostic, a nine-channel filtered spectrometer [99] recorded time-integrated x-ray dose from x-rays with energies $>$10 keV on a Fuji MS-type image plate. The spectrometer viewed the non-irradiated side of the target at a standoff distance of 49 cm. The channels were separated spatially across a tungsten aperture, illustrated by the scan of an exposed image plate in Fig. 4.2a. The diagnostic was housed in lead shielding nearly an inch thick to reduce background from x-rays produced elsewhere in the target chamber. A blast shield sat in front of the detector, consisting of 25 μm of kapton and 2 mm of polyethylene.

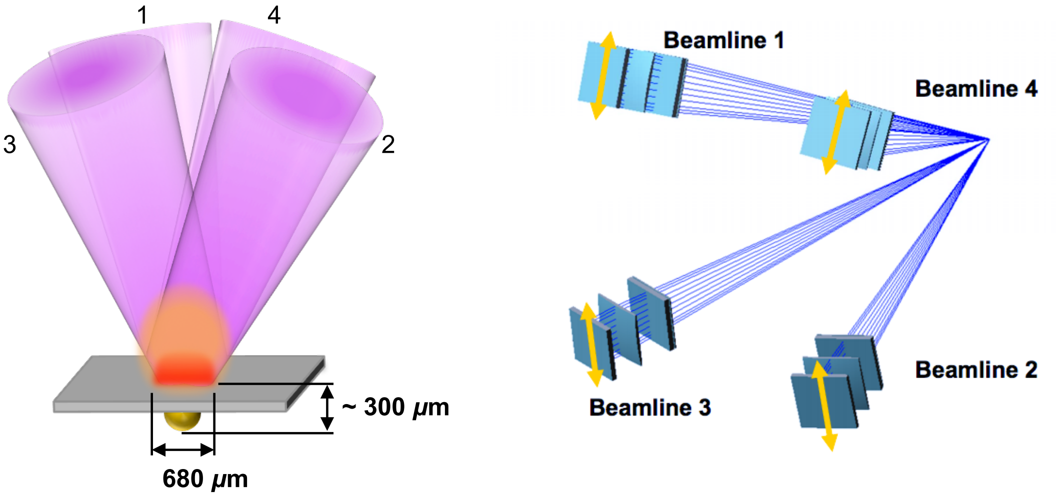

a) b)

Figure 4.1: a) Four Omega EP long-pulse beams irradiate the planar foil targets creating a nearly spherically-symmetric focal spot with FWHM = 680 μm. The fiducial plastic sphere is shown below the foil target. b) Polarization geometry of the four beams. Courtesy of LLE.

Filters for each channel are listed in Table 4.2 and consisted of aluminum and copper with thicknesses varying from 1–20 mm and 0–8 mm, respectively. Even though most electrons were not expected to escape the targets in these experiments, the filtering in front of channel 1 was enough to shield the image plate from electrons with energy up to 1.5 MeV. The response curves, $R(E)$ of each channel are shown in Fig. 4.2b, calculated by multiplying the filter transmission $T(E)$ by the image plate sensitivity, $K(E)$. The transmission was calculated using the NIST XCOM photon cross section libraries [100] and the image plate sensitivity was provided by Barukh Yaakobi at LLE. We see that channels 4 and above are several orders of magnitude less sensitive to energies below 20 keV than channels 1–3. All channels are sensitive to x-rays with energies well above 100 keV.

The total signal for each channel, y_{tot} was calculated as an average over an area of approximately 240×200 pixels, shown as the blue dashed boxes in Fig. 4.2a. Significant background resulted from Compton scatter in the shielding material and the detector housing, which is seen in 4.2a surrounding each of the channels in the shadow of the

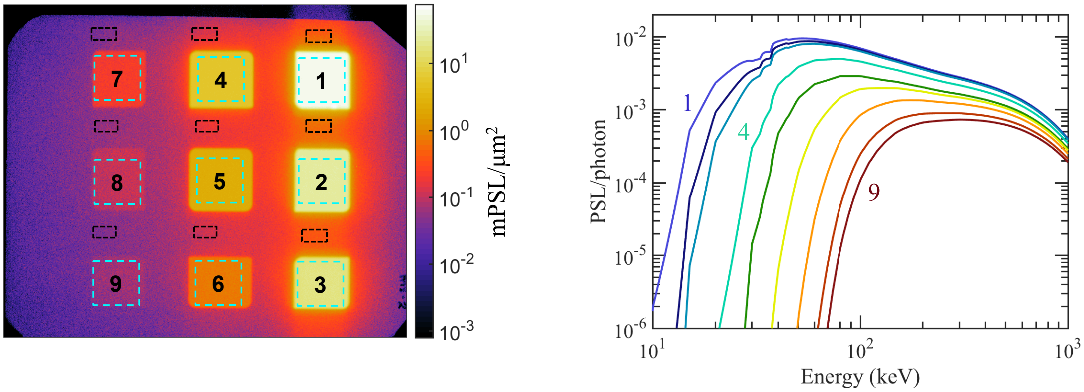

a) b)

Figure 4.2: a) Scan of exposed image plate from the HXIP detector with labeled channels. Signals and background were calculated as averages over the blue and black boxes, respectively. b) Response curves for the 9 channels in the HXIP from the filter transmission multiplied by the IP spectral sensitivity.

aperture. Vertical signal bleed from the scanning process contributed additional background for the least-filtered channels, 1–3. However, this contribution was no more than a few percent of the total in these channels. The total background was taken as an average over an area of roughly 100×30 pixels above each channel, depicted by the black dashed boxes, and this value was subtracted from the channel's total signal. The uncertainty in each signal, $\sigma_y = \sqrt{\sigma_{y,\mathrm{tot}}^2 + \sigma_{\mathrm{BG}}^2}$ was calculated from the standard deviations of the total signal and background over their sampling regions, $\sigma_{y,\mathrm{tot}}$ and σ_{BG}, respectively.

Several of the shots showed channels whose PSL saturated the scanner photomultiplier tubes (PMTs). Since only a fraction of the trapped electron-Eu^{3+} ion pairs recombine during the scanning process, the image plates were rescanned several times until saturation of the PMTs ceased. It was found by comparing unsaturated channels between fade-corrected scans that the signal ratio between the first and n^{th} scans is $(y^{\mathrm{scan}\ 1}/y^{\mathrm{scan}\ \mathrm{n}}) \approx n^{1.65\pm0.20}$. We multiplied the unsaturated signal in later scans that by this factor to infer the unsaturated signal on the first scan.

Table 4.2: Filters and thicknesses for the HXIP spectrometer

Filter material / Channel	1	2	3	4	5	6	7	8	9
Aluminum (mm)	1	2	3	10	20	20	20	20	20
Copper (mm)	0	0	0	0	0	1	3	6	8

4.2.1 Modeling of hard x-ray meaurements

The signal at the i^{th} channel, y_i, was modeled as,

$$\tilde{y}_i = \Omega_{\text{pix}} \int_0^\infty T_i(E) K(E) \frac{d^2 N_x}{dE d\Omega} dE \qquad \text{PSL/pixel,} \tag{4.1}$$

where Ω_{pix} is the solid angle of the detector pixel, $d^2N_x/dEd\Omega$ is the time-averaged incident x-ray spectrum and the transmission $T_i(E)$ includes both that through the i^{th} filter and the blast shield.

We need an appropriate model x-ray spectrum that relates the set of x-ray signals to the distributions of hot electrons produced in the targets. We expected the continuous x-ray spectrum to consist of both a hard component due to bremsstrahlung from hot electrons interacting in the cold target, as well as a softer or "cold" component from the thermal bremsstrahlung radiation emitted by the plasma of expected temperatures between $\sim 1-6$ keV. Line emission from He-like states was also present in several of these plasmas. However, we estimate based on past measurements of He-α conversion efficiencies [17, 18, 101] that this emission would have contributed negligible signal (relative to what was measured) to channels 4 and above on all shots, and 3 and above for all shots except Mo and Ag. Hot electrons can induce cold K-α emission in the Mo, Ag and Au targets with energies 17.5, 22.2 and 68.8 keV, respectively, and all channels are sensitive to these energies. However, we estimate with the simple formula provided in [102] that the total electron energy converted to K-α emission was less than 5$\%$ of that going into bremsstrahlung radiation. Therefore, we were able to neglect line emission in modeling these measurements by selectively fitting to only channels 3 or 4 and above, depending on the target material.

Hard x-ray spectrum

We approximated the hard x-ray spectrum, $S_h(E)$ as thick target bremsstrahlung,

$$S_h(E, T_{\text{hot}}) = E_{\text{hot}} \frac{5 \times 10^{11}}{4\pi} \frac{Z_{\text{nuc}}}{79} \frac{e^{1-E/T_{\text{hot}}}}{E} \frac{\text{photons}}{\text{keV Sr}}. \tag{4.2}$$

from a Maxwellian hot-electron distribution of total energy E_{hot} and temperature, T_{hot} [103]. Upon inferring E_{hot} from a fit to the x-ray measurements we calculated the fraction of laser energy, E_L converted to hot electrons or "hot electron fraction," $f_{\text{hot}} = E_{\text{hot}}/E_L$.

The thick-target approximation is valid if the hot electrons lose the large majority of their energy in the target. Using Eq. 1.9, we estimated that T_{hot} had to be greater than $\sim$ 70 keV in the case of the CH and $\sim$ 90 keV for all other materials in order for the mean electron range to be greater than the target thickness. Since these temperatures are well above what we estimated from our measurements (a posteriori), we expect that most electrons accelerated into the target lost all their energy there. However, electrons initially accelerated away from the target may escape unless they reflux with high efficiency. Refluxing occurs when the electrons remain trapped in the potential created by charge-separation electric fields as they try to escape the target. The fraction of hot electrons that reflux through the target, f_R was calculated using a simple analytic capacitance model developed by Myatt et al. [104]. As the hot electrons leave the target surface, they contribute to a potential, V. Assuming the escaping hot electrons, N_l are Boltzmann-distributed in the potential, we have,

$$N_l = N_e e^{-eV/T_{\text{hot}}}, \tag{4.3}$$

where N_e is the total number of hot electrons, with minimum energy, E_{min}. If we approximate the target as a perfectly-conducting disc of radius, r in vacuum, the capacitance is $C = Q/V = 8\varepsilon_0 r$. Substituting in the total charge lost from the target by escaping electrons, $Q = eN_l$,

$$N_l = 8\varepsilon_0 rV/e \tag{4.4}$$

$$\Rightarrow 8\varepsilon_0 rV/e = N_e e^{-eV/T_{\text{hot}}} \tag{4.5}$$

or

$$\Phi = \kappa e^{-\Phi}, \tag{4.6}$$

where $\Phi = eV/T_{\text{hot}}$, and $\kappa = 8\varepsilon_0 rT_{\text{hot}} \langle E_e \rangle /(e^2 f_{\text{hot}} E_L)$. We have substituted $N_e = f_{\text{hot}} E_L / \langle E_e \rangle$, where E_L is the laser energy and, $\langle E_e \rangle = \int_{E_{\text{min}}}^{\infty} E_e f(E_e, T_{\text{hot}}) dE_e$ is the average hot electron energy from the Maxwellian distribution, $f(E_e, T_{\text{hot}})$. We can solve Eq. 4.6 numerically for Φ at a given value of $\kappa(f_{\text{hot}}, T_{\text{hot}})$, from which we calculate $f_R = 1 - N_l/N_e = 1 - \exp(-\Phi)$. In these experiments, E_L = 8.4 kJ, $r \simeq$ 350 μm (focal spot diameter). For the ranges of T_{hot} ($10 - 100$ keV) and f_{hot} ($\sim 10^{-5} - 10^{-1}$) relevant here, we found $f_R \geq 0.998$, from which we conclude that virtually no electrons escaped. Therefore, f_{hot} should represent the fraction of laser energy converted to the *total* population of hot electrons generated in the target.

Thermal bremsstrahlung emission

The thermal bremsstrahlung emissivity or spectral power emitted per unit mass in a plasma is given by [8]

$$\eta_{\text{ff}} = \frac{16\pi}{3\sqrt{6\pi}} \frac{e^6}{m_e^2 c^3} \frac{\langle Z \rangle^2 n_e}{\sqrt{T_e/m_e} m_i} e^{-E/T_e}, \tag{4.7}$$

and varies significantly throughout the plasma with n_e and T_e. The total spectrum at the detector from this emission involves an integral of Eq. 4.7 over the entire plasma volume along different lines-of-sight, integrated in time and then divided by photon energy. We approximated the overall behavior of the time-integrated thermal bremsstrahlung spectrum as roughly exponential in energy with an effective plasma temperature, T_{cold}. Emission from x-rays generated by EPW-accelerated electrons may also contribute to this cold spectral component. Using a particle-in-cell simulation, Estabrook et al. [105] calculated hot-electron distributions with temperatures on the order of 5 keV, produced by resonance absorption at the critical surface.

The full model of the incident x-ray spectrum is

$$\frac{d^2N_x}{dEd\Omega} = A_{\text{cold}}\frac{e^{-E/T_{\text{cold}}}}{E} + E_{\text{hot}}\frac{5\times10^{11}}{4\pi}\frac{Z_{\text{nuc}}}{79}\frac{e^{1-E/T_{\text{hot}}}}{E}\ \frac{\text{photons}}{\text{keV Sr}}, \tag{4.8}$$

where A_{cold} is a coefficient describing the magnitude of the thermal component, and we fit for A_{cold}, T_{cold}, f_{hot} and T_{hot}. We note that the hot and cold components have essentially identical forms, which were indistinguishable in an optimization procedure without additional information. To converge on a two-temperature solution, we estimated the pair of parameters, $\mathbf{p}_{\text{cold}} = (A_{\text{cold}}, T_{\text{cold}})$, and $\mathbf{p}_{\text{hot}} = (E_{\text{hot}}, T_{\text{hot}})$ for the hot and cold components, respectively, in separate least-squares fits and iterated between the two, rather than fitting for all four parameters simultaneously. This technique of breaking a single optimization problem into two smaller optimization problems improved convergence significantly. Channels 3 through or 4 through 6 (set $\mathbb{N}_{\text{cold}}$) were used to fit for $\mathbf{p}_{\text{cold}}$ and channels 5 through 9 (set $\mathbb{N}_{\text{hot}}$) were used to fit for $\mathbf{p}_{\text{hot}}$. When fitting for one set of parameters, the other set was kept constant in the model spectrum. On the k^{th} iteration, we

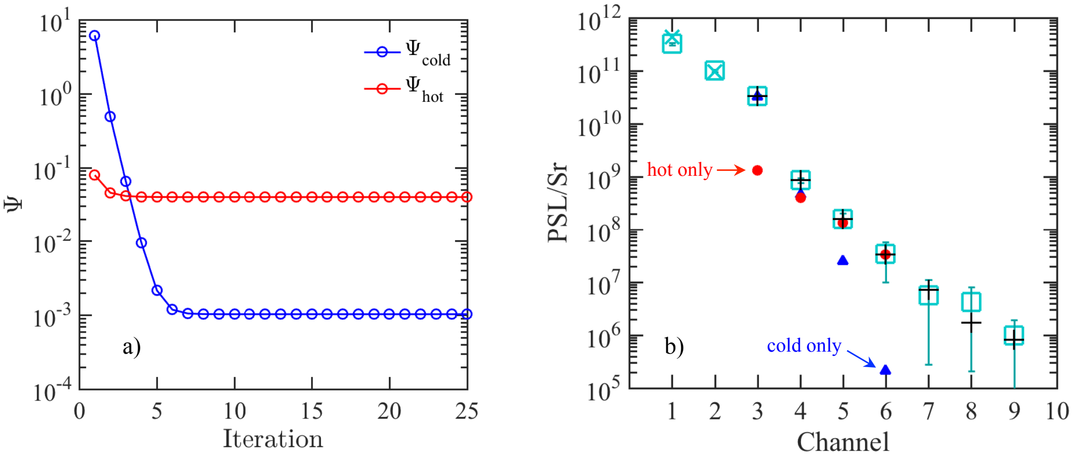

Figure 4.3: a) Weighted least-squares functions that are minimized to estimate $\hat{\mathbf{p}}_{\text{cold}}$ and $\hat{\mathbf{p}}_{\text{hot}}$ vs. iteration in the two-temperature fitting procedure. b) HXIP channel signals from the Ti shot (squares) compared to fitted values (+), where the $\times$'s are the predicted signals of channels not used in the fit (1 and 2 here). The red dots (blue triangles) show the signal contribution from the hot (cold) spectral component only for channels 3 through 6.

solved

$$\hat{\mathbf{p}}^k_{\text{cold}} = \underset{\mathbf{p}_{\text{cold}}}{\text{argmin}} \sum_{i\in\mathbb{N}_{\text{cold}}} \left|\left|\frac{y_i - \tilde{y}_i(\mathbf{p}_{\text{cold}}, \hat{\mathbf{p}}^{k-1}_{\text{hot}})}{\sigma_{y,i}}\right|\right|^2 \tag{4.9}$$

$$\hat{\mathbf{p}}^k_{\text{hot}} = \underset{\mathbf{p}_{\text{hot}}}{\text{argmin}} \sum_{i\in\mathbb{N}_{\text{hot}}} \left|\left|\frac{y_i - \tilde{y}_i(\hat{\mathbf{p}}^{k}_{\text{cold}}, \mathbf{p}_{\text{hot}})}{\sigma_{y,i}}\right|\right|^2, \tag{4.10}$$

where the procedure was initialized with a guess, $\hat{\mathbf{p}}^0_{\text{hot}}$. The values of the weighted least-squares quantities in Eqs. 4.9 and 4.10, which we denote as Ψ_{cold} and Ψ_{hot}, respectively, are shown in Fig. 4.3a for the Ti shot; they converged after about 6 iterations. Figure 4.3b shows the channel data (squares) for the this shot and fitted values (+). The red dots show the predicted signal contribution to channels 3 through 6 from the hot spectral component only. We estimated that the cold component contributes about 15% of the signal at channel 5, and more than 50% of the signal at channels 3 and 4. Conversely, the blue triangles representing the predicted cold contribution are much lower than the recorded signals at channels 5 and above, demonstrating the presence of harder x-rays.

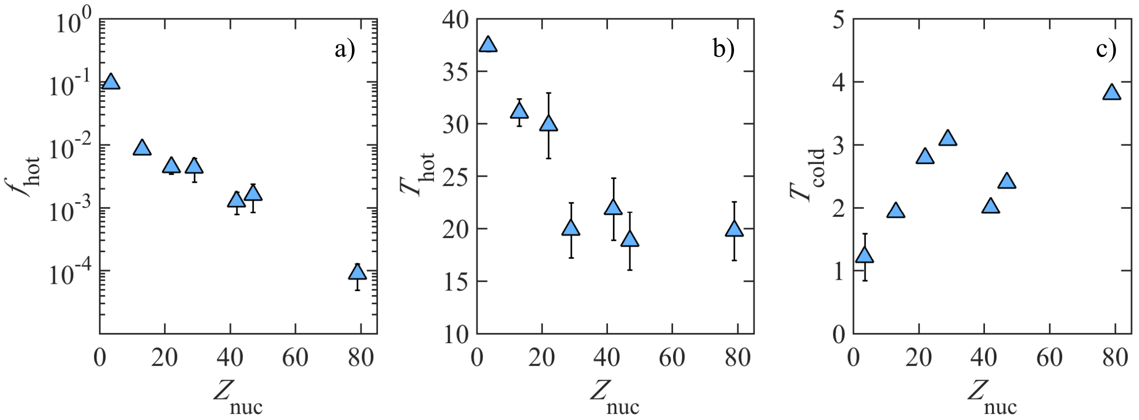

Figure 4.4: Estimates of a) hot electron fraction, f_{hot} and b) hot electron temperature, T_{hot} and c) effective temperature of the thermal emission, T_{cold} vs target atomic number, Z_{nuc} from fits to HXIP measurements. The error bars on T_{cold} are smaller than the data points in most cases.

4.2.2 Estimates of hot electron parameters

Figures 4.4a and b show the inferred values of f_{hot} and temperature, T_{hot}, vs. the target material atomic number, Z_{nuc}. The error bars are from error propagation through the fit, due to uncertainties in the channel signals; they increase with Z_{nuc} as signal-to-noise decreases. Disagreements with estimates of f_{hot} from measurements taken with a cannon spectrometer [106], as well as uncertainties in image plate calibration led to absolute errors of a factor of ~ 2. Regardless, f_{hot} decreased by a much larger factor of 10^3 across Z_{nuc}, which we attribute to the mitigation of LPIs and is consistent with the hypothesized physical mechanisms described at the beginning of this chapter. The hot-electron temperature decreased with Z_{nuc} as well, but flattened out around 20 keV, appreciably above the inferred values of T_{cold}, which are shown in Fig. 4.4c.

We observed that T_{cold} generally increased with Z_{nuc} up to Cu. We expect T_{cold} to correlate with the time- and space-averaged plasma temperature, $\langle T_e \rangle$ and can infer therefore, that $\langle T_e \rangle$ increased over this same range of Z_{nuc}. This is consistent with more efficient laser absorption, as well as less efficient electron thermal conduction into the dense target from increased collisions near n_c at higher Z. The lower T_{cold} at Mo (40) and Ag (47) is consistent with increased radiative losses expected at higher Z that start to significantly regulate the plasma temperature. However the higher value of T_{cold} at Au (79) does not support this interpretation, and may be evidence that line emission from highly-ionized states of Au not included in the model weighted this effective thermal spectrum towards higher energies. The high T_{cold} at Au may be evidence of inhibited electron transport near the critical density surface from ion-acoustic turbulence (IAT) driven by the return current instability (i.e. two-stream instability) [107, 108]. The return current instability may develop in the presence of steep temperature gradients and negligible IAW Landau damping, which are expected in high-Z laser-produced plasmas with $\langle Z\rangle T_e/T_i \gg 1$.

4.3 Angular Filter Refractometry to measure electron density profiles

Angular Filter Refractometry (AFR) imaging was used to measure electron density profiles and length-scales, which are relevant to the LPI thresholds and convective gains. The plasmas were imaged at 1.5 ns, based on past radiation hydrodynamic simulations showing that length-scales near $n_c/4$ start to stagnate around this time in CH targets [94]. The AFR diagnostic is covered in detail in [3] and [109], and in principle produces an iso-contour map of the total refraction angle, θ_{ref} that a probe beam accumulates through a plasma. A simplified diagram of the optical setup is shown in Fig. 4.5. A 4ω ($\lambda_{4\omega}$ = 263 nm) probe beam with 3.5-mm diameter, propagating in the z direction refracts in the $\alpha = x, y$ directions by angle,

$$\theta_\alpha = \frac{1}{2n_{c,4\omega}} \frac{d}{d\alpha} \int_{-L}^{0} n_e(x, y, z) dz, \tag{4.11}$$

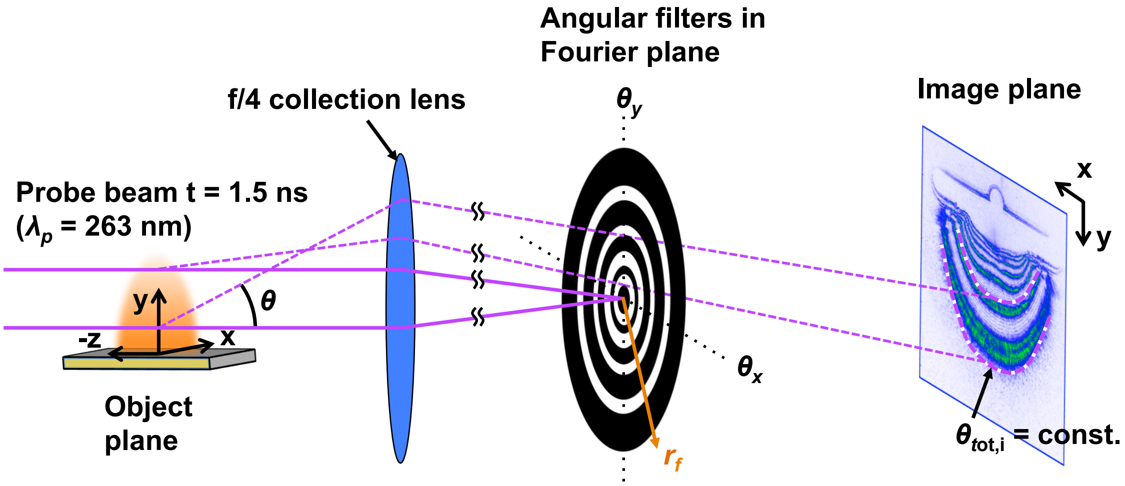

Figure 4.5: Simplified optical diagram of the AFR diagnostic. A 263-nm probe beam refracts through the plasma expanding from the target and is focused to the Fourier plane by an f/4 collection lens. Concentric angular filters in the Fourier plane block regions of the probe beam corresponding to specific bands of refraction angle. An image is formed with bands, along which the total refraction angle, θ_{ref} is constant. Adapted from Haberberger et al. [3].

over the extent of the plasma, L, where $n_{c,4\omega} = 1.59 \times 10^{22}$ cm^{-3} is the probe beam's critical density. Here, we have used the paraxial approximation, assuming that the displacements in the x and y directions over the plasma's extent are negligible. As the beam continues to propagate out to a distance z', the displacements, Δx and Δy, that a refracted ray accumulates in the x and y directions, respectively, are given by

$$\Delta x = z' \sin\theta_x \approx z'\theta_x \tag{4.12}$$

$$\Delta y = z' \sin\theta_y \approx z'\theta_y, \tag{4.13}$$

using the small angle approximation ($\theta_\alpha \lesssim 20°$). The total displacement of a ray in the $x - y$ plane is $\sqrt{\Delta x^2 + \Delta y^2} = z' \sin\theta_{\text{ref}} \approx z'\theta_{\text{ref}}$, from which we find that the total refraction angle is,

$$\begin{aligned}\theta_{\text{ref}} &\approx \sqrt{\theta_x^2 + \theta_y^2} \\ &= \frac{1}{2n_{c,4\omega}} \left| \nabla_{x,y} \int_{-L}^{0} n_e(x,y,z)dz \right| .\end{aligned} \tag{4.14}$$

After exiting the plasma, the refracted beam was collected at $f/4$, which limited the maximum detectable refraction angle to 7.13°. The beam then passed through additional optics and eventually was focused with a convex lens to the lens' focal or "Fourier" plane. In effect, the convex lens Fourier-transforms the refracted beam into (θ_x, θ_y) space [110]. Refracted light intersects the plane at a position $\mathbf{r}_f \propto \theta_x \hat{\mathbf{x}} + \theta_y \hat{\mathbf{y}}$ with origin at the optical axis, (i.e. $r_f = |\mathbf{r}_f| \propto \theta_{\text{ref}}$). A system calibration measured $\theta_{\text{ref}} = (0.368 \pm 0.003) \times r_f$. Un-refracted light intersects the optical axis at this plane and was blocked with a central Schlieren-like stop. Blocking beam propagation in other regions of the Fourier plane effectively filters out regions in (θ_x, θ_y)-space. The resulting reformed image has null regions where the original beam refracted at angles corresponding to these blocked regions of (θ_x, θ_y)-space. In this experiment, concentric opaque rings in the Fourier plane created a series of angular bandpass filters of total refraction angle, and hence, contours in the reformed image that corresponded to constant values of θ_{ref}. For example, two of these contours have been outlined with the purple dashed lines in the AFR image at the right in Fig. 4.5. The AFR images analyzed in this thesis were produced using the "AF3" filter whose angles below the cutoff are listed in Table 4.3. The full dataset is provided in Appendix A.

The image was recorded at a magnification of 4.1 on a CCD with 2048×2048 pixels of width 13.5 μm, resulting in a detector resolution of 3.3 μm at the target plane. The total resolution of the imaging system was measured to be 3.6 μm [109]. Temporal resolution was limited by the 10 ps width of the probe beam. After the beam was collected by the

$f/4$ collection lens, a filter strongly attenuated wavelengths outside the band 263 ± 2 nm to minimize background from plasma self-emission.

4.3.1 Reconstructing Plasma Density Profiles

To estimate length-scales at specific density, we need to reconstruct the full electron density profile. The plasmas produced in these experiments were approximately axisymmetric, driven by the near-circular focal spot and overlapping intensity profile above the target. In principle, an Abel inversion procedure could be used to recover a density profile, $n_e(r = \sqrt{x^2 + z^2}, y)$ upon acquiring a phase profile, $\phi(x, y)$ from the refraction contours, integrating the relation $\nabla\phi = \frac{2\pi}{\lambda_{4\omega}}(\theta_x \hat{\mathbf{x}} + \theta_y \hat{\mathbf{y}})$ (Eq. 2.20) as is done in [3]. However, the latter requires interpolating refraction between contours and presumes an (x, y) path of integration, since θ_x and θ_y were not measured individually. In this analysis, we instead sought to model the refraction images using a forward fit with a parameterized density profile, $\tilde{n}_e(x, y, z; \mathbf{p})$, whose shape is described by the vector of parameters, $\mathbf{p}$. The approximate refraction profile that results, $\tilde{\theta}(\mathbf{p})$ is simply that given by Eq. 4.14, replacing n_e with $\tilde{n}_e(\mathbf{p})$. An exhaustive fitting approach would be to calculate a full refraction image by modeling propagation of the 4ω beam through $\tilde{n}_e$, and then compare to the data, pixel-by-pixel, for many iterations of $\mathbf{p}$ until a stopping criterion is reached. In this analysis, we instead reduced the recorded refraction images to simply the positions of each contour of constant θ_{ref}. We then fit the reduced data by evaluating the model refraction angle profile, $\tilde{\theta}(x, y; n_e(\mathbf{p}))$, along the positions of the data contours, $\{(\mathbf{x}_i, \mathbf{y}_i), i = 1, ..., N_c\}$, which we then compared to the contours' corresponding true refraction angles, $\theta_{\text{ref},i}$. Figure 4.6 provides a visual representation of this procedure. The vector of fit parameters that best fit the data, $\hat{\mathbf{p}}$ was then found by minimizing the sum of square differences between

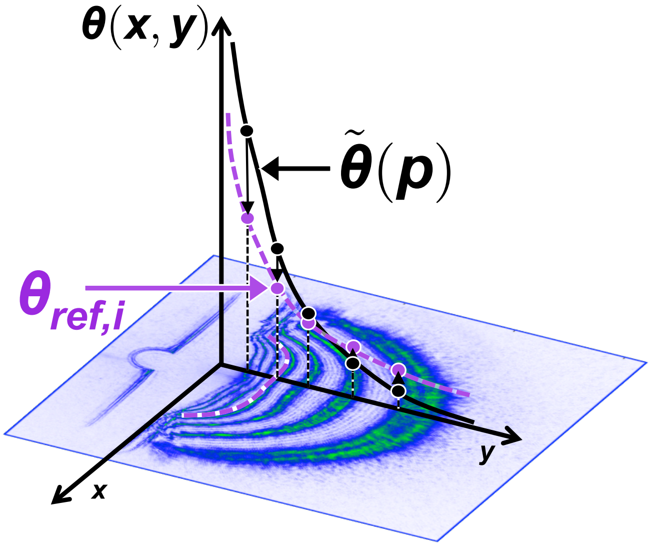

Figure 4.6: Visual representation of refraction contour fitting procedure. Refraction angle, $\theta(x, y)$ is represented as a surface in the $x - y$ plane. The purple dots represent the total refraction, $\theta_{\text{ref},i}$ along the y-axis at the locations of the contours in the image. The model refraction profile, $\tilde{\theta}(\mathbf{p})$ is shown in black for a given set of fit parameters, $\mathbf{p}$, where the black dots are the model refraction at the positions of the contours on-axis. The parameters are varied to minimize the difference between the true refraction and model refraction along the contours (i.e. make the black dots lie as close to the purple dots as possible). Only the axis is shown for clarity, but this procedure is applied to the entire refraction contours in the $x - y$ plane.

Table 4.3: Angular Filter Refractometry “AF3” filter angles below the 7.13° cutoff

Angle	(degrees)
1	0.092
2	0.350
3	0.654
4	1.004
5	1.401
6	1.844
7	2.334
8	2.870
9	3.453
10	4.082
11	4.758
12	5.480
13	6.248
14	7.063

true and model refraction angle along the N_c contours, i.e. by solving

$$\hat{\mathbf{p}} = \underset{\mathbf{p}}{\operatorname{argmin}} \sum_{i=1}^{N_c} \left|\left| \frac{1}{\sigma_{\theta_i} N_i} \left(\theta_{\text{ref},i} \mathbb{1} - \tilde{\theta}(\mathbf{x}_i, \mathbf{y}_i; \tilde{n}_e(\mathbf{p})) \right) \right|\right|^2 . \tag{4.15}$$

Here, the contribution of the i^{th} contour was normalized by its number of coordinate positions, N_i and the error in nominal refraction angle, σ_{θ_i}, and the quantity $\mathbb{1}$ is the vector of ones of length N_i. Minimization was performed with a Levenberg-Marquardt steepest-descent algorithm, which could handle the nonlinearity of Eq. 4.15 that was introduced by Eq. 4.14 and the dependence of $\tilde{n}_e$ on $\mathbf{p}$. Once model parameters, $\hat{\mathbf{p}}$ were found, length-scales were calculated from the best-fit electron density profile.

4.3.2 Processing of AFR data

To track the absolute expansion, we needed to measure the position of the original target surface, which became obscured by refraction through steep gradients. Prior to driving the foil target, a calibration image was taken using the 4ω probe beam without the angular filters to record the position of the original target surface, as shown in Fig. 4.7a, relative to the fiducial sphere. Assuming the sphere moved a negligible amount over the length of the laser pulse, we used this relative distance to locate the original target surface at the time of measurement in the AFR image (Fig 4.7b).

After locating the original target surface, we extracted the contours nominally outlining the bands in the images. Ideally, in an AFR image the intensity would be equal to zero in the "blocked" refraction regions and equal to a constant value in all other regions. However, diffraction from the hard edges of the angular filters created an interference pattern in the blocked regions between the bands and tended to smear out their edges. We used a Gaussian filter to smooth out the interference pattern and thresholded the image at some fraction of the maximum intensity after subtracting background. Simulated refraction images were calculated with a Fourier method from density profiles predicted by radiation hydrodynamic simulations to determine this threshold. We found that a $\sim 30\%$ threshold produces contours that most closely overlap with the contours corresponding to the filters true refraction angles. Figure. 4.7c shows part of a refraction image after thresholding, where the resulting contours are outlined in red.

4.3.3 Modeling of density profiles

We sought a suitable model density profile to complete the forward-fitting procedure, whose shape we motivated with physical considerations of these expanding laser-produced plasmas. At early times, the majority of laser-absorption occurs close to the critical surface and a hot corona expands in the axial (target-normal) direction. The hot corona will be approximately isothermal because heat conduction occurs rapidly here, scaling as $T_e^{7/2}$. We can check this approximation using the criterion provided in [9] for the laser irradiance

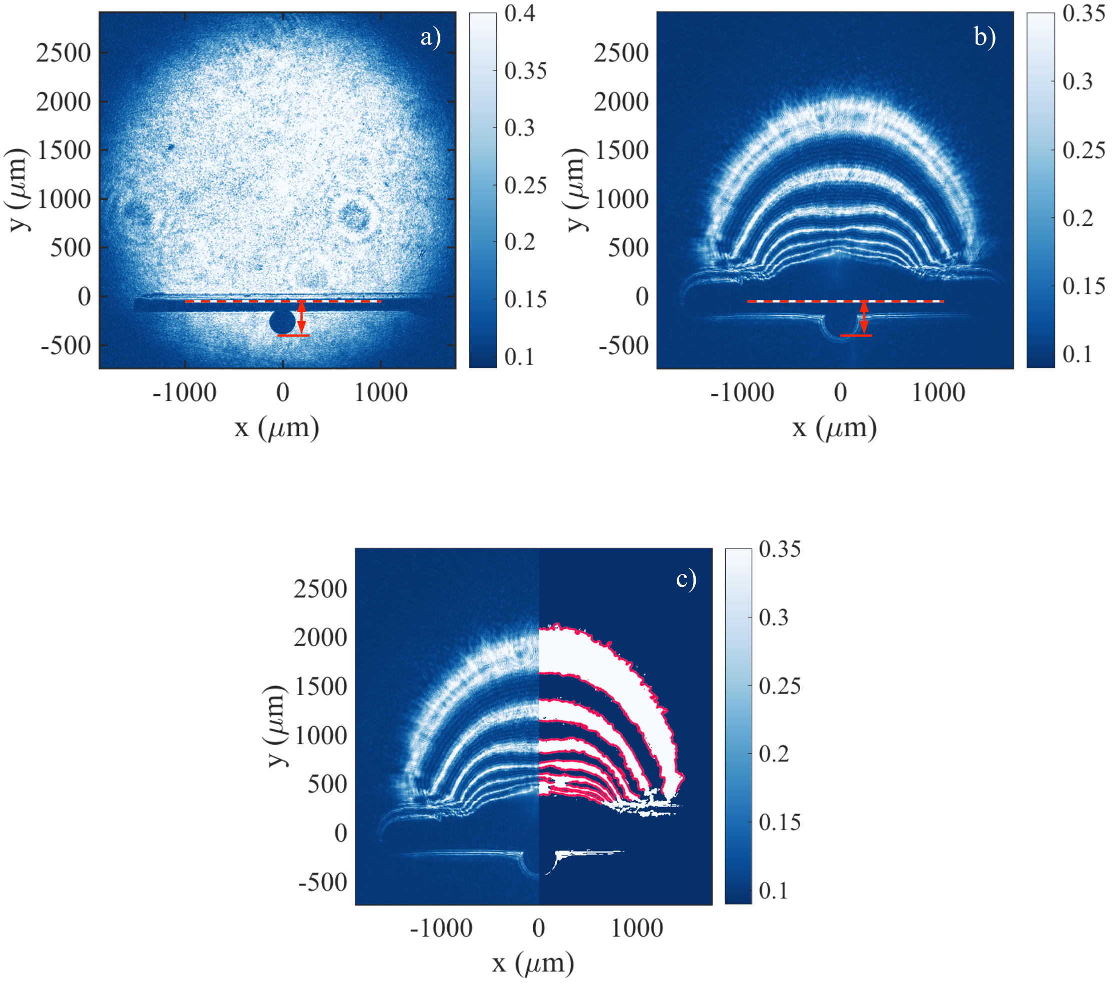

Figure 4.7: a) Image of undriven target with AFR probe beam without angular filters, showing the original target surface and fiducial sphere. b) AFR image of driven CH target with angular filters. c) Demonstration of contour extraction from thresholded image. Contours used in the fit for this image are shown in red.

absorbed in the corona,

$$I_{a,14} \geq 2.7 \times 10^{-2} Z_{\text{eff}} \ln \Lambda t_{\text{ns}} \lambda_{\mu}^{4} \frac{[\langle Z \rangle + 1]^{7/2}}{\langle Z \rangle^{2} A^{3/2}}, \tag{4.16}$$

in units of 10^{14} W/cm^2, where t_{ns} is the expansion time in ns, and λ_{μ} is the laser wavelength in microns. Even assuming full ionization, we found that I_a only needs to exceed $\sim 3\times10^{13}$ W/cm^2, or less than 3% of the incident irradiance through the end of the 2-ns laser pulse. Simulations presented in Ch. 5 also indicate isothermal behavior in the corona. Assuming an infinite amount of mass is available from the remaining solid target, the density profile of the planar isothermal rarefaction is found analytically to be a well-known exponential, $n_e \propto \exp(-y/c_s t)$. Here, $c_s = \sqrt{(\langle Z \rangle + 1) T_e / m_i}$ is the isothermal sound speed for ions of mass, m_i and temperature $T_i \approx T_e/3$, where T_e is in energy units.

For late times, the expansion size normal to the target grows to the order of approximately the laser spot radius, R_f and lateral flow beyond this distance becomes important. The lateral expansion is limited by the mass originating from within the focal spot, and may be described approximately as a mass-limited isothermal rarefaction. Past authors derived analytically a 1D self-similar density profile from the single-fluid Euler equations to describe this type of rarefaction [111–113]. In doing so, they defined a dimensionless similarity coordinate, $\xi = s/S(t)$, where $S(t)$ is a self-similar length-scale that increases in time and s is a general spatial coordinate, referring to linear distance from the origin in planar geometry (y) and radius in cylindrical or spherical geometry. For a free, homogeneous expansion, the velocity component in this direction, $u_s(s,t)$ is linear in s. The similarity ansatz for velocity and mass density becomes [111]

$$u(s,t) = \dot{S}\xi, \tag{4.17}$$

$$\rho(s,t) = \rho_0 \left(\frac{S_0}{S(t)} \right)^{\alpha} G(\xi), \tag{4.18}$$

where ρ_0 and S_0 are the initial central density and size of the expanding plasma and $\alpha = 1$, 2 or 3 for planar, cylindrical or spherical geometry, respectively, and $G(\xi)$ is the self-similar density distribution. The factor in parentheses on the RHS of Eq. 4.18 decreases in time and accounts for the mass-limited nature of the expansion. Inserting this ansatz into the fluid continuity and momentum equations, one finds

$$G(\xi) = \exp(-\xi^2). \tag{4.19}$$

We approximated the lateral shape of the low-density corona with this 1D Gaussian profile in cylindrical geometry, which agrees well with simulations presented in Ch. 5.

Because the isothermal plasma should freely expand away from the target in *all* directions, the density profile is separable in r and y, i.e. $\rho(r, y, t) = \rho_0 f(y, t) g(r, t)$. As the lateral flow limits the mass available to feed the axial expansion, we would expect at very late times and for $y > R_f$ that the axial expansion is also well-described by a mass-limited isothermal rarefaction (eventually, the expansion becomes spherical as the size of the plasma grows to be much larger than the laser spot). To allow for intermediate behavior between simple-planar and mass-limited on axis, we used the axial profile $f(y \gtrsim R_f) \propto \exp(-[(y - y_t)/L]^b)$, where $1 \le b \le 2$. Here, L is the characteristic axial length-scale and y_t is the center of the axial rarefaction. For the results in Sec. 4.3.4, we found typically $b \approx 1.3 - 1.5$. In this model of the isothermal corona, we assumed the ionization to be constant in space, which was a reasonable approximation since ionization only weakly depends on density. This led the electron density, $n_e(r, y)$ to have the same spatial dependence as $\rho(r, y)$.

Closer to the target surface, the flow remains predominantly axial. For late times and mid-to-high-Z, absorption of laser energy becomes distributed, rather than locally deposited near n_c. Regardless, it has been found using a distributed absorption model with flux-limited electron heat transport that the behavior near $n_c/4$ is approximately exponential-like [114].

From these physical considerations, we proposed a density profile for the forward model that combined an outer corona ("cor") with an inner absorbing ("abs") region:

$$\begin{aligned}\tilde{n}_e(r, y; \mathbf{p}) = & n_{\text{cor}} \exp\left[-(r/R_{\text{cor}})^2 - ((y - y_t)/L_{\text{cor}})^b\right] + \\ & n_{\text{abs}} \exp\left[-(r/R_{\text{abs}})^4 - y/L_{\text{abs}}\right] ,\end{aligned} \tag{4.20}$$

where a 4^{th}-order supergaussian for r was chosen to limit the extent of the inner profile's axial behavior to approximately the laser focal spot. Therefore, a total of eight fitting parameters, $\mathbf{p} = [n_{\text{cor}}, R_{\text{cor}}, L_{\text{cor}}, b, y_t, n_{\text{abs}}, R_{\text{abs}}, L_{\text{abs}}]$, were used to characterize the profile at $t = 1.5$ ns. This semi-analytical model proved robust enough to accommodate the variation in scale of the corona and absorbing regions across materials.

4.3.4 Estimates of electron density profiles and length-scales

Figures 4.8a and 4.8c show halves of the filtered refraction images of the irradiated CH and Au targets, respectively, at 1.5 ns where the lasers are incident 23° from the $+z$ direction. The measured contours in the Au plasma are significantly closer to the original target surface than in the CH plasma, indicating slower expansion and shorter length-scales. The overlaid dashed lines represent the refraction contours from the fit evaluated at the nominal angles of the measured contours, which show reasonable agreement with the data. The fit does not model the behavior of the profile outside the focal spot below about 250 μm from the target surface where we see significant disagreement. Figures 4.8b and 4.8d are the corresponding best-fit electron density profiles (divided by the the critical density of the drive beams). The solid and dotted contours in these profiles are located at $n_c/4$ and $n_c/10$, respectively. We observed that refraction was too great to image the plasma above $\sim n_c/10$ with this diagnostic, so any estimate of L_n beyond $n_c/10$ is an extrapolation.

The best-fit density profiles on axis are plotted for several materials in Fig. 4.9a, where the bands represent the one-sigma error, which increases going to lower densities. The dotted lines are the fit extrapolated outside of where the refraction data exists. The inferred distance from the data cutoff to $n_c/4$ varies from 150 to 200 microns based on these extrapolations. We clearly see that slower expansion (i.e. evidence of lower sound speeds) going to higher Z by noting that below $\sim n_c/5$ the position of a given density is closer to the target surface. The profiles from the Al and Mo targets are consistent with this trend, although they are not shown for clarity. The lower density cutoff is about the same for all materials, around $0.15n_c$.

Estimates of L_n from the fit density profiles on-axis are plotted in Fig. 4.9b, vs. n_e/n_c for several of the target materials in this experiment, separated by color. The bands again represent the one-sigma confidence interval around the mean value. Across materials, we observe a clear steepening of L_n as Z_{nuc} increases for densities $\sim n_c/30 - n_c/10$. The length-scales appear to have a maximum, marking where the profile transitions from the absorbing region to corona in our model. Estimated length-scales are plotted vs. Z_{nuc} in Fig. 4.10 at densities $n_c/50$, $n_c/10$ and $n_c/4$. At $n_c/10$ length-scales decrease approximately linearly with Z_{nuc}, by a factor of 2 from CH to Au. Similar behavior is observed at $n_c/4$ according to the inferred values of L_n extrapolated from the fits. The nature of the steepening is explored with simulations in Ch. 5 and is likely from increased radiative losses at densities near and above $n_c/4$ as Z_{nuc} increases, leading to slower ablation. At constant electron temperature and laser intensity, such prominent steepening we would expect to substantially reduce growth of EPWs from laser-plasma instabilities across materials. A factor of 2 shorter length-scales would result in a factor of 2 decrease in convective gains and a factor of 2 and 2.5 increase in absolute thresholds for TPD and SRS,

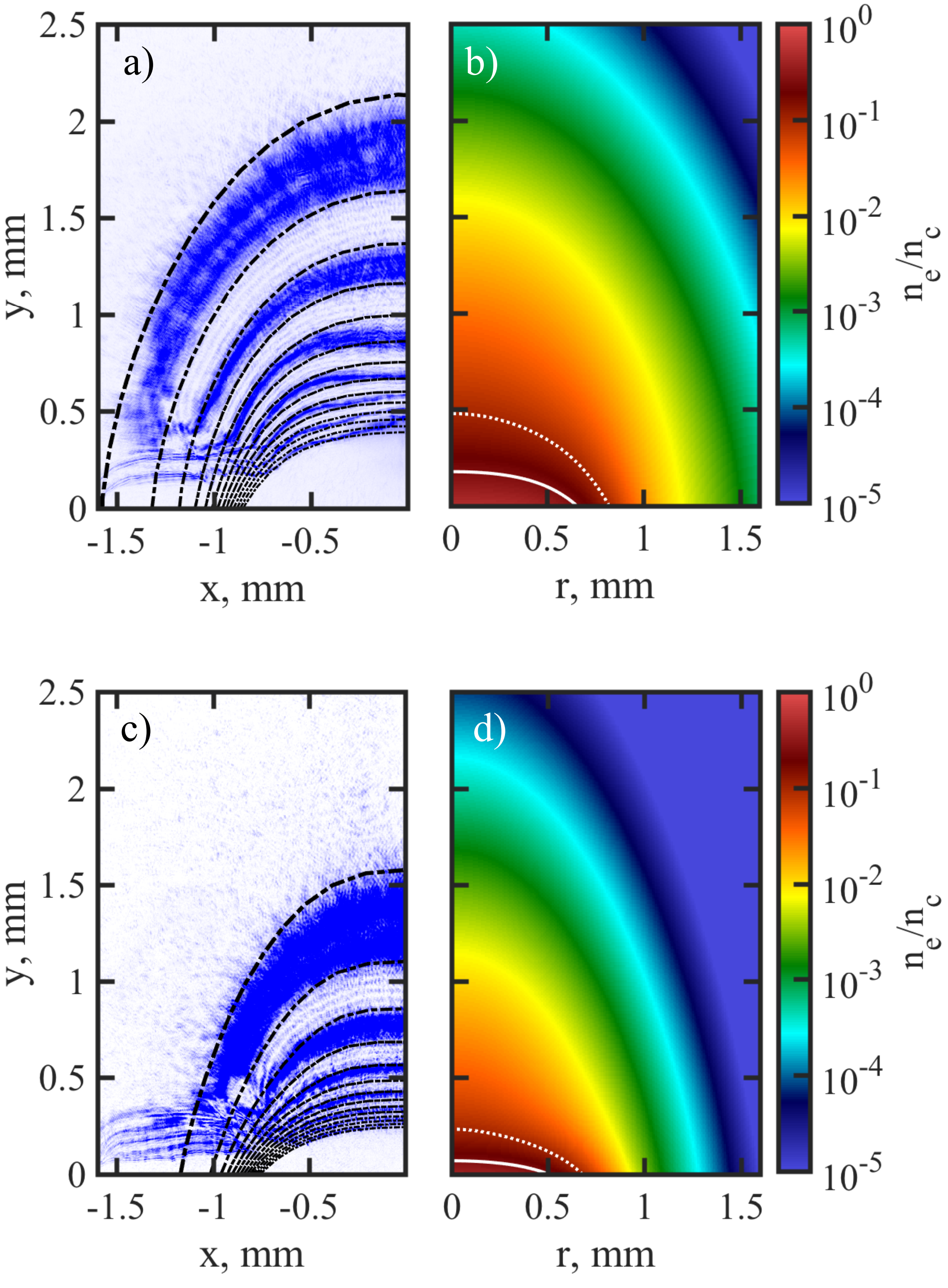

Figure 4.8: a) Comparison between the AFR data and resulting refraction contours (dashed lines) from the fit for the CH plasma. b) The corresponding electron density profile with density contours at $n_c/4$ (solid line) and $n_c/10$ (dotted line). The corresponding plots for the Au plasma are shown in c) and d).

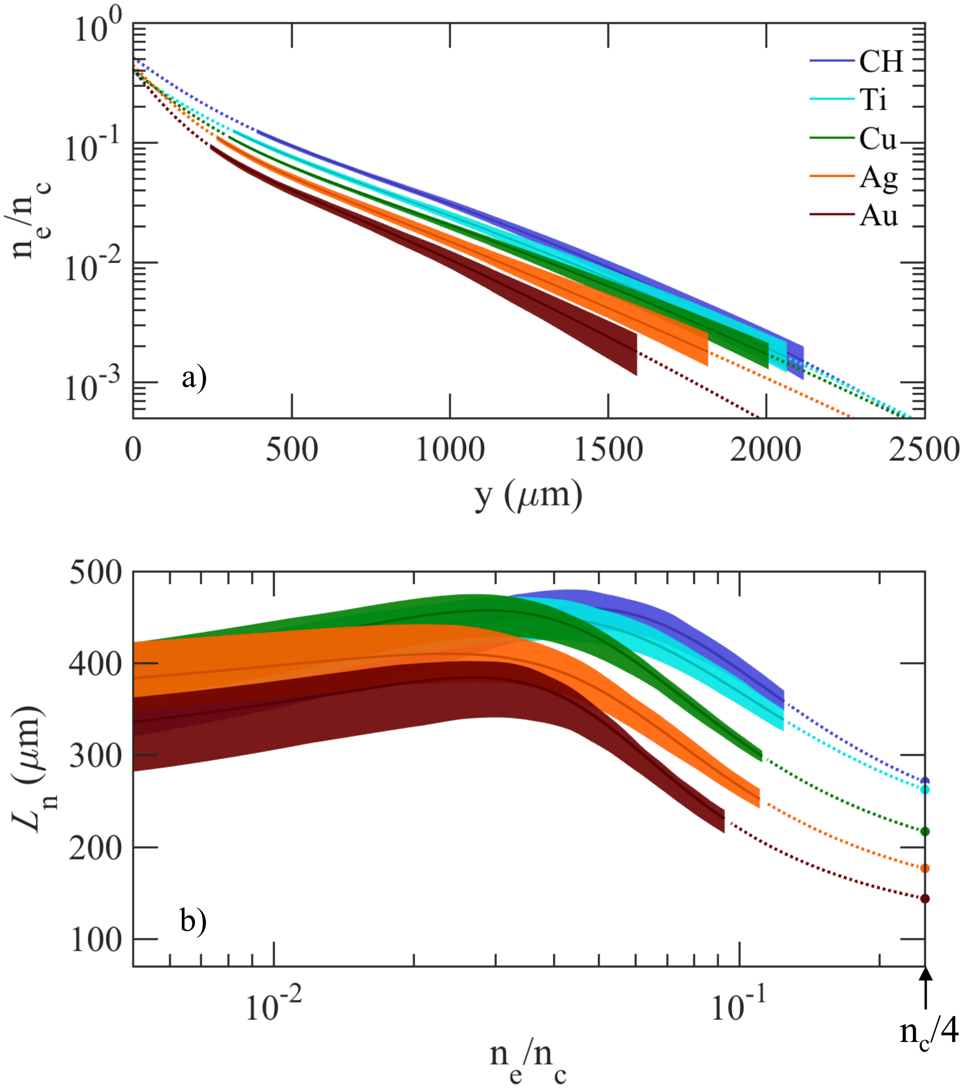

Figure 4.9: a) Best-fit electron density profiles on-axis ($r = 0$) vs. position from original target surface for several materials. Bands represent the one-sigma confidence interval and dotted lines are the fit extrapolated beyond the region where data was present. b) Estimates of electron density gradient length-scale on-axis vs. n_c/n_c from the profiles in (a). Again, the bands represent one-sigma confidence intervals and dotted lines are the fits extrapolated outside the data region.

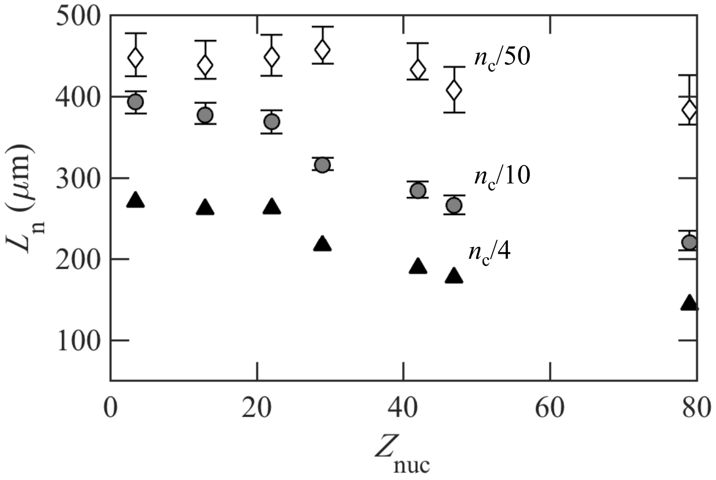

Figure 4.10: Estimates of L_n from fits to data on-axis vs. Z_{nuc}, where open diamonds, gray circles and black triangles are at $n_c/50$, $n_c/10$ and $n_c/4$, respectively.

respectively.

At densities less than $n_c/30$, occurring at axial distances larger than the laser spot radius, length-scales begin to depend much less strongly on Z_{nuc}, and the Z-dependence disappears almost entirely by $n_c/50$, shown as the open diamonds in Fig. 4.10. This result suggests that out in the low-density corona, the profile is becoming more regulated by lateral expansion beyond the laser spot and less by material-dependent processes.

In the corona where the plasma is freely expanding, the electron density profile is determined only by the geometry of the rarefaction and the isothermal sound speed–and hence, the electron temperature. A rough estimate is to approximate $L_n \approx c_s t$; this is an exact relationship in the planar, infinite-mass limit of the isothermal rarefaction. In the limit where the rarefaction becomes mass-limited, we have a different relationship between the density profile and sound-speed [111]:

$$c_s t = \frac{S_0}{2} \int_0^{S/S_0} (\ln \mu)^{-1/2} \, d\mu. \tag{4.21}$$

We use both of these relationships to estimate rough limits on the plasma temperature

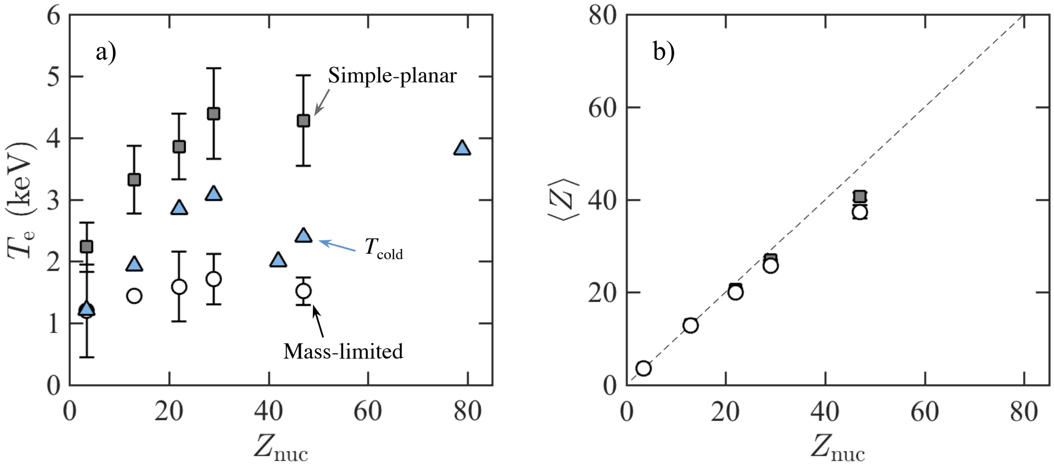

Figure 4.11: a) Estimates of coronal electron temperature using measured length-scales, calculated from relationships between sound speed and density profile from simple-planar and mass-limited models, compared to estimates of T_{cold} from HXIP measurements. b) Corresponding estimates of average ionization.

in the corona, which LPI thresholds and growth depend on in this region in addition to length-scales. The expansion time we take to start from the 50% rise time of laser pulse, giving 1.38 ns at the time of measurement. Ionization is acquired using PrismSPECT [115] non-LTE ionization tables for materials CH through Cu and Ag. These tables were not available for Mo and Au. For Eq. 4.21, we take the initial width of the plasma to be the spot radius, $S_0 \sim R_f$ and use the radial self-similar length-scale ($S \to R_{\mathrm{cor}}$) acquired from the fits. The estimates of coronal temperature and average ionization are shown in Figs. 4.11a-b, respectively, where the gray squares and open circles are from calculations using the simple-planar and mass-limited limits, respectively. We see that in both cases, the temperature rises with Z_{nuc} and appears to either plateau or decrease after Cu, much like the behavior of T_{cold} (shown again as blue triangles) estimated from fits to hard x-ray measurements in Sec. 4.2.2. However, the more than factor of 2 difference on-average in T_e between the separate limits demonstrates the simple models' inadequacy in describing the detailed behavior of the expanding plasmas in these experiments.

4.4 Conclusions

Experiments were performed to measure hot electron production from laser irradiated foils of low- to high-Z material. The fraction of laser energy converted to hot electrons, inferred from hard x-ray measurements, decreased by 3 orders of magnitude from CH to Au, consistent with the mitigation of laser-plasma instabilities going to higher Z. Hot electron temperatures were observed to decrease from 40 to $\sim$20 keV across materials, bottoming out around Ti. A refraction imaging technique was used to measure electron density profiles and estimate gradient length-scales. Across materials, the length-scale at $n_c/10$ was observed to decrease by nearly a factor of 2, from 400 μm at CH to $\sim$200 μm at Au. Extrapolations predicted a similar trend at $n_c/4$. The steepening length-scales are consistent with reduced hot-electron production going to higher Z, from higher thresholds and less growth of laser-plasma instabilities.

CHAPTER 5

Radiation Hydrodynamic Simulations

In this chapter, we present results from radiation hydrodynamic simulations that model behavior of the laser-plasmas produced in the experiments reported on in Ch. 4. This is in an effort to predict plasma conditions and how their variation across materials would have affected growth of LPIs and hot-electron production. Plasma conditions such as electron temperature and ionization that we did not measure are necessary to determine thresholds from inhomogeneity in the case of TPD and from the effect of damping for all LPIs relevant to hot-electron production. Here we primarily compare the simulations to the measurements of electron density profiles from refraction imaging, while additional results are presented in Ch. 6. Nominal agreement between the predicted and measured density profiles offers some validation in using simulation results to infer properties of hot-electron production.

In general, measurements of electron density profiles from laser-produced plasmas are useful to the broader HEDP community as a means to validate radiation hydrodynamics codes. The electron density and temperature profiles in the underdense plasma directly determine propagation and absorption of laser energy, and hence the coupling of laser energy to the dense target. These profiles are strongly affected by electron heat conduction near the critical density as well as by emission and absorption of radiation. Therefore, electron density profiles can be a useful diagnostic to probe physical models used in radiation hydrodynamics codes that describe these processes.

5.1 CRASH Simulations

Simulations were performed in 2D ry geometry for target materials CH, Al, Ti, Cu and Ag using the Eulerian radiation-hydrodynamic code, CRASH [116], with initial conditions mimicking those of the experiments. We use the y axis for azimuthal symmetry here (rather than the z axis) to be consistent with the target coordinate system used in Ch. 4. Laser energy was deposited in the plasmas by ray-tracing the experimental beam geometry in 3D after projecting the azimuthally-symmetric profiles around the target axis. The 3D profile of laser-energy deposition was then azimuthally-averaged for further hydrodynamic calculations. This procedure avoided the excess heating that would occur on-axis using 2D ray-tracing as a result of infinite ray densities on-axis. Electron heat conduction was modeled using flux-limited electron heat transport, where the flux-limiter, $f = 0.06$ is the fraction of the free-streaming electron heat flux. Radiation transport was calculated using multi-group diffusion with equation of state and absorption and emission opacity tables from PrismSPECT [115]. Tables for Ag were not available, so the corresponding tables for Sn were used instead. We assumed this was a reasonable approximation since Ag and Sn only vary in atomic number by 3; however, the substitution may have led to excess ionization and hence, laser absorption at low densities. Non-local thermodynamic equilibrium (non-LTE) effects were expected to be important in these plasmas, where sharp density and temperature gradients were present and in the low-density, optically thin corona. A preliminary approach to incorporate non-LTE physics was used in which CRASH switched between LTE and non-LTE opacity and equation-of-state tables along a predefined boundary in ion number density (n_i) and electron temperature space. Non-LTE tables were used when $n_i < 10^{22}$ cm^{-3} and $T_e > 100$ eV.

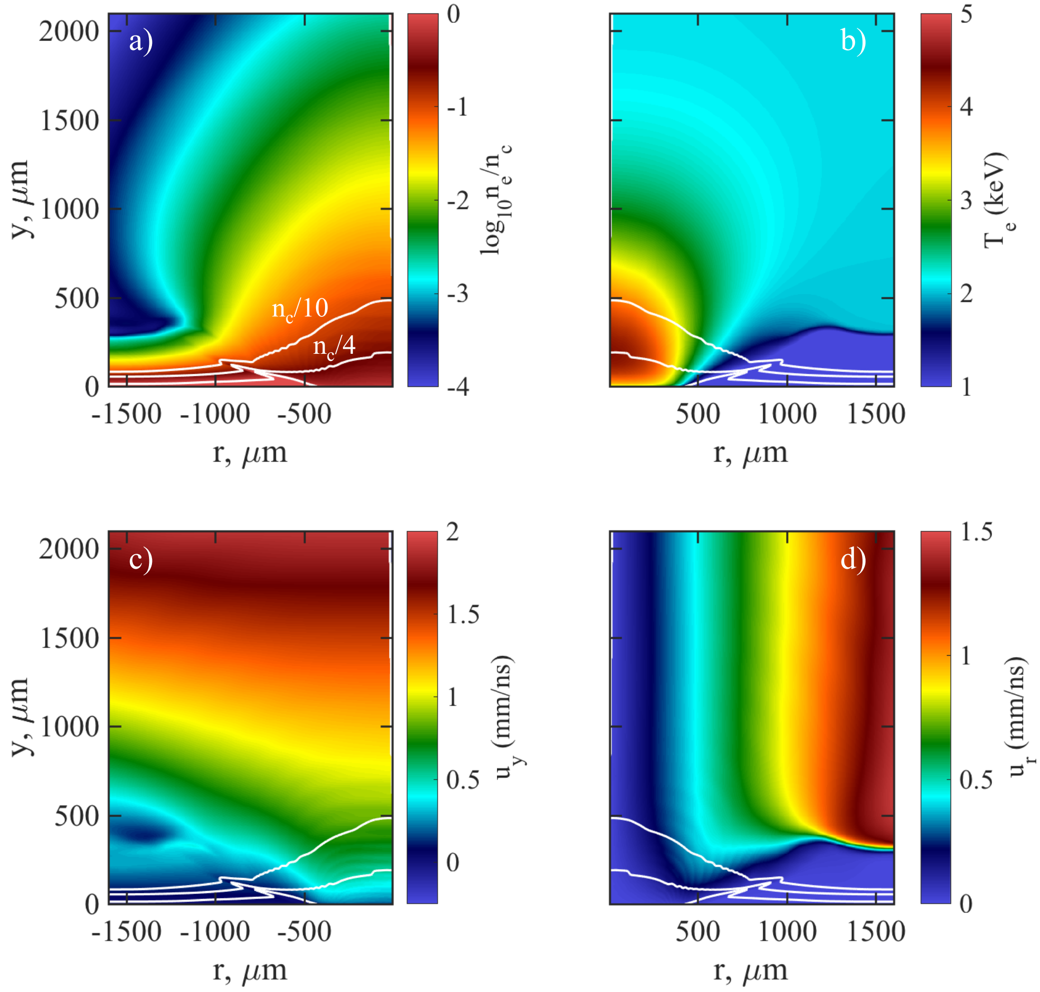

Figure 5.1: Spatial profiles at 1.5 ns predicted by CRASH simulation of an irradiated Ti target. a) Electron density, b) electron temperature, c) axial velocity, d) radial velocity.

Profiles from the simulation of the Ti target at 1.5 ns into the laser pulse are shown in Fig. 5.1a-d, where lasers are incident 23° from the y-axis. The white contours represent the locations of the $n_c/10$ and $n_c/4$ surfaces in each profile. In the temperature profile, we observe a hot "bubble"-like feature near the original target surface with a peak temperature of 4.3 keV that is a factor of 2 higher than the asymptotic temperature in the corona. This feature coincides with the region of highest overlap between individual laser beams. The drop-off to lower temperatures outside this region does not occur in 1D planar simulations and is caused in part by cooling from lateral expansion and heat conduction.

The plasma starts to become isothermal at densities of $\sim 0.02n_c$, except close to the target, outside the laser spot. In this isothermal region, both the axial velocity, u_y and radial velocity, u_r are approximately spatially-linear in their respective directions, away from the target surface. These behaviors are consistent with the assumption of a freely-expanding isothermal corona that we used to guide our choice of model density profile to fit the refraction measurements in Sec. 4.3.3. In addition, the mass flux ($\rho\mathbf{u}$) in the focal spot is directed almost entirely along the axis between densities n_c to $\sim n_c/20$, which is consistent with the presumed spot-limited planar behavior near the target surface in the model density profile. Similar behaviors are observed across the materials simulated.

5.1.1 Comparison to Measurements

The 2D electron density profiles predicted by CRASH simulations are compared to the best-fit density profiles from refraction measurements in Figs. 5.2a-d for the CH and Ag targets. The simulated and measured profiles agree generally in shape for both targets shown. Expected large discrepancies occur well outside the focal spot and close to the target surface, where the lasers do not directly heat the expanding plasma. At 1.5 ns, both the simulations and measurements show that more expansion has occurred on-axis than

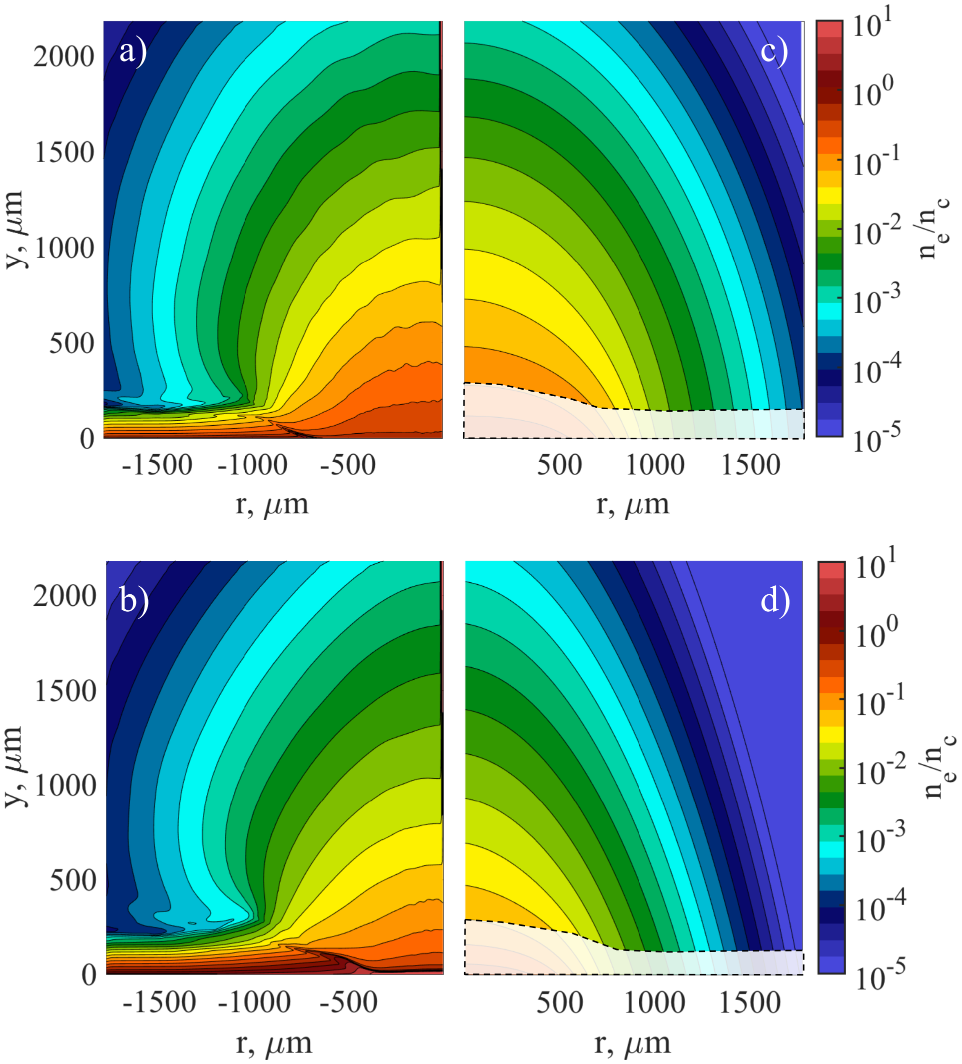

Figure 5.2: 2D Electron density profiles at 1.5 ns, predicted by CRASH simulations for a) CH and b) Ag targets. Plots c) and d) are the corresponding density profiles from fits to refraction measurements.

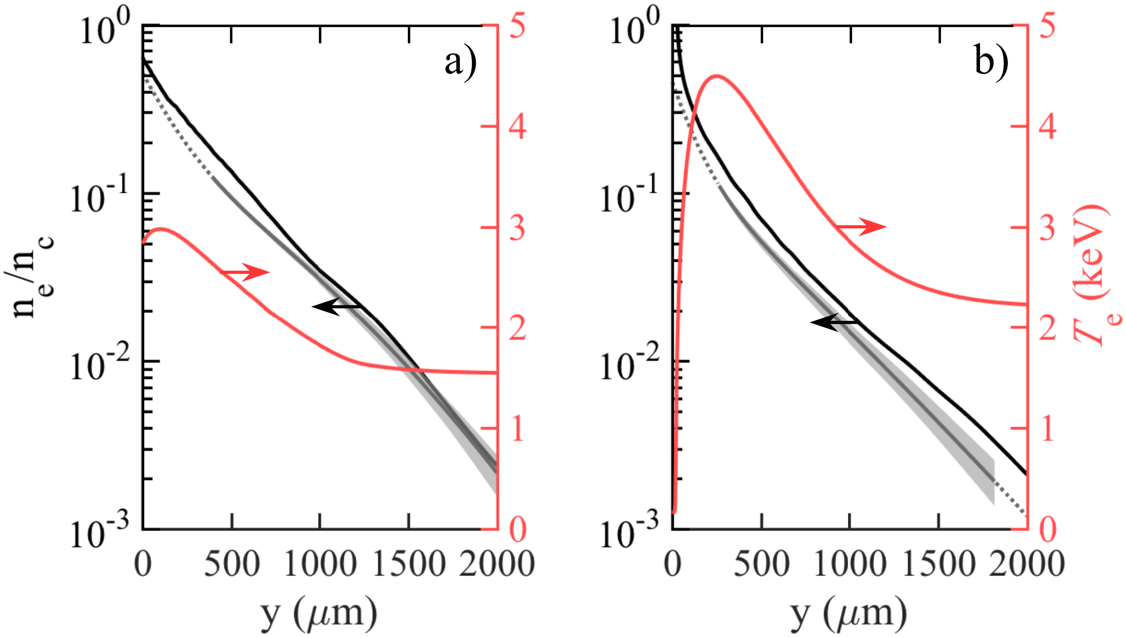

Figure 5.3: Spatial profiles at 1.5 ns from CRASH simulations at a target radius of 50μm for a) CH and b) Ag targets. The electron density profile from the simulation is depicted as the black solid line and that from the fit to the data at the same position is shown as the solid gray line with one-sigma error band, all with relation to the left vertical axis. Dotted lines are the fit extrapolated outside the range of data. The electron temperature profile is shown by the solid red line, with relation to the right vertical axis.

in the lateral direction.

Figure 5.3, provides a comparison on-axis between measured (solid gray line) and simulated (solid black line) electron density profiles for a) CH and b) Ag. Along the axis, where length-scales are longest, the simulations agree to within 10-40% of the measurements from $n_c/100 - n_c/10$ and 20-40% from $n_c/10 - n_c/4$ across all materials modeled. Throughout the profiles, the simulations over-predict densities at a given position, which has similarly been observed by other authors in the past [3,117,118]. In the case of Ag, the predicted profile becomes very steep at densities greater than $\sim 0.3 n_c$, and departs drastically from the extrapolation of the fit. Length-scales on-axis generally agree with those from the fits to measurements, shown in Fig. 5.4 in red and blue, respectively at densities $n_c/50$ (diamonds), $n_c/10$ (circles) and $n_c/4$ (triangles). The decreasing trend with Z_{nuc} is reproduced by the simulations, and persists at lower densities than what is extrapolated from the measurements. Excellent agreement is seen at $n_c/4$ for all materials except CH, despite the lack of data at this density.

Consistent overestimation of densities at a given position and length-scales at low density relative to measured values may result in part from the absence of a nonlocal electron transport model in our simulations. Nonlocal electron transport becomes significant at laser intensities near and above 10^{15} W/cm^2 [119, 120]. The hotter plasmas at these intensities contain a significant population of electrons with energies in excess of 10 to 15 keV, whose mean free paths can be many times larger than the temperature gradient length-scale near critical density. Penetration and energy deposition of these electrons into the high-density region of the target can increase both temperature and density length-scales and ablation velocity. Hu et al. [121] showed that at high intensity, inclusion of a nonlocal transport model in 2D DRACO simulations accurately captured experimental trajectories of driven foils, compared to a constant flux limiter model with $f = 0.06$. The nonlocal model provided an effective time-dependent flux limiter that averaged 0.08 over the first 0.5 ns of the pulse and 0.06 over the next 0.5 ns. With regard to the CRASH simulations presented here, a less-inhibited heat flux at early times would lead to a cooler corona, and hence lower late-time densities at a given position from slower expansion velocities.

In contrast to the other targets simulated, the predicted density profile for the CH target most closely matches the measured profile out in the corona and shows the largest disagreement at higher densities, between $n_c/20 - n_c/10$. Part of this disagreement may result due to the loss of laser energy at the higher densities to hot-electron production, which we inferred was $\sim 10\%$ from hard x-ray measurements. Scattered light from SRS and SBS would cause additional energy losses. Another possibility is that in the multi-species CH plasma, the hydrogen ions' would have higher sound speeds than the carbon

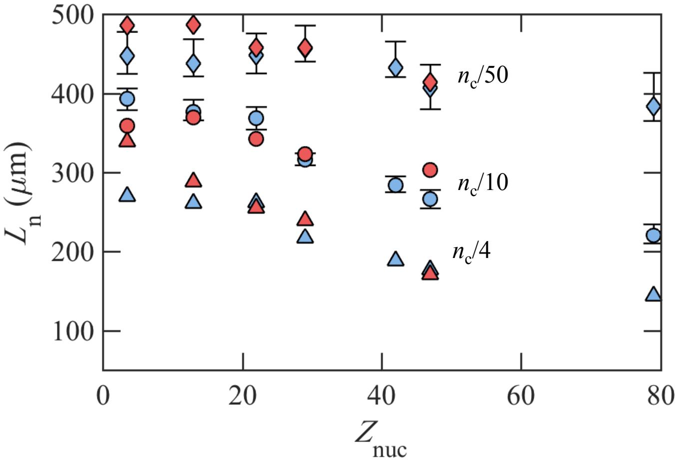

Figure 5.4: Electron density gradient length scales for the different target materials at $n_c/50$, $n_c/10$ and $n_c/4$ from simulations (red) and fits to refraction data (blue) at 1.5 ns.

ions due to a larger charge-to-mass ratio. As a result, the corona would expand more rapidly and the higher density region more slowly than if the plasma were composed of a single-ion species with average mass and charge given by an atomic mixture of hydrogen and carbon; the latter is the approximation used in the simulation. Other mechanisms may explain this relationship between the simulation and measurement, however, and the study of this topic falls outside the scope of this thesis.

In addition to the lack of non-local electron transport modeling mentioned above, inaccuracies in the high-Z emission and absorption opacities may also significantly influence the simulation results. For example, underestimation of dielectronic recombination could lead to an overestimation of $\langle Z \rangle$ and as well, temperature, as a consequence of fewer radiative losses.

5.2 Evaluation of profile steepening

We take a moment to gain some insight into the physical causes of profile steepening observed as Z_{nuc} increased. The electron density and temperature profiles at a radius of 50 μm are shown in Fig. 5.5 for each material simulated, down to a density of $n_c/20$. We

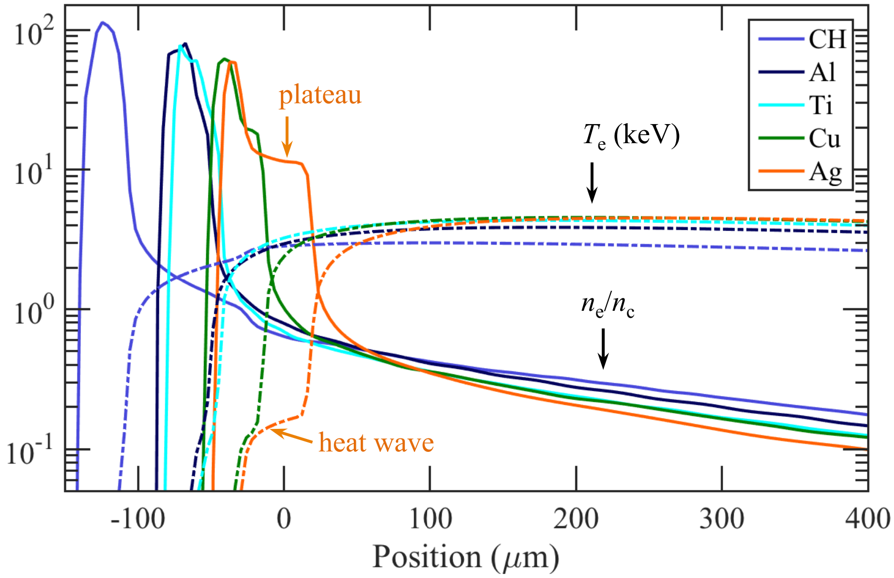

Figure 5.5: Electron density (solid) and temperature (dashed) profiles on axis from 2D CRASH simulations for each material, separated by color.

observe several general trends going from CH to Ag. First, the distance that the shock has traveled from the original target surface decreases. Second, the temperature in the low-density plasma increases, but appears to level out between Cu and Ag. Third, the length of the conduction zone, from $\sim 2n_c$ to where the temperature starts to plateau decreases, i.e. the profiles in this region steepen. In general, these features are consistent with more inhibited electron heat conduction going to higher Z as the plasma becomes more collisional from ions with higher charge states. However, the steepening may also result from effects of radiation.

By Cu we observe two distinct ablation fronts in the density profile, separated by a density plateau as well as a foot in the temperature profile ahead of the conduction zone that corresponds to a radiative heat wave. This "double ablation front" (DAF) structure has been described in [122] and [123], among others and depends on the interplay between radiative and electronic heat fluxes. In mid- to high-Z plasmas, the conduction zone strongly emits x-rays that escape in the direction towards the hot corona, but are

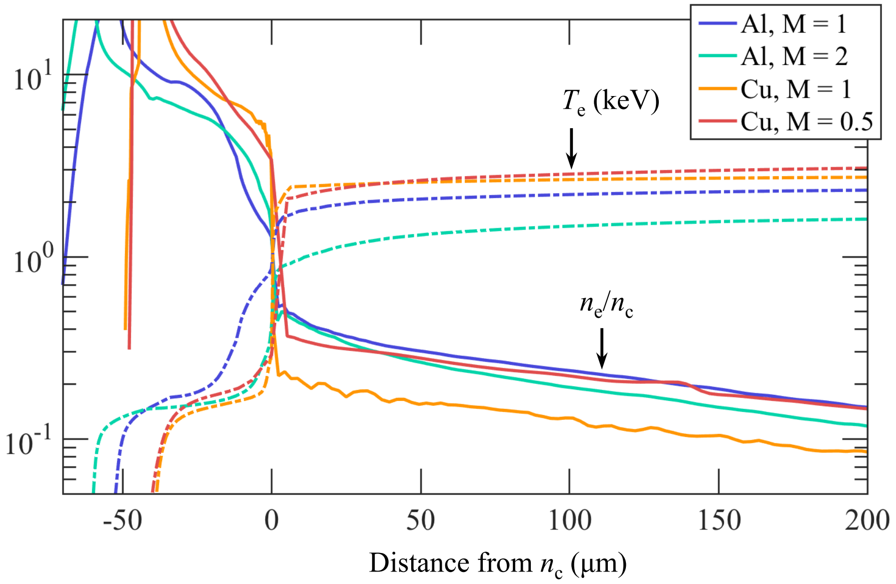

Figure 5.6: Electron density (solid lines) and temperature in keV (dashed lines) from 1D HYADES simulations at 0.8 ns, in a coordinate system where n_c is at the origin. The absorption and emission opacity multiplier, M is reduced to 0.5 for Cu and increased to 2 for Al to show the effect of radiation on the profiles.

absorbed within the more opaque, dense target. As a consequence, a radiation-driven heat wave forms in the dense target where radiation and matter are approximately in equilibrium and a radiation-driven ablation front forms, distinct from the electronic ablation front at lower density. The emission of radiation from the conduction layer helps balance electron heat flux into the dense target, leading to slower ablation and hence, profile steepening. The steepening from this effect may persist through the absorbing region until the plasma transitions to a free expansion. Radiation would similarly contribute to steepening of the profiles in the lower Z targets; in these cases, a distinct second ablation front does not form because the target is in general more transparent to x-rays and the transition between optically thin and thick plasma occurs much more gradually.

5.2.1 1D HYADES Simulations

In addition to the 2D CRASH simulations, we performed 1D radiation hydrodynamics simulations in planar geometry with the Lagrangian code HYADES to more directly observe how radiation affects the profiles. Diffusive radiation transport was calculated with 30 energy groups logarithmically-spaced from 1 eV to 20 keV a time-independent average-atom model was used to model ionization. Flux-limited electron heat transport was calculated using a flux limiter of $f = 0.06$. The incident laser irradiance was chosen to be 4×10^{14} W/cm^2, 1/3 of the peak irradiance in the experiments to account for some of the effects of lateral expansion and heat conduction. These simulation parameters were somewhat arbitrary, but their choice should not strongly influence the qualitative behavior across Z that we are interested in. Simulations were performed for Al, and Cu. To investigate radiation effects, we multiplied the emission and absorption opacities by a value M. In general, higher values of M increase the influence of radiation.

Figure 5.6 shows the predicted electron density (solid lines) and temperature (dashed lines) profiles at 1 ns for each of these materials, in a relative coordinate system where with n_c at the origin. In all cases, significant profile steepening occurs in the neighborhood of $n_c/4$, and is much more dramatic than in the CRASH simulations. In this region, the nominal case ($M = 1$) Cu has significantly steeper profiles and a higher temperature in the corona compared to Al. When the opacity multiplier is increased to $M = 2$ for Al, increased emission of radiation at densities near and above n_c steepens the profiles in this region to densities well below critical. In addition, the corona becomes much colder from increased radiative losses. The opposite occurs when the opacity multiplier is reduced to $M = 0.5$ for Cu. These results indicate the role radiation may have in producing shorter density length-scales in the experiments as the atomic number of the target is increased.

5.3 Conclusions

Simulations were performed in 2D and showed reasonable agreement with the density profiles from refraction measurements, reproducing the observed length-scale steepening with Z. The simulations lacked models of nonlocal electron transport and may have had inaccurate atomic physics models describing ionization and radiation transport. Despite these potential uncertainties, we believe the current results give a reasonable idea of how plasma conditions generally scale across the different materials in these experiments. Less efficient electron heat conduction and increased radiative losses are believed to lead to the shorter length-scales observed in the higher-Z targets. One-dimensional simulations with HYADES showed that increases in emission of radiation alone can steepen the profile in the region near critical.

CHAPTER 6

Models of Hot-Electron Production

Chapter 4 presented data from experiments measuring hot-electron production in laser-irradiated planar targets ranging from low-Z CH to high-Z Au. We observed that the inferred fraction of laser energy converted to hot electrons, f_{hot}, decreased by 3 orders of magnitude and the hot electron temperature, T_{hot}, decreased by a factor of 2 going from CH to Au. In addition, electron density length-scales, L_n, estimated from refraction measurements decreased by nearly a factor of 2 over this same range of materials. While we did not directly observe LPIs, these observations are consistent with their mitigation going to higher-Z, which may have resulted in part from increased thresholds from the steeper length-scales. However, the instability thresholds also depend on conditions that we did not observe directly, such as electron temperature, ionization and the laser irradiance profile. In this chapter we speculate on the origins of the inferred hot electrons by evaluating the importance of various LPIs and their scaling with Z to interpret our measurements. We use radiation hydrodynamic simulations discussed in Ch. 5 to predict how plasma conditions vary with Z as part of this interpretation.

6.1 Discussion

Before invoking predictions from radiation hydrodynamic simulations, we make inferences on hot-electron production based on the data alone. Estimates of the fraction of

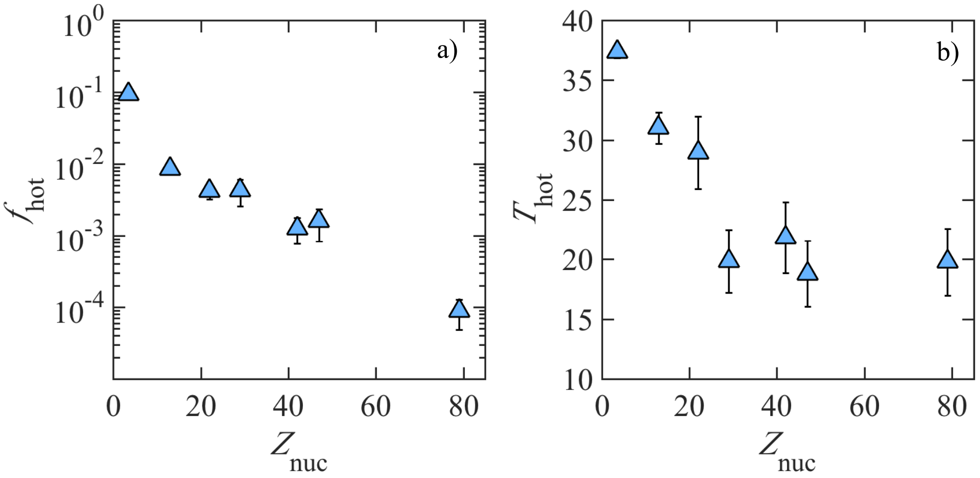

Figure 6.1: a) Hot electron fraction and b) temperature estimates from hard x-ray measurements described in Ch. 4.

laser energy converted to hot electrons, f_{hot}, and hot electron temperature, T_{hot}, described in Ch. 4 are again presented in Fig. 6.1 for reference. Two possible models of interest for generation of hot electrons in these experiments are the SRS and TPD instabilities driven by multiple laser beams. In both instabilities, anywhere from 2 to 4 of the beams may share a common EPW accompanied by a series of individual beam-driven scattered light waves or EPWs in the case of SRS and TPD, respectively. The thresholds for unstable growth of common EPWs shared by multiple beams can be significantly lower than if these EPWs were driven by single laser beams.

Multi-beam SRS:

For SRS in particular, the thresholds at a given density are determined solely by L_n and the beam geometry when damping can be neglected. For N laser beams with the same wavenumber, k_0 and frequency, ω_0, lying on a cone with half angle θ, the multi-beam SRS (MBSRS) convective gain is [84]

$$G_{\text{SRS}}^{\text{MB}} = \frac{\pi L_n k_c^2}{4c^2 k_{sy}} \sum_{i=1}^{N} |\mathbf{v}_{0i}|^2 \cos^2(\varphi_i), \tag{6.1}$$

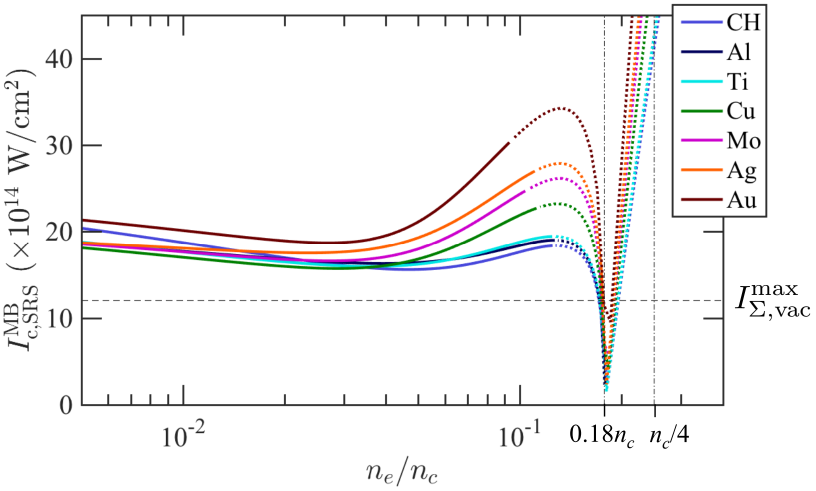

Figure 6.2: Convective thresholds for the MBSRS instability calculated along the target axis, using the length-scales from the fits to refraction data. Dotted lines represent where no refraction data was present

neglecting damping. Here, $k_c = k_0 \cos\theta + \sqrt{k_s^2 - k_0^2 \sin^2\theta}$ is the wavenumber of the common EPW, and $k_{s,i}(y) = (\omega_0/c)[1 - 2\sqrt{n_e(y)/n_c}]^{1/2}$ is the wavenumber of the i^{th} beam's scattered light wave with component $k_{sy}^2 = k_s^2 - k_0^2 \sin^2\theta$ parallel to the beam cone axis. In the plasma, we recall that the angle $\theta(y)$ is related to the vacuum cone half-angle, $\theta_v = 23^\circ$ via Snell's law (Eq. 2.22). Here, $\mathbf{v}_{0i}$ is the i^{th} beam's electron oscillation velocity and φ_i is the angle between the polarizations of the i^{th} beam and scattered wave. Scattered light waves from MBSRS may be driven with a variety of polarizations at a given density. However, growth is maximized and thresholds are minimized for those light waves whose polarization is most closely aligned with its driving laser's polarization. This occurs in the present geometry when $\varphi_i \approx 39 \pm 2^\circ$ ($\cos^2(\varphi_i) \approx 0.6 \pm 0.05$) over a wide range of densities. The MBSRS convective threshold, $I^{\mathrm{MB}}_{\mathrm{c,SRS}}$ can be found by setting $G^{\mathrm{MB}}_{\mathrm{SRS}} \geq 2$ for a minimum of $\exp(2\pi)$ growth [68]. We calculate this threshold along the axis for each material as a function of electron density using the estimated values of L_n from the fits to refraction data provided in Sec. 4.3.4, shown in Fig. 6.2. According to the estimates of L_n, we find that along the axis, the threshold for multi-beam convective growth is always above

15×10^{14} W/cm^2 (as high as 50×10^{14} W/cm^2 in the case of Au), except very close to the density $\frac{1}{4} n_c \cos^4 \theta_v \simeq 0.18 n_c$, where the MBSRS instability driven by 3 or 4 beams becomes absolute [84]. Damping would further increase these convective thresholds, which are already above the peak overlapped irradiance in vacuum, $I_{\Sigma,\text{vac}}^{\max}$ shown as the horizontal dashed line. It is possible that this instability is above threshold between $n_c/10 \lesssim n_e \lesssim 0.18 n_c$ where length-scales were not directly observed (dotted lines). However, even in the "best-case" scenario of CH, the length-scales in this region would have to increase by at least $\sim 50\%$ from those measured at $n_c/10$ for the threshold to be lowered to even the peak vacuum overlapped intensity, shown by the dashed horizontal line. In contrary, the simulations in Ch. 5 consistently predict shorter length-scales with increasing density in this region. We conclude from our observations that the convective MBSRS instability is not likely to contribute to hot-electron production, except perhaps in a small number of laser hot spots.

As mentioned above, the absolute MBSRS instability driven by 3 or 4 beams may exist at the density $0.18 n_c$ in this geometry. It occurs when the scattered light waves propagate essentially perpendicular to the density gradient and can remain in-phase with the laser over longer distances than in the convective case. If this instability is dominant, then the EPW spectra in the linear growth stage would feature a strong peak for the common waves, at $k = k_c \sim 0.9 \omega_0 / c$ along the axis. Electrons moving at these common waves' phase velocity, $v_p = \omega_c / k_c$ would have energy $E_{e^-} = \frac{1}{2} m_e (\omega_c / k_c)^2$. Taking this to be approximately the hot-electron temperature [84], we have

$$T_{\text{hot}} \simeq \frac{m_e c^2 \cos^2 \theta_v}{(8 - 2 \cos^2 \theta_v)}, \tag{6.2}$$

which equates to roughly ~ 70 keV–significantly higher than the <40 keV temperatures observed in these experiments (Fig. 6.1b). The expected temperature from common EPWs

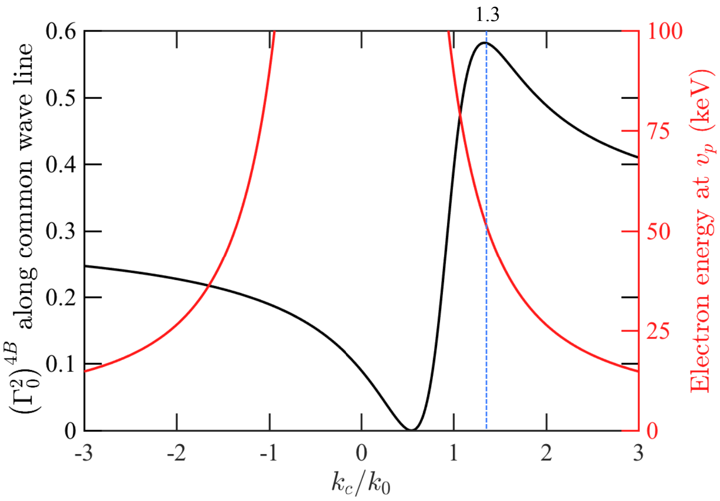

Figure 6.3: Normalized multi-beam TPD growth rate for the 4-beam OMEGA EP geometry along the common wave line, coinciding with the y axis ($\mathbf{k}_c = k_c\hat{\mathbf{y}}$) vs. wavenumber. The kinetic energy of an electron moving at the common wave's phase velocity, $v_p = \omega_c/k_c$ is shown on the right axis.

driven by 2 beams in absolute MBSRS is even larger since the angle between the beams and the common wave (equivalent to θ_v in Eq. 6.2) is smaller.

Multi-beam TPD:

For multi-beam TPD in this experimental geometry, the lasers may stimulate common EPWs with a variety of wavenumbers. However, the modes with the highest linear growth rate are expected to dominate the EPW spectrum during linear growth [124, 125]. Figure 6.3a shows the normalized multi-beam growth rate squared, $(\Gamma_0^2)^{\mathrm{MB}}$ (Eq. 2.52) for the 4-beam geometry along the common wave line, which coincides with the y axis. Plotted with respect to the right axis is the energy of an electron moving at a common wave's phase velocity. The growth rate peaks for common EPWs with wavenumber, $k_c \approx 1.3k_0$, giving $E_{e^-} \simeq \frac{1}{2}m_e(\omega_0/2.6k_0)^2 \approx 50$ keV, which is somewhat closer to the observed temperatures compared to the estimate for MBSRS, but still well above $T_{\mathrm{hot}} \sim 20$ keV seen for materials Cu through Au.

The discrepancy between the rough temperature estimates given above and those from the hard x-ray measurements is consistent with hot electrons being generated in the nonlinear regime of the multi-beam instabilities once higher wavenumber modes have developed from potentially a variety of mechanisms. The relatively long timescale of the laser pulse compared to the instabilities' e-folding times suggests that nearly all driven EPWs below the Landau cutoff may reach a time-averaged stable state. In general, the higher wavenumber EPWs occupy a larger volume in k-space than small-wavenumber EPWs, and therefore can weight the hot-electron spectrum towards lower energies. This could lead to a lower characteristic T_{hot} than predicted by the common waves' phase velocities alone.

Rather than being directly-driven by the laser, higher wavenumber EPWs may arise primarily due to broadening of common EPWs resulting from multi-beam TPD or SRS [97, 98, 124]. Broadening may occur via propagation of EPWs down the density gradient upon reflection at $n_c/4$, or cavitating Langmuir turbulence which leads to saturation in the nonlinear regime [97, 98, 124, 126, 127]. Vu et al. [124] observed in 2D reduced-PIC simulations of 2-beam TPD that during linear growth, the EPW spectra contained a peak corresponding to the common wave with maximum linear growth rate. In the saturated spectra, this peak had broadened and migrated to a wavenumber ∼4/3 times its value in the linear regime. This would correspond to a hot-electron temperature of ~ 30 keV, by a similar calculation as above.

The threshold for nonlinear saturation of growing EPWs decreases as IAW damping is lowered [71, 72, 95, 97]. This occurs as $\langle Z\rangle T_e/T_i$ increases, which will generally scale strongly with Z_{nuc}. We would therefore expect the nonlinear regime to persist for longer periods of time on average as Z_{nuc} increases, enabling more broadening towards higher wavenumbers. This is consistent with the lower T_{hot} observed with increasing Z_{nuc}. Collisional damping would contribute additional broadening of resonances and is expected to increase with Z_{nuc}. Even if this broadening were roughly symmetric about the resonance center, the larger volume that the higher wavenumbers occupy would lead to a lower characteristic T_{hot}.

At high enough values of $\langle Z\rangle T_e/T_i$, the IAW damping rate will bottom-out at some value set by the background Landau damping on electrons. This may explain the leveling of T_{hot} at $\sim$20 keV for materials Ti and above. The leveling of T_{hot} may also be evidence that the Landau cutoff ($k \lesssim k_{\max} \equiv 0.3/\lambda_D \propto T_e^{-1/2}$, where λ_D is the Debye length) has shifted to smaller wavenumbers as a result of the higher temperatures expected in these higher-Z plasmas. For electrons to be accelerated by Landau damping of LPI-driven EPWs to energies, $E_{\text{e}^-} \lesssim 20$ keV we find that T_e must be less than 3.6 keV, using $E_{\text{e}^-} \lesssim \frac{1}{2}m_e(\omega/k_{\max})^2$.

6.1.1 Variation of plasma conditions

At this point, we use the plasma conditions predicted by simulations to infer generally how growth of TPD and SRS would scale across materials, and evaluate consistency with our hot electron measurements. These inferences are limited by the simulations themselves–especially at high-Z (e.g. Ag)–but may still indicate the relative importance of the potential hot-electron generation mechanisms.

The electron temperature at 1.5 ns from the simulations is plotted vs. Z_{nuc} in Figs. 6.4a at 50 μm from the axis, where the squares and triangles are evaluated at $0.18n_c$ and $n_c/4$, respectively. At both densities, the temperature increases by nearly a factor of 2 going from CH to Cu, where it peaks at $\sim$4.7 keV, as a result of increased laser absorption and lower electron thermal conductivity from the significantly higher charge states available in the higher-Z materials. The slight drop after this point going to Ag is due to increased emission of radiation. Similar behavior across Z_{nuc} is seen at lower densities as well. These high temperatures suggest that for materials Ti and beyond, Landau damping would

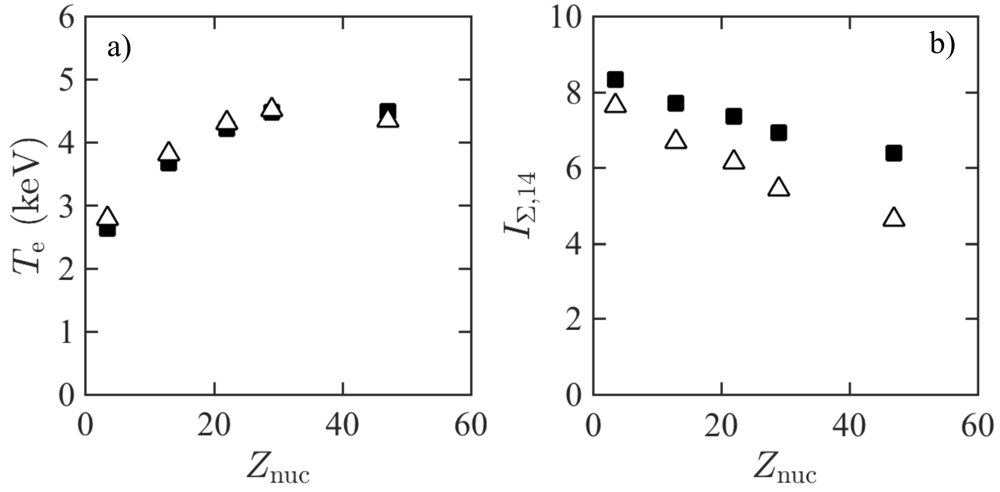

Figure 6.4: Plasma parameters from CRASH simulations vs target atomic number. Squares are at $0.18n_c$ and triangles are at $n_c/4$. a) Electron temperature, b) overlapped intensity ($\times 10^{14}$ W/cm^2). All are evaluated at 1.5 ns into the laser pulse.

indeed set a lower limit on the energy of hot electrons produced by multi-beam LPIs that is above the lowest $T_{\rm hot}$'s observed, around 20 keV.

The IAW damping rate, $\nu_{\rm iaw}$ was calculated for each of the simulated materials using the plasma conditions predicted by simulations. This was done for materials Al through Ag using the formula for a single-ion-species plasma provided in Bellan [89], and for CH using the two-ion-species analysis provided in Williams et al. [128]. Figure 6.5 shows that the damping decrement, $\Gamma_i = \nu_{\rm iaw}/\omega_r$ (where ω_r is the real part of the IAW frequency) rapidly drops from CH to Al and then continues to decrease only slightly going to higher Z, roughly independent of wavenumber. In general, the lower predicted IAW damping–implying lower saturation thresholds of LPIs–is consistent with the lower inferred $T_{\rm hot}$ going to higher Z. However, the precise dependency of $T_{\rm hot}$ on Γ_i is not clear, and may depend on other important physical mechanisms. In particular, $T_{\rm hot}$ decreased by almost 40% from Al to Cu, whereas Γ_i is predicted to only decrease by 15%.

Electron density, temperature and ionization profiles were post-processed to calculate the overlapped irradiance, using Eq. 2.15 with the incident 3D beam profile azimuthally

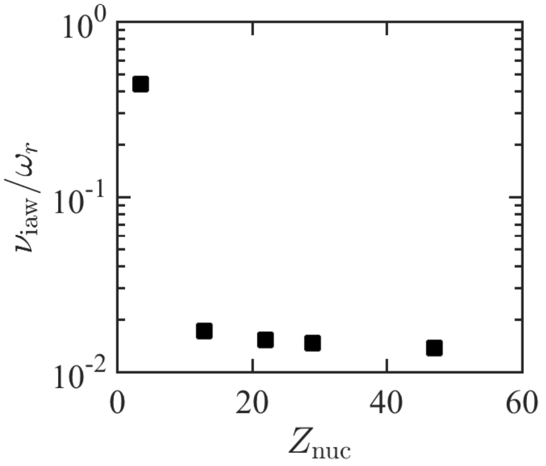

Figure 6.5: Predicted IAW damping rate divided by the real component of the frequency, ω_r evaluated at $0.18n_c$ and 1.5 ns into the laser pulse.

averaged around the target axis. The overlapped irradiance vs. Z_{nuc} is shown in Figure 6.4b at the location and densities corresponding to those in Fig. 6.4a. Enhanced laser absorption leads to a 25% drop in overlapped intensity at $0.18n_c$ going from CH to Ag. A larger, 40% drop in I_Σ is observed at $n_c/4$ across Z_{nuc} from the stronger absorption that occurs at a higher density.

6.1.2 Linear instability thresholds

We now use the plasma conditions predicted by simulations to infer generally how growth of TPD and SRS would scale across materials, and evaluate consistency with the inferred hot electron levels from hard x-ray measurements. For each instability, we calculate an above-threshold parameter $\eta \equiv I/I_{\mathrm{thr}}$, the ratio of driving intensity, I to the threshold intensity, I_{thr}. For significant growth, η should be near or greater than unity. In the case of the multi-beam instabilities, $I = I_\Sigma$.

The threshold for convective growth of TPD common waves is determined by setting the TPD convective gain $G_{\mathrm{TPD}} \approx 2$, [57] as was done previously for MBSRS in Sec. 6.1,

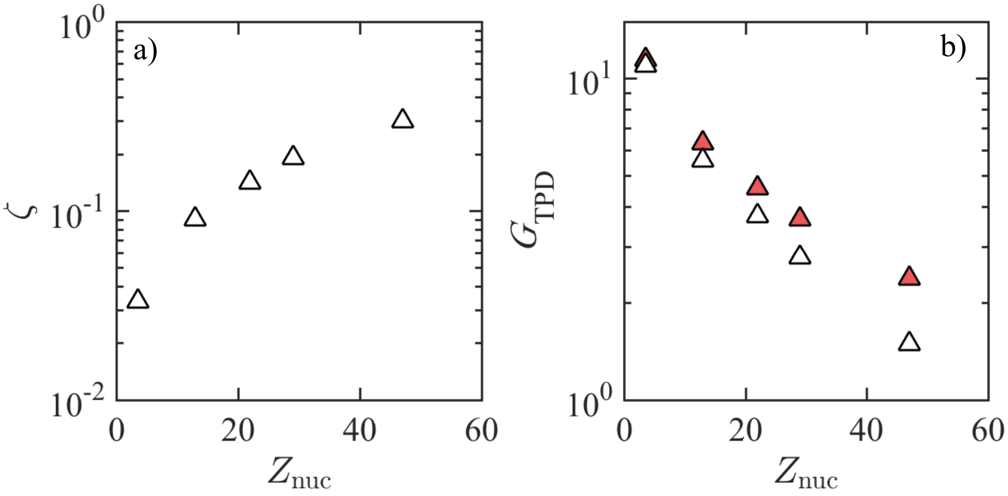

Figure 6.6: a) Damping parameter at $n_c/4$ for for multi-beam TPD, and b) TPD convective gains with (open) and without (red) damping of EPWs.

where

$$G_{\mathrm{TPD}} = 6 \times 10^{-2} \frac{I_\Sigma L_n \lambda_0}{T_e} \left(\Gamma_0^2\right)^{\mathrm{MB}}_{\max} . \tag{6.3}$$

Here L_n and λ_0 are in microns, T_e is in keV and I_Σ is in 10^{14} W/cm^2, all of which are evaluated at $n_c/4$. At $k_c \approx 1.3k_0$ in Fig. 6.3, $(\Gamma_0^2)^{\mathrm{MB}}$ has a maximum value of 0.58. For convective growth of LPIs in an inhomogeneous plasma, damping modifies the gain [129] in Eq. 6.3 by a factor, $F(\zeta)$ (and the convective threshold by $1/F(\zeta)$),

$$F(\zeta) = \begin{cases} \frac{2}{\pi}\left(\arccos(\zeta) - \zeta\sqrt{1-\zeta^2}\right), & \text{if } \zeta \leq 1 \\ 0, \text{ otherwise}, \end{cases} \tag{6.4}$$

where $\zeta = \sqrt{\nu_1 \nu_2}/\gamma_0$ and ν_1 and ν_2 are the amplitude damping rates of the decay waves and γ_0 is the LPI homogeneous growth rate. For multi-beam TPD, $\zeta = \sqrt{\nu_{\mathrm{c}}\nu_{\mathrm{b}}}/\gamma_{0,\max}$, and $(\gamma_0^2)_{\max} = \frac{2}{c n_c m_e}\left(\frac{k_0}{2}\right)^2 I_\Sigma \left(\Gamma_0^2\right)^{\mathrm{MB}}_{\max}$ is the maximum homogeneous temporal growth rate squared at $n_c/4$ for multi-beam TPD. The amplitude damping rates of the common (c) and backward propagating (b) EPWs are $\nu_{\mathrm{c,b}} = \nu_{ei}/2 + \nu_L(k_{\mathrm{c,b}})$ where $\nu_L(k_{\mathrm{c,b}})$ are the Landau damping rates evaluated at the wavenumber of either wave. ζ is plotted for each material in Fig. 6.6a, showing that damping becomes significant ($\zeta \gtrsim 0.1$) above Al. Landau damping of the common-wave reaches a maximum at Cu($Z_{\text{nuc}} = 29$), where T_e at $n_c/4$ peaks, and is $\sim 50\%$ of the collisional damping. The convective gains are plotted in Fig. 6.6b with (open triangles) and without (red triangles) the effect of damping. While damping is predicted to reduce the gain by a factor of $10 - 40\%$ for materials Ti through Ag, the gain has already been lowered by a factor of 5 from smaller length-scales, higher temperatures and greater absorption of the laser prior to it reaching $n_c/4$.

The absolute threshold for TPD driven by a single beam in an inhomogeneous plasma is [81] $I^{\text{SB}}_{\text{TPD,abs}} = 81.3T_e/(L_n\lambda_0)$, using the same units as above. Zhang et al. [125] predicted that this instability can also be driven by multiple laser beams. However, even excluding the effects of multiple beams or damping, we find that its threshold is generally above that of convective multi-beam TPD with damping. Absolutely unstable modes may still be present, but presumably at smaller wavenumbers than in the convective case [125].

The threshold from inhomogeneity for the absolute MBSRS instability in units of 10^{14} W/cm^2 is [84]

$$I^{\text{MB}}_{\text{SRS,abs}} \geq \frac{3 \times 10^3}{f_S \lambda_0^2} \left(L_n/\lambda_0\right)^{-4/3} \tag{6.5}$$

where L_n (evaluated at $0.18n_c$) and λ_0 are again in microns. The factor, f_S accounts for the beam geometry similar to the normalized multi-beam growth rate for TPD, and has a maximum value of 1.78 in this experiment when the angle between the polarizations of the lasers and scattered light waves is a minimum. The threshold in Eq. 6.5 is updated to include the effect of damping following the analysis in Afeyan et al. [130] for oblique stimulated Raman sidescatter by subtracting the effective damping rates of the decay waves from the inhomogeneous growth rate. However, we find that at $0.18n_c$, inhomogeneity is the dominant mechanism in setting the threshold, which is increased by no more than

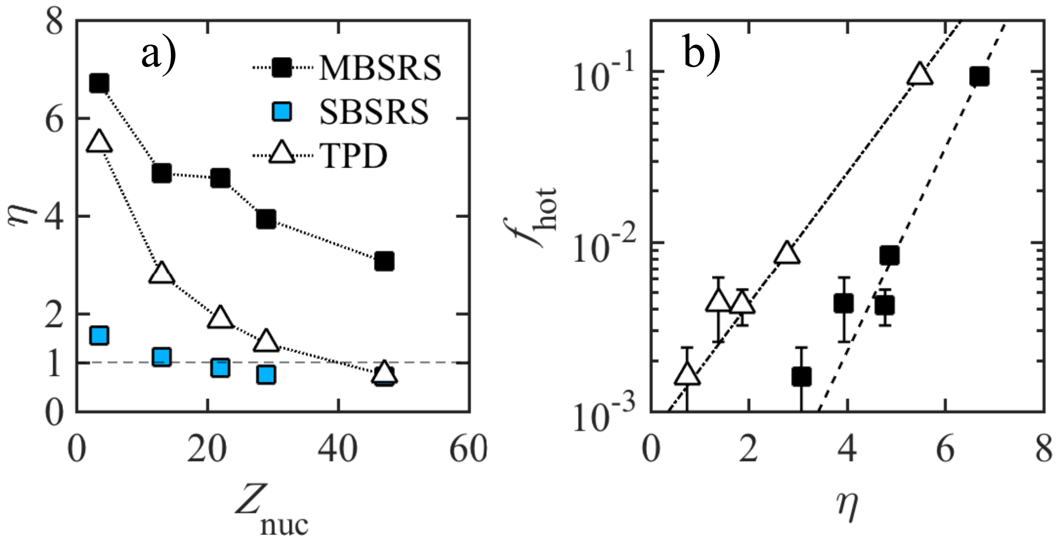

Figure 6.7: a) Threshold parameter, $\eta = I/I_{\text{thr}}$ vs. Z_{nuc} calculated from simulations at 1.5 ns for the absolute MBSRS instability at $0.18n_c$, the single-beam stimulated Raman backscatter (SBSRS) at $n_c/10$ and the convective multi-beam TPD instability at $n_c/4$ with the effects of damping. b) f_{hot} from Fig. 6.1 vs the multi-beam threshold parameters from a), where the lines are exponential fits for guidance.

5% percent from collisional and Landau damping of the common EPWs and collisional damping of the scattered light waves.

The threshold parameters, η for convective multi-beam TPD and absolute MBSRS with damping are shown in Fig. 6.7a as the open triangles and black squares, respectively, vs. Z_{nuc} for the materials simulated. The simulations indicate that η is generally near its maximum in both cases around 1.5 ns, but reaches unity as early as 0.4 ns for several materials. We see that for both instabilities, η decreases with increasing Z_{nuc}, and that both are predicted to be above threshold except perhaps in the case of Ag where damping is expected to significantly reduce growth of TPD. The TPD threshold parameter is predicted to be less than that of MBSRS, but is more sensitive to Z_{nuc} because of the increase in T_e and larger drop in I_Σ going to higher Z. The threshold parameter for absolute SRS backscatter driven by a single beam is also shown, as the blue squares, evaluated at $n_c/10$ where the phase velocities of the EPWs correspond to the acceleration of electrons to ~20 keV. This threshold parameter is predictably lower than those of the multi-beam instabilities, except in the case of Ag where it is comparable to that of TPD.

Figure 6.7b shows the estimates of f_{hot} from measurements plotted against the threshold parameters inferred from simulations for the multi-beam instabilities in question. f_{hot} scales with η in both cases, consistent with mitigation of these instabilities and their consequent hot-electron production as length-scales steepen and absorption becomes enhanced going to higher Z. However, we are unable to determine definitively which instability, if either, dominates in producing hot electrons, as well as how the plasma conditions are varying across Z based on these measurements. We also note that the single-beam LPIs that are above threshold may still contribute significantly to production of hot electrons; while single-beam LPI growth is generally lower and thresholds are higher, the matching conditions are easier to satisfy than in the multi-beam case because only one beam needs to be in-phase with the decay waves. Furthermore, because hot electrons are accelerated during the nonlinear regime, f_{hot} will ultimately depend on nonlinear saturation mechanisms. Regardless, we still expect f_{hot} to correlate with η, since lowering the linear threshold or increasing the average intensity increases the number of laser hot spots above threshold that can drive EPWs to saturation and accelerate hot electrons. In the future, calculations using a 3D Zakharov model may be performed to study the evolution of the nonlinear regime for these plasmas and the coupling between EPWs and IAWs [95,97].

6.2 Conclusion

In summary, models of hot-electron production were presented to interpret the observed decreases in hot-electron fraction, f_{hot} and temperature, T_{hot} with Z_{nuc} that were inferred from hard x-ray measurements in Ch. 4. The decrease in T_{hot} was consistent with more efficient EPW spectral broadening from decreased IAW damping expected at higher Z.

Additionally, the eventual leveling of T_{hot} around $\sim$20 keV was consistent with the Landau cutoff shrinking to smaller wavenumbers from the higher temperatures expected at higher Z. Both multi-beam TPD and multi-beam SRS were predicted to be significantly above threshold in most cases, based on the plasma conditions calculated from the radiation hydrodynamic simulations that were presented in Ch. 5. For all LPIs evaluated, the threshold parameters were highest for multi-beam SRS, suggesting that it may play a comparable or greater role in producing hot electrons compared to TPD. The threshold parameters were predicted to decrease by a factor of $\sim$5 and $\sim$2 from CH to Ag for TPD and SRS, respectively due to shorter length-scales as well as increased temperatures and decreased overlapped irradiance from more efficient laser absorption going to higher Z. These predictions support the connection between measured hot electrons and mitigation of multi-beam laser-plasma instabilities at high-Z. Future measurements of plasma conditions as well as TPD and SRS common wave amplitudes using Thomson scattering will help confirm our inferences from the present data and simulations.

CHAPTER 7

Mitigation of the Hard X-ray Background in Backlit Pinhole Imagers

This chapter is based on the article "Mitigation of hard x-ray background in backlit pinhole imagers," written by the author and published in Review of Scientific Instruments, June 2016 [131]. Experiments were performed on the OMEGA laser to test whether hard x-ray background could be mitigated in backlit pinhole imagers by controlling laser-plasma instabilities. Based on previous work [86, 94], we hypothesized that laser-plasma instabilities and production of hot electrons leading to hard x-ray background can be reduced by increasing the atomic number of the irradiated scaffold material holding the microdot away from the pinhole substrate. As we have demonstrated in previous chapters, a higher atomic number is correlated with shorter electron density length-scale, and higher plasma temperature due to enhanced collisional laser absorption, lowering the instability growth [67, 94]. In combination with increased collisional damping, growth of the electron plasma waves that accelerate hot electrons becomes inhibited.

7.1 Experimental Design

Diagrams of the backlit pinhole imagers used in this experiment are shown in Fig. 7.1. In the nominal design (A) a 5-μm thick V dot with 300-μm diameter is attached to a 25-μm

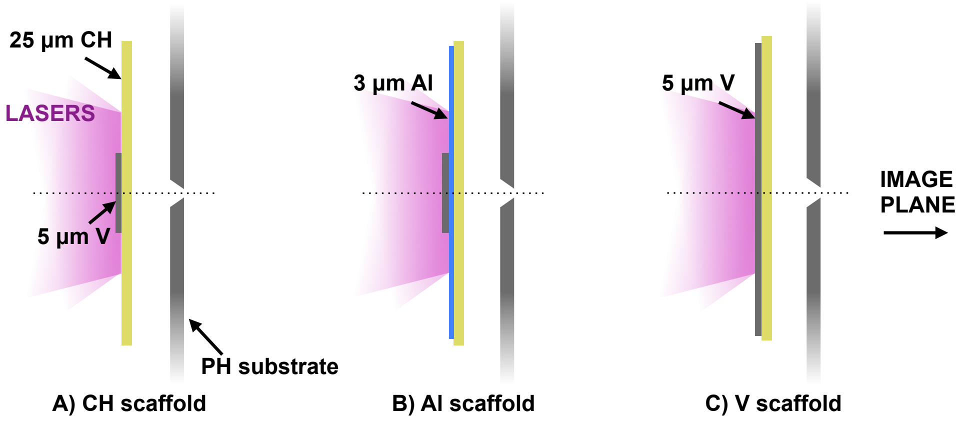

Figure 7.1: Side-on schemata of the backlit pinhole imagers: design with A) bare CH scaffold; B) Al intermediate layer; C) V intermediate layer.

× 3-mm square CH scaffold that sits 500 μm behind a Ta pinhole (PH) substrate. Lasers heat the V dot and scaffold, producing a thermal plasma that emits V He-like x-rays at 5.18 keV. Fast blow-off plasma from the low-Z scaffold inhibits V expansion around the PH substrate and emission of x-rays towards the un-gated detector. The 50-μm thick × 7-mm square PH substrate contains a tapered aperture from $50 - 20\,\mu$m to collimate the soft x-ray emission into a quasi-point source while minimizing vignetting. It also prevents the blow-off plasma from interacting with the primary object.

Five laser beams of 351-nm light with 450 J/beam irradiated the targets in a 1-ns flattop pulse. Three beams had incident angle 59°, and two beams had incident angles 42° and 22°, relative to target-normal. Each beam was polarization-smoothed and passed through distributed phase plates having a 4th-order super-Gaussian intensity profile. The final $\sim$700-μm FWHM laser spot gave a peak irradiance of 4.9×10^{14} W/cm^2 and ratio of $\sim$5:1 between irradiated areas of scaffold and V microdot. Based on the geometry, the largest overlapped irradiance that could be coupled into TPD or SRS common waves is $\sim 3 \times 10^{14}$ W/cm^2 via the three 59° beams. From these irradiances and beam geometries we expect temperatures of hot electrons produced in the plastic targets to be $\lesssim 20$ keV [94,99].

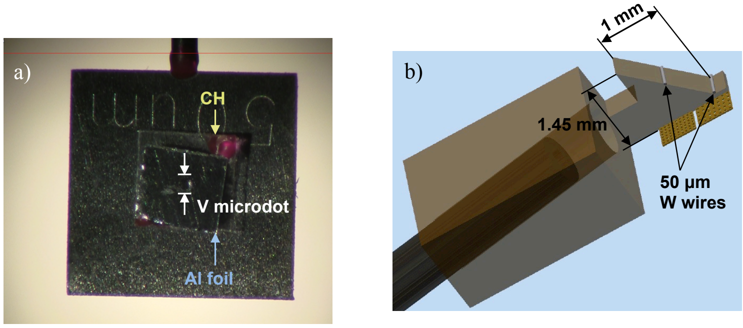

Figure 7.2: a) Photograph of backlit pinhole imager with Al scaffold. b) Rendering of resolution test target.

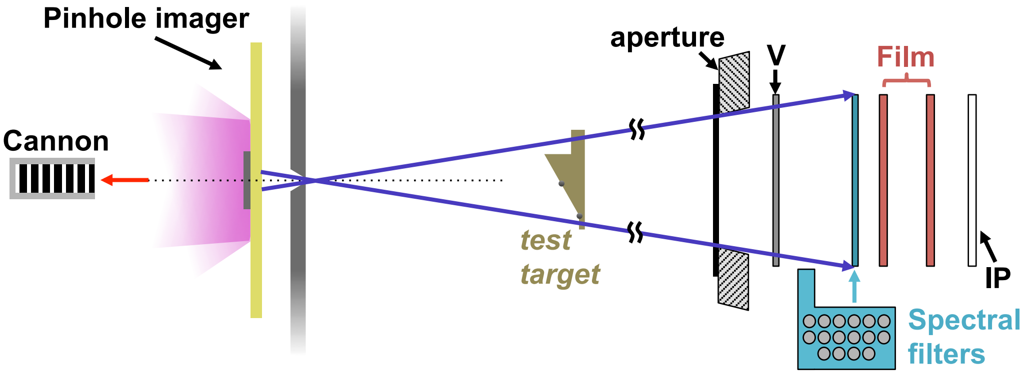

Figure 7.3: Diagram of backlit pinhole radiography to test strategies to mitigate hard x-ray background. A resolution test target was imaged onto 2 film layers and an image plate loaded in an RSPCA mount. A cannon spectrometer detected hard x-rays from the irradiated side of the pinhole imager, opposite the imaging direction.

Two additional pinhole imagers were used to test whether hard x-ray background could be mitigated by varying the target-irradiated material. In (B), a 3-μm-thick × 2.5-mm square intermediate layer of Al was placed between the V microdot and existing 25-μm CH (picture shown in Fig. 7.2a). In (C), a 5-μm-thick × 2.5-mm square V foil replaced the dot altogether, eliminating the potential collimating effect of the lower-Z scaffold. A single CH scaffold target and two of both the Al and V scaffold targets were tested.

7.1.1 X-ray diagnostics

Radiography

Table 7.1: Spectral filter materials, thicknesses and nominal energy band defined by the indicated pair filters' K-edges. "Low" and "High" indicate whether the filter's K-edge is the lower or upper bound of the energy band. Filters are numbered in relation to Fig. 7.5.

Filter Numbers (Low, High)	Low filter (μm)	High filter (μm)	Energy band (keV)
(14,13) & (5,10)	Ti(12.5)	V(8)	4.97 - 5.46
(15, 12)	V(25) + Al(5)	Fe(12.5) + Al(5)	5.46 - 7.11
(12, 11)	Fe(12.5) + Al(5)	Zn(10)	7.11 - 9.67
(8, 7)	Zn(35)	Mo(10)	9.67 - 20.0
(7, 6)	Mo(10)	Ag(7)	20.0 - 25.53
(6, 16)	Ag(7)	Sn(9)	25.53 - 29.21
(4, 3)	Sn(150)	Ta(25)	29.21 - 67.41
(2, 1)	Ta(50)	Au(35)	67.41 - 80.72

As depicted in Fig. 7.3, x-rays that made it through the PH aperture back-lit a resolution test target at a distance of 11.5 mm onto x-ray detectors another 274 mm away, resulting in a magnification of $M \simeq 25$. The resolution target (Fig. 7.2b) consisted of two Au grids, with 42- and 62-μm pitch and 10- and 25-μm bar width, respectively, attached to an acrylic ramp used to help calibrate x-ray signal intensity. The detector stack, which was housed in the TIM-based Rotational Static Pinhole Camera Array (RSPCA), consisted of 2 layers of Agfa D7 x-ray film in front of a Fuji BAS MS-type image plate (IP). Kapton and Be blast shields and an 8-μm V "discriminator" filter light-sealed the detectors and attenuated x-rays with $E \leq 2$ keV by a factor greater than 4×10^6 and $5.4 \leq E \leq 8$ keV by a factor between 4 – 40. Image plates were scanned at 50-μm resolution (equivalent to 2.5 μm at the object plane) with a scanning sensitivity of $S = 4000$ and temporal fade was corrected using the fade curve in Ref. [93].

Additional spatially-separated filters of material varying from Al to Au were placed between the V filter and film to provide spectral content of the incident x-rays in the range $\sim 2 - 80$ keV, mounted on a 178-μm-thick Cirlex® filter holder. The materials and thicknesses are detailed in Table 7.1, where the numbering corresponds to the spatial or-

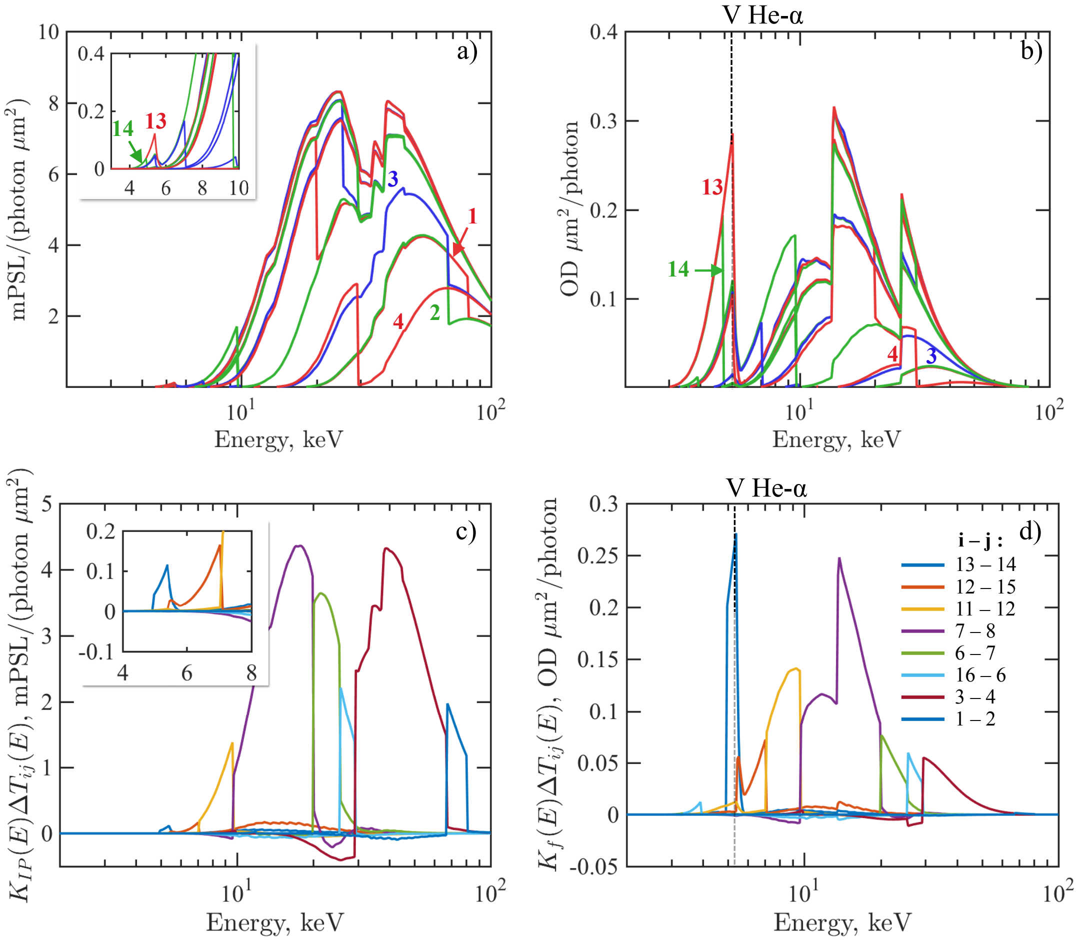

Figure 7.4: Detector response (sensitivity × total transmission) for each of the 16 spectral filter channels listed in Table 7.1. a) Response for the IP and b) response for the film layer closest to TCC. Curves c) and d) are the differences in detector response between filters i and j, $K(E)\Delta T_{ij}(E)$ for the IP and film, respectively for selected Ross pairs.

dering in the radiograph in Fig. 7.5a. Each filter provides a separate "channel" of spectral information. The detector response or amount of signal produced per photon of energy E behind the i^{th} channel/filter, $R_i(E) = K(E)T_i(E)$ is calculated as the product of the spectral sensitivity, $K(E)$ of the IP or film [93, 132–134] and the channel's total transmission, $T_i(E)$, neglecting fluorescence. $T_i(E)$ includes transmission through the blast shield and 8-μm V and is calculated using the XCOM photon cross-section database [100]. The response curves of the 16 spectral filters are shown in Fig. 7.4 for a) the IP and b) the film layer closest to source. We can see that the image plate responses peak at energies 20–

60 keV, whereas the film responses peak at lower energies, 4–25 keV. The relatively low image plate response at energies $\leq$7 keV is due to decreased sensitivity at these energies and attenuation through the preceding film layers. To aid with reconstruction of the spectrum at energies below $\sim$7 keV, three additional channels were incorporated into the total data set: two from separate regions of the polyimide ramp and one from the center of the image where no object or extra filtering were present.

The materials and thicknesses of the spectral filters were initially chosen so that certain filter pairs would create nominal band-pass filters with edges defined by the two materials' K-edges, as in the Ross-pair technique [135]. With proper matching of thicknesses, the difference in transmission between two filters composing a pair may be everywhere negligible except between the K-edges of the two materials. Any difference in detected signal between the two filters, therefore, must come predominantly from x-rays with energies between the two K-edges in the pair. The difference in detector response between filters i and j, $K(E)\Delta T_{ij}(E)$ is shown for the filter pairs designed for this experiment in Figs. 7.4c and d, for the IP and first film layer, respectively. Each curve corresponds to a separate Ross pair, and several show sizable "wings" outside the nominal energy band. Using the difference signal, d_{ij} between channels i and j, a simple estimate of the number of incident photons/detector pixel or area with energies between K-edges i and j, N_{ij} is

$$N_{ij} \approx \frac{|d_{ij}|\Delta E_{ij}}{|\int_{E_i}^{E_j} K(E)\Delta T_{ij}(E)dE|}, \tag{7.1}$$

assuming the spectrum to be approximately flat over the energy band and neglecting effects of the wings except as a source of error [41, 93]. In Sec. 7.2.3, we propose a more complete approach to calculate the number of photons in each energy band that properly accounts for the effects of wings on all neighboring energy bands. However, we find that the covariances introduced by subtracting data points lead to a worse spectral reconstruc-

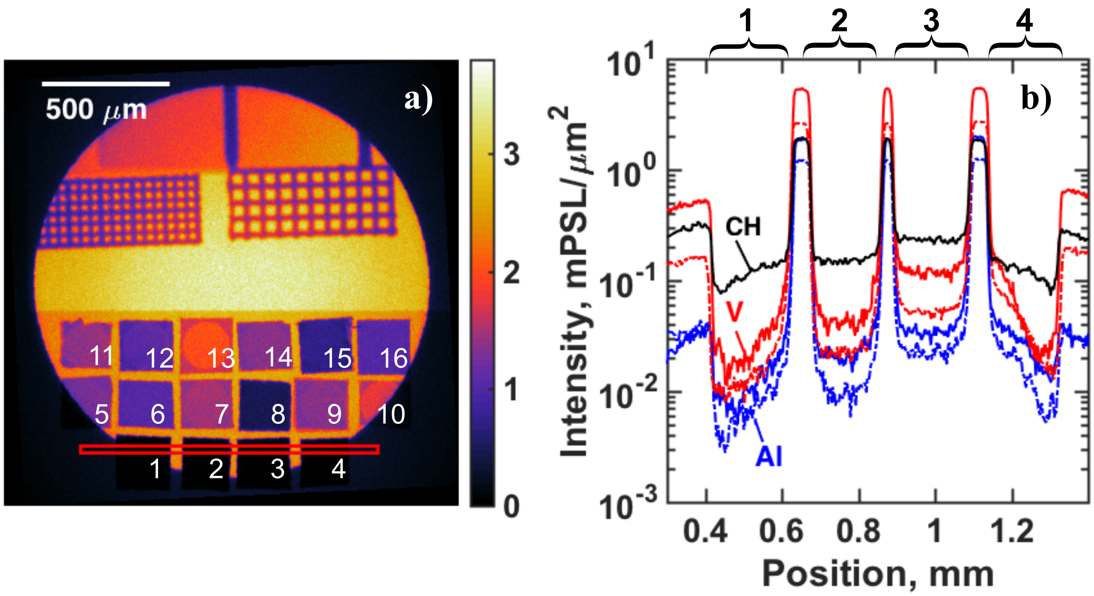

Figure 7.5: a) Radiograph from recorded on the image plate from shot 74180 using a V scaffold target. Labeled spectral filters are placed in the detector plane. Scale corresponds to the object plane. b) Lineouts across the highest-Z filters (1 - 4) for each shot. The black line corresponds to the CH scaffold, and the blue and red lines correspond to the Al and V scaffolds, respectively, where solid and dashed lines indicate separate shots.

tion than when using channels individually.

7.2 Experimental Results

7.2.1 Radiography

Figure 7.5a shows an example radiograph recorded on an IP using a V scaffold, with test target above and numbered spectral filters below. The aperture of the RSPCA snout results in a circular image on the detector. Spatial resolution was calculated approximating the pinhole's point-spread function as a Gaussian blur. Fitting the blur of the Au grid edges in the film radiographs showed resolution varied slightly across scaffold materials, with FWHM $= 13.5 \pm 3$ μm in the vertical and horizontal directions—on the order of the 20-μm pinhole size.

Lineouts across the four highest-Z filters (depicted by the red rectangle) from each shot are compared in Fig. 7.5b. Black, blue and red lines correspond to the CH, Al and V scaffolds, respectively, where solid and dashed lines indicate separate shots. The mean signal behind each filter decreases by a factor of 2–10 when going from the CH scaffold to the Al and V scaffold, respectively. Virtually no He-α x-rays are detected behind these filters since the maximum filter transmission at 5.18 keV is $\sim 10^{-10}$, through the 25-μm Ta. At 10 keV, the combined IP response [93] and transmission through the 25-μm Ta is at most 1/60 that of the neighboring Cirlex® filter holder. Therefore, any reduced signal behind filters 1 through 4 shot-to-shot reflects a loss of hard x-rays at energies well above that of the He-α line. This conclusion is further supported by the increase in signal behind the Cirlex®with the V scaffold relative to the CH scaffold. In addition, a cannon filtered spectrometer [106] viewing the irradiated side of the target showed up to a 2 order of magnitude drop in signal on channels sensitive primarily to x-rays with energy $>$20 keV.

We note that the signal behind the high-Z filters from the V-scaffold targets is consistently higher than that from the Al-scaffold targets. As will be discussed below, we attribute the higher signal to both increased thermal bremsstrahlung from the higher-Z V plasma, and detector exposure to emission from V plasma whose expansion beyond the edge of the pinhole substrate was not tamped with a lower-Z scaffold plasma.

7.2.2 Assessment of nonuniformities and other characteristics

Distinct nonuniformities were observed in the radiographs for most targets, whose shape and likely origin varied across scaffold materials. Figure 7.6 illustrates how these nonuniformities may originate in the pinhole imaging geometry for each scaffold material from either hard x-rays, microdot misalignment or extended sources. It is used as a supplement to the radiographs and will be described throughout this section as needed.

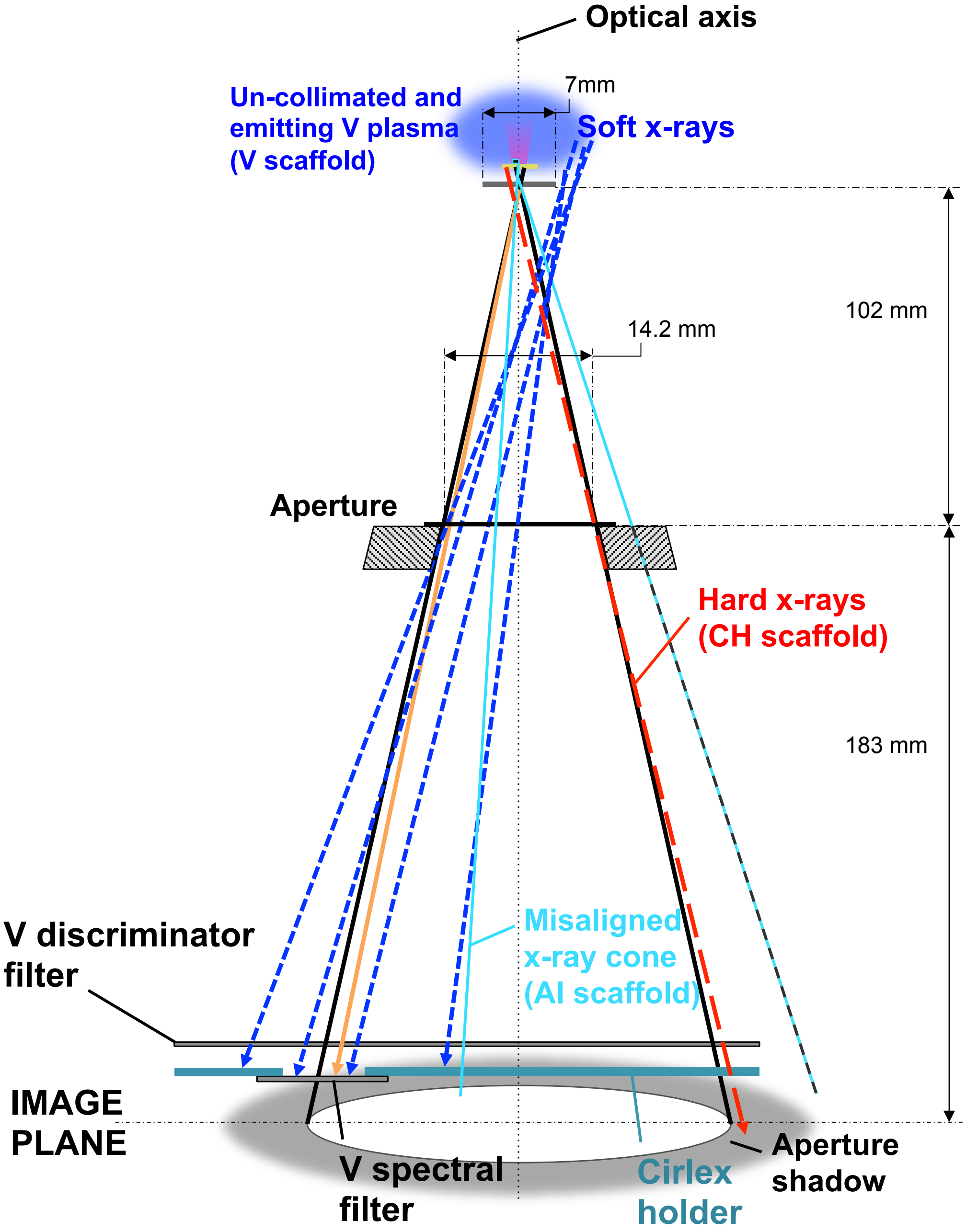

Figure 7.6: Illustration of how radiograph signal non-uniformities may originate for the different scaffold materials. Hard x-rays can produce a flare just beyond the aperture shadow, seen with the CH scaffold. Misalignment of the microdot would create a sharp cutoff in signal along the radiograph, seen possibly with the Al scaffold. Uncollimated expansion of the V plasma (expected with the V scaffold) may cause an extended source of soft x-ray emission beyond the edge of the pinhole substrate that would expose a large area of the detector, well into the aperture's shadow.

CH Scaffold:

The film and IP radiographs from the pinhole imager using the CH scaffold are shown in Figs. 7.7a and b, respectively. Figure 7.7c shows lineouts from the radiographs across the central unattenuated region (green lines) and acrylic fiducial ramp (black lines), which correspond to the regions outlined by the boxes of same color and line style in the images of the radiographs to the left. Dashed and solid lineouts are from the film and IP radiographs with intensity in units OD and mPSL/μm^2, respectively. Looking at the solid green line we see that the unattenuated signal across the radiograph has a roughly bell-shaped profile, varying from the maximum value by more than 20%. A similarly-shaped but much more subtle profile exists over the same region on the film, with less than 10% variation from the maximum. The black dashed line of the ramp profile recorded on the film shows a very clear exponential decay that agrees well with what we would expect from a spatially uniform V He-α source being attenuated through the ramp. Conversely, the solid black line representing the ramp profile recorded on the IP shows a much more gradual decay from right-to-left, superposed with a nonuniform feature similar to that in the unattenuated profile. These features of the data agree with the hypothesis that the non-uniformity is from x-rays at energies significantly above the 5.18 keV V He-α line; they contribute relatively little signal to the film, but significant signal to the IP whose sensitivity peaks at higher energies.

The precise origin of the non-uniformity's shape is unknown and may be a combination of several factors. Even if hot electrons are produced preferentially in the CH plasma surrounding the V microdot, they will diffuse both across and outside the laser spot. Production of hard x-rays from these hot electrons will be more efficient in the higher-Z V plasma and remaining solid material than in the lower-Z plastic. This could lead to an emission profile that decays radially as the ions from which the x-rays are produced transition from V to carbon and hydrogen. Additionally, the hot-electron diffusion radi-

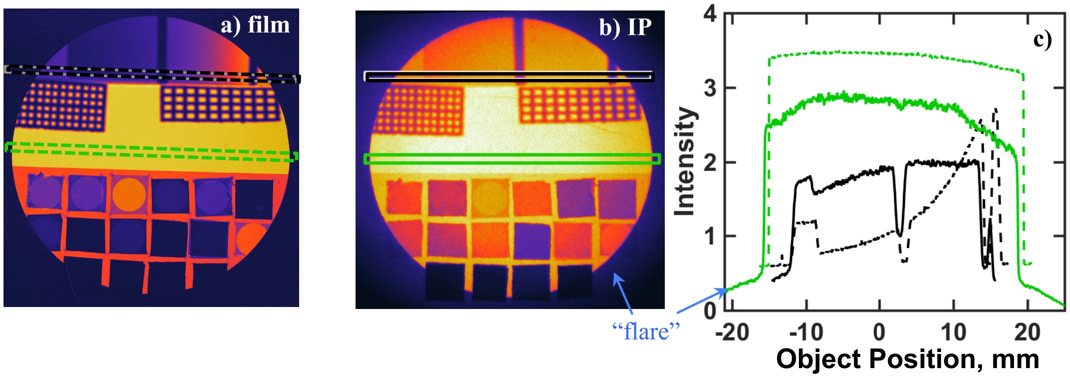

Figure 7.7: Radiographs from a pinhole imager using the nominal CH scaffold recorded on a) the first layer of film and b) the IP. c) Lineouts across the radiographs in a) and b) of the central unattenuated region (green lines) and across the acrylic fiducial ramp (black lines). Regions where lineouts were taken correspond to the boxes of same color and linestyle as in the radiographs. Dashed and solid lineouts are from the film and IP radiographs with intensity units OD and mPSL/μm^2, respectively. Lineouts from the IP radiograph show significant nonuniformity. The film fog has not been subtracted in the lineout.

ally outward would likewise contribute to this decay as fewer electrons reach larger radii due to $1/r$ falloff. The presence of a “flare” observed surrounding the circular aperture’s shadow in Fig. 7.7b supports this notion, which is much significantly fainter in the IP radiographs from V scaffolds and completely absent in those with Al scaffolds. The flare is likely from x-rays with energies well above that of the V He-α line because it is not observed in the film (Fig. 7.7a). More than 40% of x-rays with energy >40 keV transmit through the 50-μm Ta pinhole substrate. As depicted in Fig. 7.6 by the red arrow, some of these transmitted hard x-rays that originate far from the optical axis could lead to signal outside the aperture shadow. Some of this signal contributing to the flare could be from x-ray fluorescence in the V discriminator filter in front of the Cirlex®spectral filter holder; however, this contribution must apparently be small because the flare is not observed in the film which has a higher sensitivity to the 4.95 keV V Kα x-rays than to harder x-rays.

Al Scaffold:

Figure 7.8a shows the radiograph recorded on the image plate from shot 74176, in which an Al scaffold was used. The image shows a nonuniform feature in which from

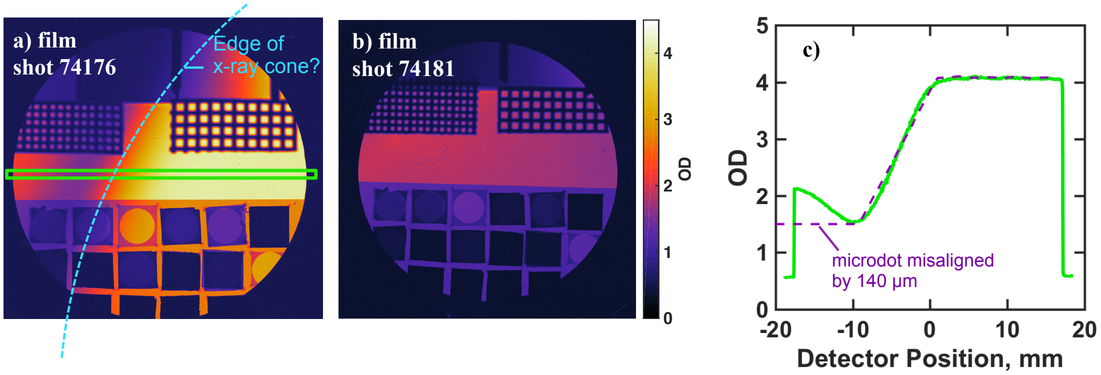

Figure 7.8: a) Radiograph recorded on first layer of film from shot 74176 with Al scaffold, showing nonuniformity from right-to-left. The cyan dashed line represents the edge of the x-ray cone from a potentially misaligned V microdot. b) Radiograph recorded on first layer of film from shot 74181 with Al scaffold, with considerably lower overall signal. c) The green line is the lineout from the boxed region in a) showing the magnitude of the nonuniformity. The purple dashed line is the simulated intensity profile from a microdot that is misaligned 140 μm to the left of center.

right-to-left the intensity is roughly flat and sharply drops off over ∼8 mm in the detector plane (∼400 μm in the object plane). This is illustrated more clearly by the green lineout in Fig. 7.8c of the boxed region in Fig. 7.8a. The nonuniformity appears to come from a variation in soft x-ray intensity across the image, based on a comparison of the intensity across the Cirlex®to the intensity across the unattenuated region between the spectral filters and grids in Fig. 7.8a. One hypothesis for such a feature is the translational misalignment of the microdot relative to the pinhole. The Al scaffold design was most susceptible to this issue because the pinhole could not be viewed through the opaque Al layer, whereas the CH scaffold was optically transparent. The result of misalignment is described pictorially in Fig. 7.6 by the cyan rays that outline the misaligned x-ray cone projected through the pinhole. The edge of such a cone with an expected diameter of 144 mm at the detector reasonably outlines the nonuniformity in 7.8a, shown by the dashed cyan line. The shape of the drop-off in Fig. 7.8c is consistent with a profile that results from approximately 140-μm misalignment of the microdot with respect to the pinhole

140 μm, to the left of the image's center. This is modeled by ray-tracing a microdot-sized He-α source through the pinhole substrate and shown as the purple dashed line in Fig. 7.8c, where a constant underlying background has been added. The model shows sharp "knees" where attenuation starts and the source abruptly stops, which we would expect to round out (like in the green profile) from mixing of the microdot and Al plasmas, as well as a smoothed Ta density profile from ablation of the pinhole wall.

The lineout in Fig. 7.8c contains an intensity minimum at -9 mm, and then increases out to the aperture's shadow at -15 mm–a feature that is inconsistent with the nonuniformity resulting solely from misalignment. The nature of this feature is unclear. Rather than translational misalignment of the microdot, the nonuniformity in shot 74176 may have resulted from partial obstruction of the laser or the He-α emission, e.g. by glue or dust. In the end, not enough data are available to make any strong conclusions about the non-uniformity in shot 74176, aside from it being low-energy in nature.

In the other Al scaffold shot (74181), the radiograph, Fig. 7.8b, showed factor of ~ 2 lower signal overall than in the flat signal region in Fig. 7.8a. We believe the lower signal to have resulted from a smaller pinhole in shot 74181, which is consistent with the improved resolution observed in this shot. The Gaussian blur FWHM was 11.4±0.3 in shot 74181 vs. 14.2±0.5 in shot 74176, corresponding to a factor of 1.25 smaller pinhole. This would reduce the signal by a factor of $(14.2/11.4)^2 \approx 1.6$, similar to what was observed.

V Scaffold

Figure 7.9a shows the radiograph recorded on the first layer of film from shot 74180 using a V scaffold. Similar to before, lineouts across the radiograph and corresponding IP (Fig. 7.5a) of the central unattenuated region (green lines) and across the ramp (black lines) are shown in Fig. 7.9c. As in Fig 7.7c, dashed lines correspond to the film and solid lines correspond to the image plate. A similar bell-shaped curve appears in the unattenuated lineouts, but is more smoothly varying and symmetric than in the CH radiograph. This

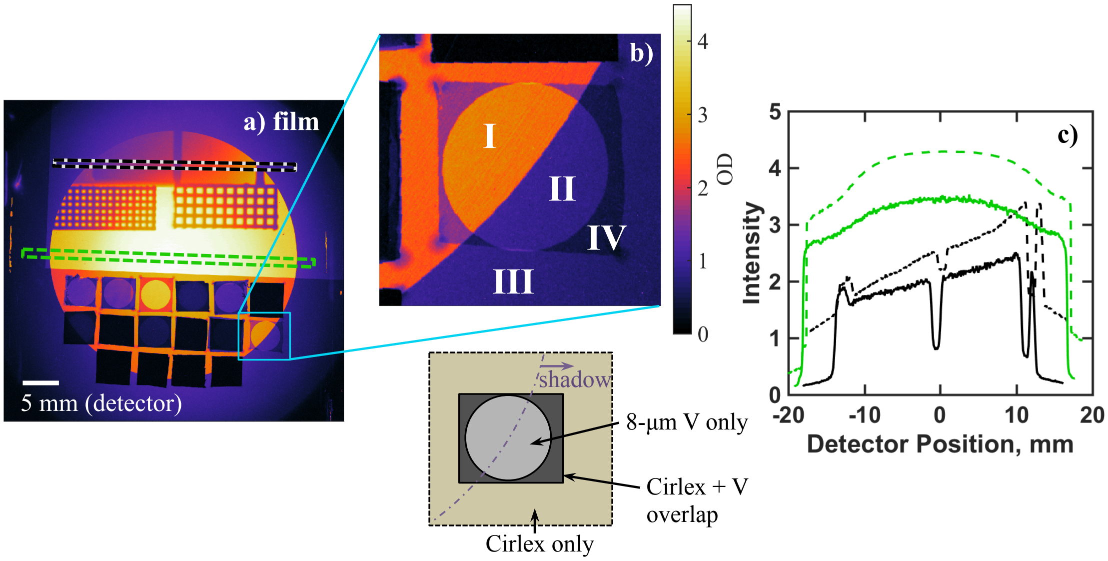

Figure 7.9: a) Radiograph from shot 74180 the V scaffold recorded on the first layer of film. b) Zoom-in on region in radiograph near the edge of the aperture's shadow, focusing on the shadow of the V filter overlapped with the Cirlex filter holder. The diagram underneath describes this overlap. c) Lineouts across the radiograph and corresponding IP of the central unattenuated region (green lines) and across the acrylic fiducial ramp (black lines). As in Fig 7.7, dashed lines correspond to the film and solid lines correspond to the image plate.

feature was reproduced in the other V scaffold target, shot 74188 and is seen on both the film and image plate.

There are several features of this non-uniformity that are consistent with it originating from an extended source of soft x-rays. These x-rays were likely emitted by the V plasma as it expanded unabated beyond the edge of the pinhole substrate, which is depicted in Fig. 7.6 by the blue extended source and dashed arrows. In the radiograph, we see very clearly the outlines of several spectral filters and that of the Cirlex®filter holder in the aperture's shadow. Significant exposure is present at distances $\gg$ 6 mm from the beginning of this shadow (almost up to the detector's edge), which could only originate from x-ray emission in the source plane that extended beyond the edge of the pinhole substrate. This observation rules out that a significant portion of the additional source of x-rays originated from fluorescence in the V discriminator filter. Figure 7.9b shows a close-up of filter 10 of 8-μm thick V, which lies partially in the aperture's shadow. The regions labeled II and IV consist of solely the V and the V + Cirlex®, respectively. The signal ratio between the two is 0.544 ± 0.023, which matched an expected transmission of 0.53 for 5.18 keV He-α x-rays through the 178-μm Cirlex®. In addition, the ratio between signals in regions II and III (Cirlex only) is consistent with 5.18 keV x-rays transmitting through solely the V filter.

The bell-shape of the nonuniformity is similar to that produced by an annular extended source from emission around the pinhole substrate which is then projected through the diagnostic aperture. Several other features in the image are consistent with this suggested origin, such as the ramp profile and signal behind the tungsten wires on the ramp. Ray-tracing shows that the additional source of x-rays does not pass through the resolution target, and would simply contribute an overall background, in addition to hard x-rays. A similar extended source has similarly been reported in [41]. The authors used a significantly smaller pinhole substrate, in which case the extended source was able to cast an additional shadow of the target. In the work reported here, since the nonuniformity/extended source does not appear when using pinhole imagers with CH and Al scaffolds, we conclude that the low-Z plasma formed in the latter two cases effectively tamps lateral expansion of the V microdot plasma.

7.2.3 Reconstruction of X-ray Spectra

For each channel, the recorded signal is taken to be the average over a detector region of $\sim 50 \times 50$ pixels. The recorded signal, y_i on the IP or film of the i^{th} channel can be modeled as

$$y_i = \hat{y}_i + \epsilon_i \tag{7.2}$$

where $\hat{y}_i$ is the expected signal from an incident spectrum, $S(E)$,

$$\hat{y}_i = \int_{E_{min}}^{E_{max}} R_i(E)S(E)\mathrm{d}E, \tag{7.3}$$

$R_i(E)$ is the detector response and ϵ_i is noise, which we can expect to be normally-distributed when the number of photons/pixel is sufficiently large. In general, we can assume that $S(E)$ lies in the space $L^2(E_{min}, E_{max})$ of functions that are square-integrable over the interval, $[E_{min}, E_{max}]$. Then we can write the spectrum as a sum of basis functions, $h_b(E)$ that span $L^2(E_{min}, E_{max})$,

$$S(E) = \sum_{b}^{\infty} c_b h_b(E), \tag{7.4}$$

which gives,

$$\hat{y}_i = \int_{E_{min}}^{E_{max}} R_i(E) \sum_{b}^{\infty} c_b h_b(E) dE.$$

To reconstruct the spectrum, we can then estimate the coefficients, c_b by minimizing the weighted L^2-norm of the error, $\|\boldsymbol{\epsilon}\|_{\mathbf{W}_y^{1/2}} = \|\mathbf{y} - \hat{\mathbf{y}}\|_{\mathbf{W}_y^{1/2}}$ between the N_d measurements, $\mathbf{y}$ and the expected values, $\hat{\mathbf{y}}$. Here, the weighting matrix, $\mathbf{W}_y = \mathbf{S}_y^{-1}$ is the inverse of the measurement covariance matrix, $\mathbf{S}_y$, whose diagonal elements, $\sigma_{y,ii}^2$ are taken as the standard deviation of signal over each channel. In reality, the finite number of data, (dimensionality of $\mathbf{y}$) requires that we truncate the number of basis functions to $N_b < \infty$, which span the subspace, H.

$$\begin{aligned} \hat{y}_i &\approx \int_{E_{min}}^{E_{max}} R_i(E) \sum_{b}^{N_b} c_b h_b(E) dE \\ &= \sum_{b}^{N_b} c_b \int_{E_{min}}^{E_{max}} R_i(E) h_b(E) dE \qquad (7.5) \\ &= \mathbf{c} \cdot \mathbf{g}_i \qquad (7.6) \end{aligned}$$

where $\mathbf{c} = \{c_1, c_2, ..., c_{N_b}\}$ and $g_{ib} = \int_{E_{min}}^{E_{max}} R_i(E) h_b(E) dE$. The data vector of measurements, $\mathbf{y}$ can be written as a matrix equation:

$$\mathbf{y} = \mathbf{G}\,\mathbf{c} + \boldsymbol{\epsilon}, \qquad (7.7)$$

where $\mathbf{g}_i$ are the rows of the $N_d \times N_b$ system matrix, $\mathbf{G}$. The weighted least-squares solution is

$$\hat{\mathbf{c}} = \mathbf{A}\,\mathbf{y} \qquad (7.8)$$

where $\mathbf{A} = (\mathbf{G}^\top \mathbf{W}_y \mathbf{G})^{-1} \mathbf{G}^\top \mathbf{W}_y$. The covariance matrix of the coefficients, $\mathbf{S}_c$ is calculated via

$$\mathbf{S}_c = \mathbf{A}\mathbf{S}_y\mathbf{A}^\top, \tag{7.9}$$

where the diagonal elements, $S_{c,bb}$ are the square of the standard error, σ_b. In practice, we apply a non-negativity constraint to ensure that the reconstructed spectral bins have physically-relevant values.

To use the Ross pair technique, we construct a differencing matrix, $\mathbf{\Delta}_y$ where a given row,

$$\Delta_y^{ij} = [0 \ldots 0 \;\; \underset{i}{-1} \;\; 0 \ldots 0 \;\; \underset{j}{1} \;\; 0 \ldots 0] \tag{7.10}$$

produces the difference signal, $d_{ij} = \Delta_y^{ij} \cdot \mathbf{y} = y_j - y_i$ between filters i and j comprising a Ross pair. The vector of differences is then $\mathbf{d} = \mathbf{\Delta}_y \mathbf{y}$, with covariance matrix, $\mathbf{S}_d = \mathbf{\Delta}_y \mathbf{S}_y \mathbf{\Delta}_y^\top$. The system matrix becomes $\mathbf{D} = \mathbf{\Delta}_y \mathbf{G}$, and weighted least-squares estimate is $\hat{\mathbf{c}}_{RP} = \mathbf{A}_{RP}\mathbf{d}$, where $\mathbf{A}_{RP} = (\mathbf{D}^\top \mathbf{W}_d \mathbf{D})^{-1} \mathbf{D}^\top \mathbf{W}_d$, and $\mathbf{W}_d = \mathbf{S}_d^{-1}$. In this description, the difference signal model accounts for contributions not just from the nominal energy band between the Ross pair's K-edges, but from the wings outside as well.

We choose the basis functions, $h_b(E)$ to be rectangular functions whose edges are defined by the K-edges of the filter materials because these are dominant features that introduce independence between channels. We also choose $E_{\text{min}} = 1.5$ keV and $E_{\text{max}} = 80.7$) keV knowing negligible numbers of x-rays with energies outside this range are detected, given the amount of attenuation for low-energy x-rays and that the hot electron temperatures are expected to be $\lesssim 20$ keV.

Given these basis functions, we can now compare the quality of reconstruction between the individual-channel and Ross pair techniques by determining their sensitivity to noise in the data. In both cases, we are solving the equation, $\mathbf{b} = \mathbf{H}\,\mathbf{c}$ for coefficients, $\mathbf{c}$, given system matrix, $\mathbf{H}$ and data, $\mathbf{b}$. For each model, sensitivity of $\mathbf{c}$ to noise in $\mathbf{b}$ can be measured in terms of the system matrix's condition number, $\text{cond}(\mathbf{H})$. Table 7.2 provides a comparison of condition numbers between the individual-channel ($\mathbf{H} \equiv \mathbf{G}$) and Ross-pair ($\mathbf{H} \equiv \boldsymbol{\Delta}_y\mathbf{G}$) systems. In the first column, only signals recorded on the image plate were included in the reconstruction, whereas in the second column, only signals recorded on the film were used. In the third column, signals from both the image plate and film were used in combination. In all three cases, we see that the condition number of the individual-channel system matrix is several (up to 12) orders of magnitude lower than that of the corresponding Ross-pair system matrix, due to fewer channels being used by pairing. In addition, the data covariances (and hence bin covariances) increase substantially as a result of subtracting channels. Therefore we conclude that for the current filter setup, *using individual channels offers an improvement over the Ross pair technique.* Comparing the columns of Table 7.2, we see that condition number is lowest when combining the image plate and film channels in the reconstruction. Absolute values of the corresponding covariance matrices, $\mathbf{S}_c$ of the coefficients are shown in Fig. 7.10, where bins are ordered in energy; bin 1 is (1.5,4.97) keV and bin 9 is (67.41,80.72) keV. Large covariances are present at low energy for the image plate channel-only system and at high energy for the film channel-only system, resulting from the shapes of the sensitivity curves of

Table 7.2: Condition numbers of the systems matrices used in the reconstruction of x-ray spectra.

System	$\text{cond}(\mathbf{H}_{\text{IP}})$	$\text{cond}(\mathbf{H}_{\text{f}})$	$\text{cond}(\mathbf{H}_{\text{tot}})$
Individual, ($\mathbf{H} \equiv \mathbf{G}$)	7×10^4	900	129
Ross Pairs, ($\mathbf{H} \equiv \boldsymbol{\Delta}_y\mathbf{G}$)	1.7×10^{16}	9×10^{16}	9.5×10^4

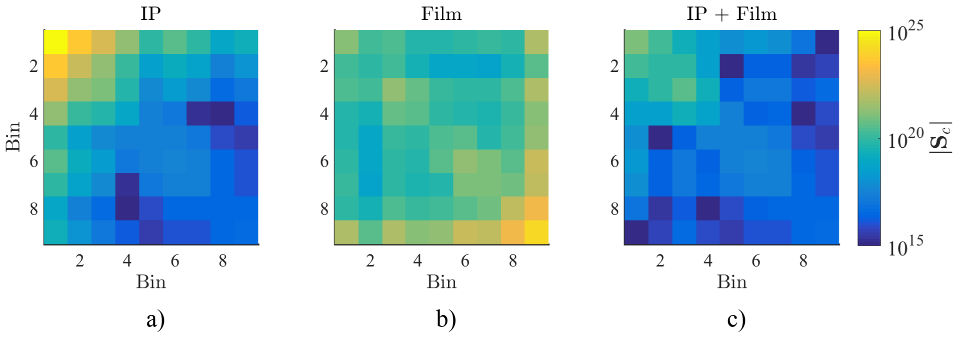

Figure 7.10: Absolute values of covariances matrices, $\mathbf{S}_c$ of coefficients, c_b for individual-channel reconstruction using channels of a) IPs only, b) film only and c) both IP and film. Standard errors of the signals data were taken from shot 74188 to calculate $\mathbf{S}_y$ for each detector.

either detector. Combining the image plate and film channels results in a system with overall significantly reduced coefficient covariances (as much as 10 orders of magnitude reduction).

The non-uniformities discussed previously can introduce significant errors in the reconstructed x-ray spectra. While not completely avoidable, we took several steps to minimize these errors. For instance, in the case where a significant signal gradient was observed across a channel, the signal average was preferentially weighted towards the high-signal side. In some cases, select channels were removed altogether from the data set used in the reconstruction. For instance, channels 5 and 10 at the extremities of the image were removed from most shots without much loss of spectral information as they were repeats of channels 13 and 14. Many of the low-energy channels in the Al scaffold, shot 74176 were removed. We also note that the high-energy channels were insensitive to non-uniformities in the low-energy x-ray signal.

Using the individual channel system, spectra are reconstructed for each shot and shown in 7.11a-b, divided by the laser energy, where the colors and line style are the same as those for Fig. 7.5b. Error bars represent the standard error from the covariance matrices as discussed above. In a) only image-plate channels were used, whereas in b)

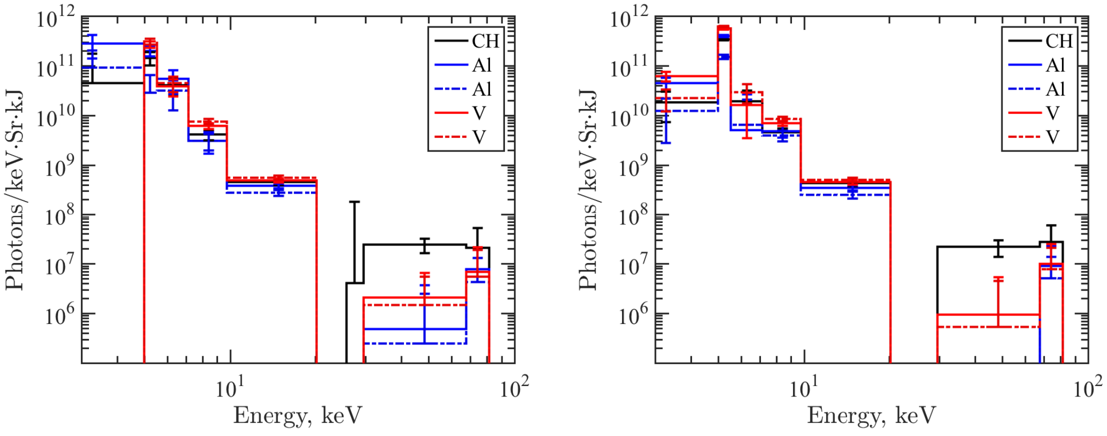

a) b)

Figure 7.11: Reconstructed spectra from the filters in the radiograph plane. Colors and line style (solid/dashed) correspond to the lineouts in Fig. 7.5b. a) Reconstruction from individual channels using image plate signals only. b) Reconstruction from individual channels utilizing signals from both the image plate and film.

both image plate and film channels were used. Comparing a) and b) we see that combining detectors primarily improves the fidelity for the 1.5 - 4.97 keV bin and the 4.97 - 5.46 keV bin, which includes the V He-α line at 5.18 keV.

Hard x-rays in the range 30–70 keV decrease by a factor of > 25 when switching from a CH to Al or V scaffold, consistent with the mitigation of LPIs and their consequent hot electrons going to higher Z. For V, somewhat softer x-rays between 7–25 keV increase by 25–100$\%$, likely from increased thermal bremsstrahlung emission at higher Z. In addition, we see that the number of x-rays in the 4.97 - 5.46 keV bin is about 50$\%$ larger for the V scaffolds compared to the CH scaffold and the Al scaffold shot 74176 (solid blue line), due to the extended source that emits x-rays beyond the edge the pinhole substrate. The other Al scaffold shot, 74181 had over a factor of 2 fewer x-rays in this bin.

7.2.4 Signal-to-background ratio

We now use our above results to calculate signal-to-background ratios (SBs), to understand improvements in image plate-based radiography using the different scaffold designs.

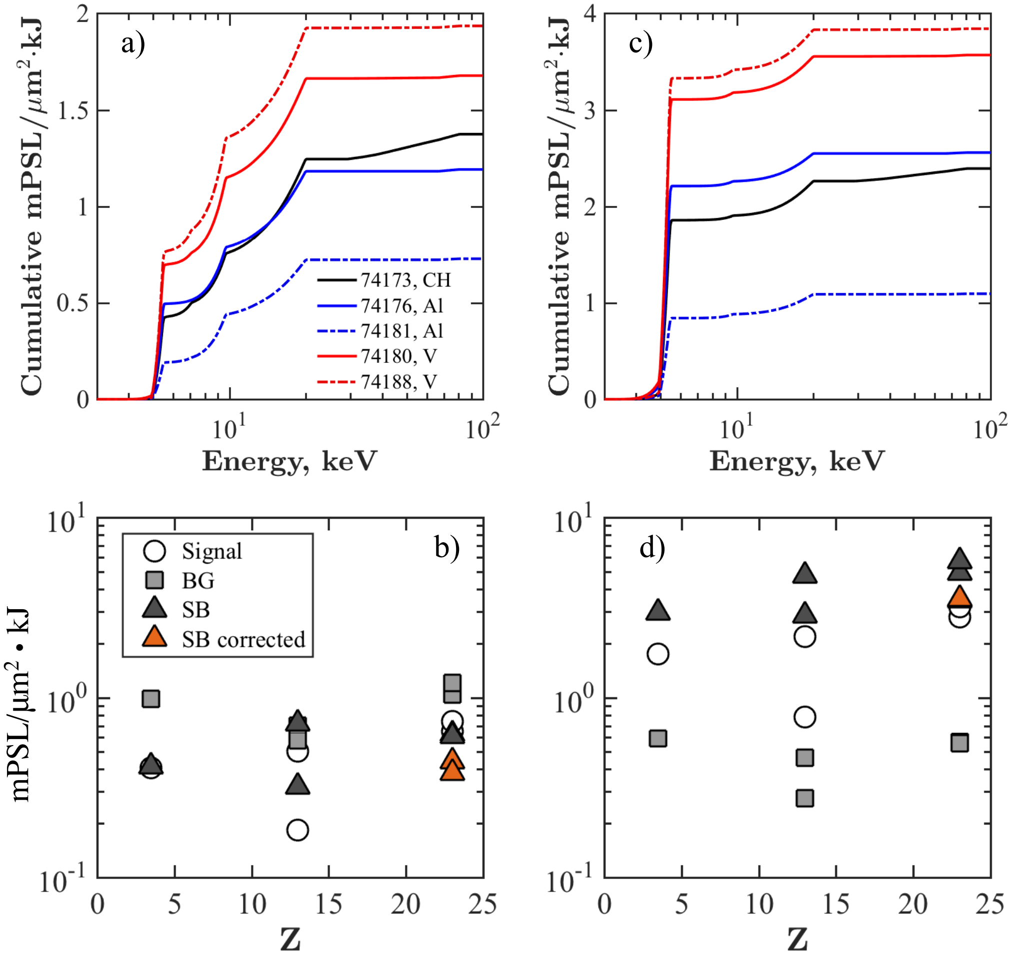

Figure 7.12: a) Inferred cumulative intensity distributions on the image plate from the reconstructed spectra for setup A, the current experiment. b) Signal and background on the image plate in units of mPSL/μm^2·kJ and the dimensionless signal-to-background ratio (SB) vs. scaffold atomic number, Z. The corresponding plots for setup B with a 30-μm V discriminator filter and no film are shown in c) and d).

With the reconstructed energy spectra, we can estimate how x-rays of different energies contribute to the total unattenuated intensity on the image plate. We calculate the total intensity on the image plate, $y_{\text{tot}}(E)$ contributed by x-rays up to energy, E,

$$y_{\text{tot}}(E) = \int_{E_{\text{min}}}^{E} K(E')T_0(E')S(E')\mathrm{d}E', \tag{7.11}$$

similar to Eq. 7.3, where $T_0(E')$ is the transmission through the blast shield, the 8-μm V discriminator filter and the 2 layers of film in front of the image plate. The total intensity distributions are shown for each shot in Fig. 7.12a, divided by the laser energy. The initial large increase in intensity comes from the He-α x-rays in the $4.95 - 5.5$ keV bin. We call this the desirable "signal." All intensity increases beyond 5.5 keV we refer to as the "background." For all shots, we infer that the majority of the background arises from x-rays with energies between 5.5 and 20 keV. These x-rays likely originate from thermal bremsstrahlung emission within the hot coronal plasmas, and contribute much more background than do harder x-rays–especially in the case of Al and V. This thermal background is largest for V, as expected since bremsstrahlung scales as $\langle Z\rangle^2$. However, the hard x-rays with energies $\gtrsim$30 keV present using the CH scaffold (likely from LPI-generated hot electrons) contribute a background that is about 30$\%$ of the He-α signal alone. The background signal from energies between 5.5 and 20 keV from the CH scaffold is larger than that from both of the higher-Z Al scaffolds, indicating there may be some hot electron-generated hard x-rays in this energy range.

The signal, background and SB are shown in Fig. 7.12b vs. scaffold Z as the circles, squares and triangles, respectively. The SB improves from 4:10 for CH to ∼7:10 and ∼6:10 for Al and V, respectively. However, we note that for V, the SB may really be lower than what is shown since some of the signal came from the extended emission around the pinhole substrate that doesn't pass through the object. We can approximate the *direct* signal contribution from the pinhole for V as the average of that estimated for CH and Al (excluding the Al shot, 74181 showing much less signal. We remind the reader that lower signal is consistent with the pinhole being smaller for this shot, in which case the SB is not directly comparable to the other data.) In a future design we presume to eliminate the extended source of background with a collimating structure rather than with plasma from a low-Z scaffold. We calculate a worst-case corrected SB for V using the above approximation of direct pinhole signal, assuming only the He-α x-rays from the extended source are eliminated through collimation. This is shown as the orange triangles, which are about equal to the SB seen for CH as a result of the large thermal bremsstrahlung component. However, eliminating the extended source may also eliminate some of the background from this thermal component, resulting in a SB somewhere between 4:10 and 6:10 for V.

7.2.5 Future design of backlit pinhole imagers

We can improve the design of image plate-based radiography for future experiments with the information provided by the spectral measurements presented in Sec 7.2.3. We propose using a thicker, 30-μm V discriminator filter and removing the film, which gives a total transmission (including blast shield) shown by the blue curve in Fig. 7.13. The orange curve is the transmission of the proposed setup relative to that for the current experiments. These changes result in a factor of 4 higher throughput of the He-α x-rays while decreasing the throughput of thermal bremsstrahlung x-rays with energy between 5.5 to 10 keV by a factor of 3 to 100. Figure 7.12c shows estimates of the total intensity distributions for this proposed setup, indicating that background from 5.5 - 20 keV x-rays may be reduced by over a factor of 2, while hard x-rays are essentially unaffected by the change. Fluorescence in this filter contributes additional signal no more than $\sim 4\%$ of that

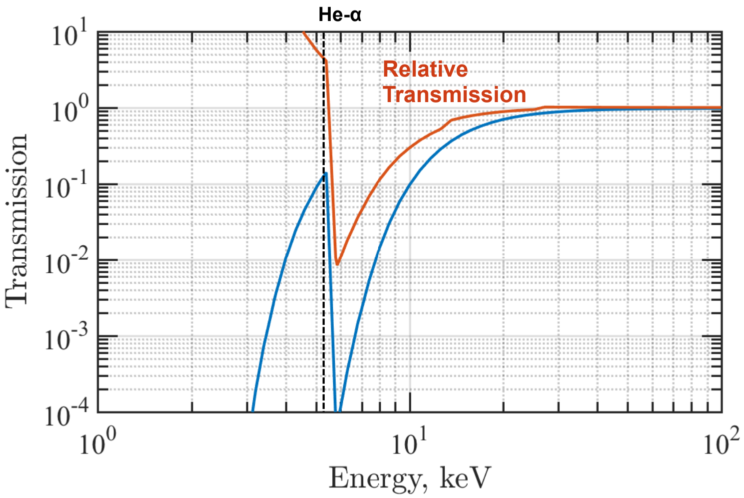

Figure 7.13: Transmission (blue) of proposed radiography setup with 30 μm of V and no film and the transmission relative (orange) to that used in these experiments.

from incident x-rays. Data in Fig. 7.12d presents calculations of signal, total background and SB for this new setup, showing seven-fold increase in SB overall relative to that for the current experiments. Again, the SB increases by 50% from 3:1 for CH to 4.5:1 for Al.

Figure 7.14 shows two designs of backlit pinhole imagers for future experiments, along with the filtering setup proposed above for image plate-based radiography. In both designs, the pinhole substrate may be Ta or higher-Z, with dimensions 7 mm-square by 50 μm-thick. According to results from Ch. 3, a thicker substrate (e.g. 75 μm) may further improve signal-to-background by more efficiently attenuating the thermal bremsstrahlung x-rays that don't pass directly through the pinhole. The top design is similar to the common CH-scaffold design, but uses a transparent quartz or glass (SiO_2) scaffold $\sim$20-μm thick that we expect to mitigate hard x-ray background and avoid microdot misalignment issues. The beryllium blast shield should be made thick enough to significantly attenuate the 1.8 keV Si He-α x-rays that may still transmit through the scaffold. The bottom design is similar to the V-scaffold design reported on in this chapter, except that the V foil is now supported by an acrylic cone that collimates its blow-off plasma, inhibiting expansion beyond the edge of the pinhole substrate. This type of cone has been successfully

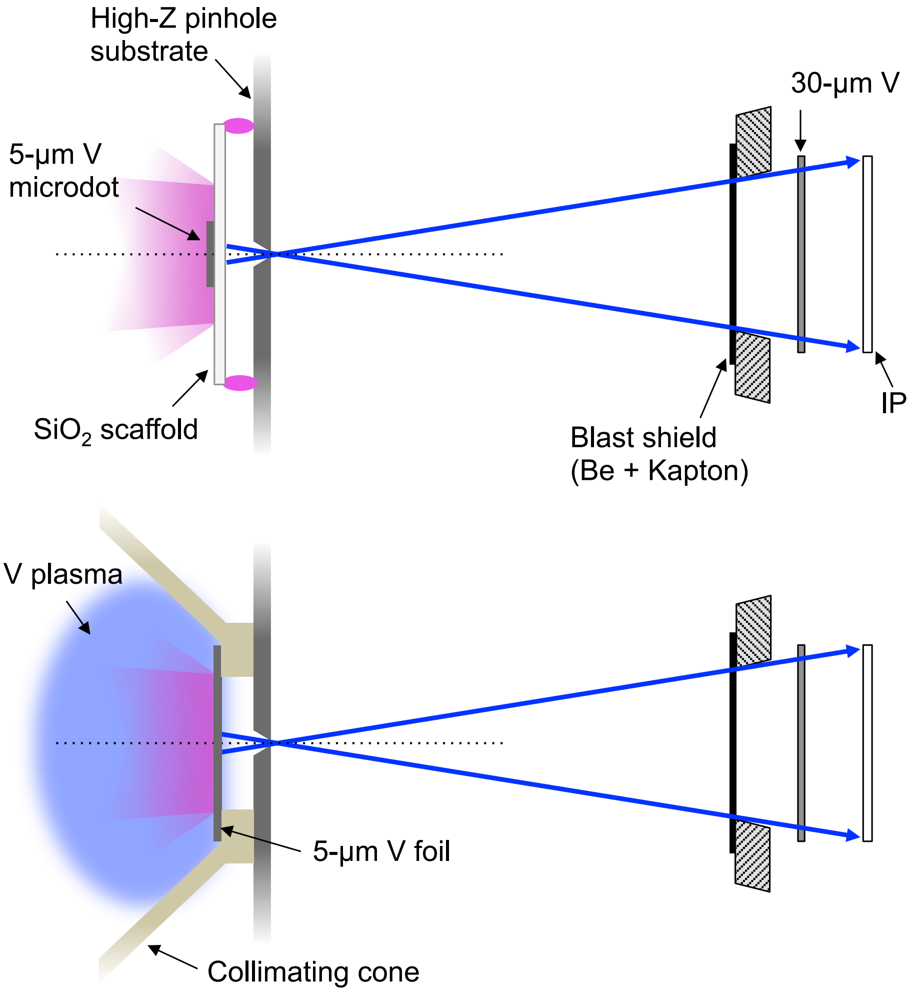

Figure 7.14: Proposed designs of future backlit pinhole imagers. Top: design using a transparent SiO_2 scaffold and V microdot. Bottom: design using a V foil embedded in a collimating cone that is symmetric about the horizontal axis.

applied to x-ray sources used in diffraction measurements of dynamic materials experiments [136]. Alternatively, a larger pinhole substrate may be used. In all cases, one can optimize between spatial resolution and photon statistics by altering the pinhole size and adding kapton filtering between the blast-shield and image plate.

7.3 Conclusions

In this chapter, we demonstrated that the hard x-ray background present in backlit pinhole imagers could be mitigated by increasing the atomic number of the scaffold material that holds the microdot foil away from the pinhole substrate. Changing the scaffold material from CH to aluminum offered a 50% increase in the signal-to-background ratio. The targets using aluminum scaffolds may have suffered from misalignment of the microdot relative to the pinhole. Replacing the aluminum with a transparent scaffold of similar Z, such as quartz or glass ($\langle Z \rangle = 10$) may avoid this issue and still mitigate hard x-rays. Eliminating the scaffold entirely by means of irradiating a large V foil led to mitigation of hard x-rays, but less improvement in signal-to-background ratio due to an increase in background from thermal bremsstrahlung emission. As well, we observed an additional source of background soft x-rays in these targets consistent with emission from V plasma extending beyond the edges of the pinhole substrate. This extended source should not be an issue for gated detectors but may be avoided in future experiments by using a collimating cone or larger pinhole substrate. The CH and aluminum scaffolds prevented this issue by tamping lateral flow of the V plasma. A proposed setup demonstrates a signal-to-background ratio of up to 4.5:1.

CHAPTER 8

Conclusions and Future Directions

This thesis presented three experiments that were performed at large laser facilities, focused on laser-plasma interaction and radiography using laser-generated x-ray sources to diagnose high-energy-density physics experiments. The overarching theme here was to understand the origin of sources of background in backlit pinhole radiography in order to mitigate them and improve the quality of imaging for future HED experiments. However, much of the work is interesting and valuable independent of solving this specific engineering problem. With these concluding remarks, I provide a brief summary of the findings, as well as broader implications of this work and future directions.

Chapter 3 reported results from experiments studying the hard x-ray background in backlit pinhole imaging. Signal-to-background ratios as low as 1:10 were observed. Mitigating the background entirely had the potential to reduce uncertainty in estimates of optical depth from radiographs by over a factor of 2 for film and a factor of 10 for image plates. The latter is particularly important given the desire to move away from film and toward image plates for x-ray detection. The background on the radiograph increased significantly when using lower-Z pinhole substrates. While these changes were consistent with the x-ray background coming from the pinhole imagers, we did not have enough evidence to determine whether the x-rays were produced primarily in the laser plasma interaction region, or in the pinhole substrate. Estimates of electron ranges in materials suggest the former. These results indicate that future experiments using thicker and higher-Z pinhole substrates can lead to less background on the radiograph. However, the source of hard x-rays must be eliminated entirely to also mitigate the contribution of background that passes through the pinhole.

Chapters 4-6 focused on experiments studying hot electron production from low- to high-Z laser-irradiated planar targets. We inferred from hard x-ray measurements that hot-electron levels decreased by 3 orders of magnitude between low-Z CH and high-Z Au targets, and temperatures decreased by a factor of 2. Measurements of electron density profiles of the expanding plasmas from these targets demonstrated significant steepening as the atomic number of the target increased. These combined observations were consistent with increased intensity thresholds of laser-plasma instabilities in the higher-Z targets. Radiation hydrodynamic simulations presented in Ch. 5 showed systematic over-prediction of density at a given location by up to 40%, relative to measured density profiles. However, they showed overall good agreement in shape and length-scales compared to measurements at densities below $n_c/10$. The low-density agreement helped validate using the simulations to predict conditions at higher densities. The simulations predicted significant increases in electron temperature and overlapped intensities with increasing Z, leading to higher thresholds for multi-beam TPD and multi-beam SRS. The results added to previous evidence indicating that SRS may play a comparable or greater role than TPD in generating hot electron in multi-beam experiments.

Models of LPIs are difficult to validate with solely time-integrated hard x-ray measurements and inferences of hot-electron production. The acceleration of hot electrons occurs primarily in the nonlinear stages of TPD and SRS driven by either single or multiple laser beams. Hence, the hard x-ray measurement data contain little information about the linear growth stages and the original decay waves that are direct signatures of these LPIs. Time-resolved Thomson scattering measurements of common EPW amplitudes as well as measurements of $\omega_0/2$ and $3\omega_0/2$ light and SRS scattered light signatures in future experiments can provide more direct observations of these instabilities. In addition, more comprehensive measurements of plasma conditions can help confirm which physical mechanisms are most important in mitigating the instabilities in mid- to high-Z targets. Zakharov and PIC simulations combined with accurate knowledge of the plasma conditions in these experiments can be used to study the nonlinear evolution of TPD and SRS from the coupling between EPWs and IAWs, as well as the acceleration of hot electrons in the EPWs' potentials.

The refraction images presented in Ch. 4 may be used in the future to understand details of ablation dynamics in laser-produced plasmas, aside from their application in understanding LPIs in this thesis. These measurements are particularly useful to study the plasma corona at densities below $\sim 9 \times 10^{20}$ cm^{-3}. However a measurement system with a shorter probe wavelength and/or larger-diameter collection optic is required to observe the profile closer to n_c where gradients are especially steep. X-ray interferometry techniques [137, 138] may be used to image these plasmas at higher density in future experiments, and can be used in concert with our low-density measurements to provide a more complete picture of the plasma profile. Detailed measurements of the profiles can help validate models of nonlocal electron heat transport and non-LTE atomic physics that are used in radiation hydrodynamic simulations. Validation of this kind is highly valuable to improve modeling of full-scale direct and indirect drive ICF targets.

The measurements from the OMEGA-EP experiments increase the parameter space over which hot-electron production has been quantified. This is in general useful to predict the importance of hot electrons in more complicated experiments with similar laser parameters and irradiated materials. In addition, they add to the evidence demonstrating that low-Z irradiated materials can be replaced with higher-Z ones where acceptable to reduce hot electrons that cannot be tolerated experimentally. Past experiments studying unstable HED flows have typically had design constraints from hot-electron preheat. For instance, the laser irradiance had been limited to $\sim 10^{14}$ W/cm^2 [139] when using low-Z plastic ablators. Our observations and others of mitigated hot-electron production suggest that this upper limit may be increased in future experiments by increasing the effective Z of the ablator. Higher irradiances would enable access to new flow regimes. However, designs must optimize over reduced hot-electron production, additional x-ray preheat and reduced ablation pressures going to higher Z. Inserting an additional thin high-Z layer between the ablator and target package may mitigate the x-ray preheat [139].

Chapter 7 presented experiments on the OMEGA-60 laser demonstrating that the hard x-ray background present in backlit pinhole imagers could be mitigated by increasing the atomic number of the scaffold material that holds the microdot foil away from the pinhole substrate. Spectral measurements showed that hard x-rays with energy $\gtrsim$30 keV were significantly reduced in both the Al- and V-scaffold designs relative to the common CH-scaffold design. This change led to a greater than 50% improvement in the signal-to-background ratio in the case of Al. The improvements with the V-scaffold design were less clear due to the presence of emission from the V plasma that had expanded beyond the edge of the pinhole substrate. In all cases, the background from the thermal emission was estimated to be significantly larger than that from the harder x-rays that were presumably generated by hot electrons. New designs of backlit pinhole imagers and filtering setups may offer signal-to-background ratios of greater than 4:1 using image plate-based radiography.

APPENDIX A

AFR Data From August 2014 Shot Day

The full set of angular filter refractomery images using the "AF3" angular filter are shown in Fig. A.1 from the experiments presented in Ch. 4. All images are fairly symmetric across the y-axis, consistent with our assumption of azimuthally symmetry electron density profiles. The contours closer to the target surface are highly discontinuous across the image in nearly all targets. The breaks in the contours correlate with filamentary structures observed in shadowgraphs that align closely with the beam direction. The density gradients that led to these structures may have occurred from either filamentation instabilities or local intensity hot spots in the beam profile [140–142].

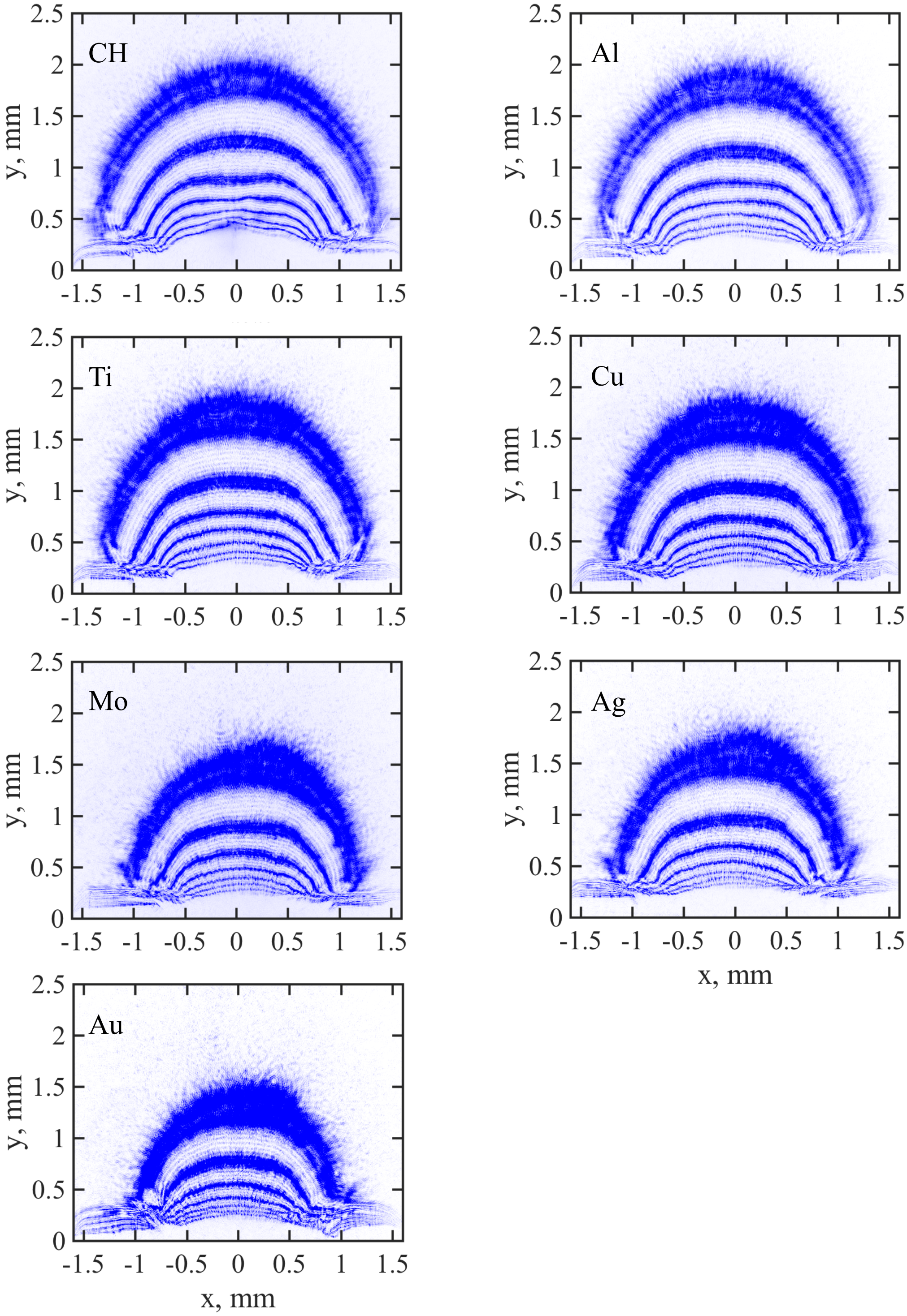

Figure A.1: Angular filter refractometry images for all targets in the experiments presented in Ch. 4.

BIBLIOGRAPHY

[1] Hansen, J. F., Robey, H. F., Klein, R. I., and Miles, A. R., "Experiment on the mass-stripping of an interstellar cloud in a high Mach number post-shock flow," *Phys. Plasmas*, Vol. 14, No. 5, 2007, pp. 056505.

[2] Brown, D. B., Criss, J. W., and Birks, L. S., "Sensitivity of x-ray films. I. A model for sensitivity in the 1 - 100-keV region," *J. Appl. Phys.*, Vol. 47, No. 8, 1976, pp. 3722.

[3] Haberberger, D., Ivancic, S., Hu, S. X., Boni, R., Barczys, M., Craxton, R. S., and Froula, D. H., "Measurements of electron density profiles using an angular filter refractometera)," *Phys. Plasmas*, Vol. 21, No. 5, may 2014, pp. 056304.

[4] Basov, N. G. and Krokhin, O. N., "Conditions for heating up of a plasma by the radiation from an optical generator," *Sov. Phys. JETP Lett.*, Vol. 19, No. 1, 1964, pp. 123–125.

[5] Dawson, J. M., "On the Production of Plasma by Giant Pulse Lasers," *Phys. Fluids*, Vol. 7, No. 7, 1964, pp. 981.

[6] Shkarofsky, I P, Johnston, T W, Bachynski, M. P., *The Particle Kinetics of Plasmas*, Addison-Wesley Pub. Co., 1st ed., 1966.

[7] Ginzburg, V., "The properties of electrmagnetic waves in plasmas," *Pergamon*, 1964.

[8] Atzeni, S. and Meyer-ter Vehn, J., *The Physics of Inertial Fusion : BeamPlasma Interaction, Hydrodynamics, Hot Dense Matter*, Clarendon Press, Oxford, 2004.

[9] Fabbro, R, Max, C, Fabre, E., "Planar laser-driven ablation : Effect of inhibited electron thermal conduction," *Phys. Fluids*, Vol. 28, No. 5, 1985, pp. 1463 – 1481.

[10] Lindl, J. D., *Inertial Confinement Fusion: The Quest for Ignition and Energy Gain Using Indirect Drive*, Springer-Verlag, New York, 1998.

[11] Hwang, U., Flanagan, K. A., and Petre, R., "Chandra X-Ray Observation of a Mature Cloud-Shock Interaction in the Bright Eastern Knot Region of Puppis A," *Astrophys. J.*, Vol. 635, No. 1, 2005, pp. 355–364.

[12] Robey, H. F., Kane, J. O., Remington, B. A., Drake, R. P., Hurricane, O. A., Louis, H., Wallace, R. J., Knauer, J., Keiter, P., Arnett, D., and Ryutov, D. D., "An experimental testbed for the study of hydrodynamic issues in supernovae," *Phys. Plasmas*, Vol. 8, No. 5 II, 2001, pp. 2446–2453.

[13] Kuranz, C. C., Drake, R. P., Grosskopf, M. J., Fryxell, B., Budde, A., Hansen, J. F., Miles, A. R., Plewa, T., Hearn, N., and Knauer, J., "Spike morphology in blast-wave-driven instability experiments," *Phys. Plasmas*, Vol. 17, 2010, p. 052709.

[14] Krauland, C. M., Drake, R. P., Kuranz, C. C., Sweeney, R., Grosskopf, M., Klein, S., Gillespie, R., Keiter, P. A., Loupias, B., and Falize, E., "Radiative reverse shock laser experiments relevant to accretion processes in cataclysmic variables," *Phys. Plasmas*, Vol. 20, No. 5, 2013, pp. 056502.

[15] Matthews, D. L., Campbell, E. M., Ceglio, N. M., Hermes, G., Kauffman, A., Koppel, L., Lee, A., Manes, K., Rupert, V., Slivinsky, V. W., Turner, R., and Ze, F., "Characterization of laser-produced plasma x-ray sources for use in x-ray radiography," *J. Appl. Phys.*, Vol. 54, No. 8, 1983, pp. 4260–4268.

[16] Workman, J. and Kyrala, G. A., "X-ray yield scaling studies performed on the OMEGA laser," *Rev. Sci. Instrum.*, Vol. 72, No. 1, 2001, pp. 678.

[17] Barrios, M. A., Fournier, K. B., Regan, S. P., Landen, O., May, M., Opachich, Y. P., Widmann, K., Bradley, D. K., and Collins, G. W., "High Energy Density Physics Backlighter development at the National Ignition Facility (NIF): Zinc to zirconium," *High Energy Density Phys.*, Vol. 9, 2013, pp. 626–634.

[18] Barrios, M. A., Regan, S. P., Fournier, K. B., Epstein, R., Smith, R., Lazicki, A., Rygg, R., Fratanduono, D. E., Eggert, J., Park, H. S., Huntington, C., Bradley, D. K., Landen, O. L., and Collins, G. W., "X-ray area backlighter development at the national ignition facility (invited)," *Rev. Sci. Instrum.*, Vol. 85, No. 11, 2014, pp. 0–6.

[19] Salzmann, D., *Atomic physics in hot plasmas*, Oxford University Press, New York, 1998.

[20] Glendinning, S. G., Weber, S. V., Bell, P., DaSilva, L. B., Dixit, S. N., Henesian, M. A., Kania, D. R., Kilkenny, J. D., Powell, H. T., Wallace, R. J., Wegner, P. J., Knauer, J. P., and Verdon, C. P., "Laser-driven planar Rayleigh-Taylor instability experiments," *Phys. Rev. Lett.*, Vol. 69, No. 8, 1992, pp. 1201–1204.

[21] Robey, H. F., Perry, T. S., Klein, R. I., Kane, J. O., Greenough, J. A., and Boehly, T. R., "Experimental investigation of the three-dimensional interaction of a strong shock with a spherical density inhomogeneity," *Phys. Rev. Lett.*, Vol. 89, No. 8, 2002, pp. 085001/1–085001/4.

[22] Foster, J. M., Wilde, B. H., Rosen, P. A., Perry, T. S., Fell, M., Edwards, M. J., Lasinski, B. F., Turner, R. E., and Gittings, M. L., "Supersonic jet and shock interactions," *Phys. Plasmas*, Vol. 9, No. 5, 2002, pp. 2251–2263.

[23] Doss, F. W., Robey, H. F., Drake, R. P., and Kuranz, C. C., "Wall shocks in high-energy-density shock tube experiments," *Phys. Plasmas*, Vol. 16, No. 11, 2009, pp. 112705.

[24] Smalyuk, V. A., Hansen, J. F., Hurricane, O. A., Langstaff, G., Martinez, D., Park, H.-S., Raman, K., Remington, B. a., Robey, H. F., Schilling, O., Wallace, R., Elbaz, Y., Shimony, A., Shvarts, D., Di Stefano, C., Drake, R. P., Marion, D., Krauland, C. M., and Kuranz, C. C., "Experimental observations of turbulent mixing due to Kelvin - Helmholtz instability on the OMEGA Laser Facility," *Phys. Plasmas*, Vol. 19, No. 9, 2012, pp. 092702.

[25] Park, H. S., Chambers, D. M., Chung, H. K., Clarke, R. J., Eagleton, R., Giraldez, E., Goldsack, T., Heathcote, R., Izumi, N., Key, M. H., King, J. A., Koch, J. A., Landen, O. L., Nikroo, A., Patel, P. K., Price, D. F., Remington, B. A., Robey, H. F., Snavely, R. A., Steinman, D. A., Stephens, R. B., Stoeckl, C., Storm, M., Tabak, M., Theobald, W., Town, R. P. J., Wickersham, J. E., and Zhang, B. B., "High-energy Kα radiography using high-intensity, short-pulse lasers," *Phys. Plasmas*, Vol. 13, No. 5, 2006, pp. 056309.

[26] Brambrink, E., Wei, H. G., Barbrel, B., Audebert, P., Benuzzi-Mounaix, a., Boehly, T., Endo, T., Gregory, C., Kimura, T., Kodama, R., Ozaki, N., Park, H.-S., le Gloahec, M. R., and Koenig, M., "X-ray source studies for radiography of dense matter," *Phys. Plasmas*, Vol. 16, No. 3, 2009, pp. 033101.

[27] Maddox, B. R., Park, H. S., Remington, B. A., Chen, C., Chen, S., Prisbrey, S. T., Comley, A., Back, C. A., Szabo, C., Seely, J. F., Feldman, U., Hudson, L. T., Seltzer, S., Haugh, M. J., and Ali, Z., "Absolute measurements of x-ray backlighter sources at energies above 10 keV," *Phys. Plasmas*, Vol. 18, No. 5, 2011, pp. 056709.

[28] Glendinning, S G, Amendt, P A, Budil, K S, Hammel, B A, Kalantar, D H, Key, M H, Landen, O L , Remington, B A, Desenne, D. E., "Laser plasma diagnostics of dense plasmas," *Proc. SPIE 2523, Appl. Laser Plasma Radiat.*, Vol. 2523, No. 29, 1997, pp. 1–11.

[29] Landen, O. L., Farley, D. R., Glendinning, S. G., Logory, L. M., Bell, P. M., Koch, J. A., Lee, F. D., Bradley, D. K., Kalantar, D. H., Back, C. A., and Turner, R. E., "X-ray backlighting for the National Ignition Facility (invited)," *Rev. Sci. Instrum.*, Vol. 72, No. 1, 2001, pp. 627.

[30] Bradley, D. K., Landen, O. L., Bullock, A. B., Glendinning, S. G., and Turner, R. E., "Efficient, 1-100-keV x-ray radiography with high spatial and temporal resolution." *Opt. Lett.*, Vol. 27, No. 2, 2002, pp. 134–136.

[31] Bullock, A. B., Landen, O. L., and Bradley, D. K., "10 and 5 μm pinhole-assisted point-projection backlit imaging for the National Ignition Facility," *Rev. Sci. Instrum.*, Vol. 72, No. 1, 2001, pp. 690–693.

[32] Blue, B. E., Hansen, J. F., and Robey, H. F., "Improved pinhole-apertured point-projection backlighter geometry," *Rev. Sci. Instrum.*, Vol. 75, No. 10, oct 2004, pp. 3989–3991.

[33] Batha, S. H., Barnes, C. W., and Christensen, C. R., "Backlighter predictive capability," *Rev. Sci. Instrum.*, Vol. 74, No. 3, 2003, pp. 2174.

[34] Bullock, A. B., Landen, O. L., Blue, B. E., Edwards, J., and Bradley, D. K., "X-ray induced pinhole closure in point-projection x-ray radiography," *J. Appl. Phys.*, Vol. 100, No. 4, 2006, pp. 043301.

[35] Flippo, K. A., Kline, J. L., Doss, F. W., Loomis, E. N., Emerich, M., Devolder, B., Murphy, T. J., Fournier, K. B., Kalantar, D. H., Regan, S. P., Barrios, M. A., Merritt, E. C., Perry, T. S., Tregillis, I. L., and Fincke, J. R., "Development of a Big Area BackLighter for high energy density experiments," *Rev. Sci. Instrum.*, Vol. 093501, 2014, pp. 1–8.

[36] Workman, J., Fincke, J. R., Keiter, P. A., Kyrala, G. A., Pierce, T., Sublett, S., Knauer, J. P., Robey, H., Blue, B., Glendinning, S. G., and Landen, O. L., "Development of intense point x-ray sources for backlighting high energy density experiments (invited)," *Rev. Sci. Instrum.*, Vol. 75, No. 10, 2004, pp. 3915.

[37] Workman, J., Fincke, J. R., Kyrala, G. A., and Pierce, T., "Uniform large-area x-ray imaging at 9 keV using a backlit pinhole." *Appl. Opt.*, Vol. 44, No. 6, feb 2005, pp. 859–65.

[38] Kyrala, G. A., Klare, K., and Workman, J., "Optimizing area-backlighter performance in a difficult geometry," *Rev. Sci. …*, Vol. 2182, No. 2003, 2003.

[39] Failor, B. H., Gabl, E. F., Johnson, R. R., and Shepard, C., "Characterization of sub-10-μm 30-ps flash duration point sources for x radiography," *J. Appl. Phys.*, Vol. 66, No. 4, 1989, pp. 1571–1578.

[40] Kuranz, C. C., Blue, B. E., Drake, R. P., Robey, H. F., Hansen, J. F., Knauer, J. P., Grosskopf, M. J., Krauland, C., and Marion, D. C., "Dual, orthogonal, backlit pinhole radiography in OMEGA experiments," *Rev. Sci. Instrum.*, Vol. 77, No. 10, 2006, pp. 10E327.

[41] Huntington, C. M., Krauland, C. M., Kuranz, C. C., Drake, R. P., Park, H.-S., Kalantar, D. H., Maddox, B. R., Remington, B. a., and Kline, J., "Development of a short duration backlit pinhole for radiography on the National Ignition Facility." *Rev. Sci. Instrum.*, Vol. 81, No. 10, oct 2010, pp. 10E536.

[42] Krauland, C. M., Jarrott, L. C., Drake, R. P., Keiter, P. A., Kuranz, C. C., Westover, B., Sawada, H., Kaczala, D. N., and Bonofiglo, P., "An evaluation of high energy bremsstrahlung background in point-projection x-ray radiography experiments." *Rev. Sci. Instrum.*, Vol. 83, No. 10, oct 2012, pp. 10E528.

[43] Workman, J., Lanier, N. E., and Kyrala, G. A., "Analysis of Ti K-shell emission produced from solid targets using nanosecond pulses on the TRIDENT laser facility," *Rev. Sci. Instrum.*, Vol. 74, No. 3, 2003, pp. 2165.

[44] Nuckolls, J., Wood, L., Thiessen, A., and Zimmerman, G., "Laser Compression of Matter to Super-High Densities: Thermonuclear (CTR) Applications," *Nature*, Vol. 239, No. 5368, 1972, pp. 139–142.

[45] Lindl, J., "Development of the indirect-drive approach to inertial confinement fusion and the target physics basis for ignition and gain," *Phys. Plasmas*, Vol. 2, No. 11, 1995, pp. 3933.

[46] Rosen, M. D., "The physics issues that determine inertial confinement fusion target gain and driver requirements: A tutorial," *Phys. Plasmas*, Vol. 6, No. 5, 1999, pp. 1690.

[47] Meyerhofer, D. D., Delettrez, J. a., Epstein, R., Glebov, V. Y., Skupsky, S., Smalyuk, V. a., Sorce, C., Stoeckl, C., Soures, J. M., Fletcher, K., Padalino, S., Freeman, C., Izumi, N., Lerche, R. a., Phillips, T. W., and Sangster, T. C., "Inferences of mix in direct-drive spherical implosions with high uniformity F H S ," *New York*, Vol. 43, 2001, pp. 277–286.

[48] Shiau, J. N., Goldman, E. B., and Weng, C. I., "Linear stability analysis of laser-driven spherical implosions," *Phys. Rev. Lett.*, Vol. 32, No. 7, 1974, pp. 352–355.

[49] Craxton, R. S., Anderson, K. S., Boehly, T. R., Goncharov, V. N., Harding, D. R., Knauer, J. P., McCrory, R. L., McKenty, P. W., Meyerhofer, D. D., Myatt, J. F., Schmitt, A. J., Sethian, J. D., Short, R. W., Skupsky, S., Theobald, W., Kruer, W. L., Tanaka, K., Betti, R., Collins, T. J. B., Delettrez, J. A., Hu, S. X., Marozas, J. A., Maximov, A. V., Michel, D. T., Radha, P. B., Regan, S. P., Sangster, T. C., Seka, W., Solodov, A. A., Soures, J. M., Stoeckl, C., and Zuegel, J. D., "Direct-drive inertial confinement fusion: A review," *Phys. Plasmas*, Vol. 22, No. 11, 2015.

[50] Lindl, J. D., Amendt, P., Berger, R. L., Glendinning, S. G., Glenzer, S. H., Haan, S. W., Kauffman, R. L., Landen, O. L., and Suter, L. J., "The physics basis for ignition using indirect-drive targets on the National Ignition Facility," *Phys. Plasmas*, Vol. 11, No. 2, 2004, pp. 339.

[51] Smalyuk, V., Shvarts, D., Betti, R., Delettrez, J., Edgell, D., Glebov, V., Goncharov, V., McCrory, R., Meyerhofer, D., Radha, P., Regan, S., Sangster, T., Seka, W., Skupsky, S., Stoeckl, C., Yaakobi, B., Frenje, J., Li, C., Petrasso, R., and Séguin, F., "Role of Hot-Electron Preheating in the Compression of Direct-Drive Imploding Targets with Cryogenic D2 Ablators," *Phys. Rev. Lett.*, Vol. 100, No. 18, may 2008, pp. 185005.

[52] Robey, H. F., Celliers, P. M., Moody, J. D., Sater, J., Parham, T., Kozioziemski, B., Dylla-Spears, R., Ross, J. S., LePape, S., Ralph, J. E., Hohenberger, M., Dewald, E. L., Berzak Hopkins, L., Kroll, J. J., Yoxall, B. E., Hamza, A. V., Boehly, T. R., Nikroo, A., Landen, O. L., and Edwards, M. J., "Shock timing measurements and analysis in deuterium-tritium-ice layered capsule implosions on NIF," *Phys. Plasmas*, Vol. 21, No. 2, feb 2014, pp. 022703.

[53] Yaakobi, B., Pelah, I., and Hoose, J., "Preheat by fast electrons in laser-fusion experiments," *Phys. Rev. Lett.*, Vol. 37, No. 13, 1976, pp. 836–839.

[54] Rousseaux, C., Amiranoff, F., Labaune, C., and Matthieussent, G., "Suprathermal and relativistic electrons produced in laser-plasma interaction at 0.26, 0.53, and 1.05 μm laser wavelength," *Phys. Fluids B Plasma Phys.*, Vol. 4, No. 8, 1992, pp. 2589.

[55] Yan, R., Ren, C., Li, J., Maximov, A. V., Mori, W. B., Sheng, Z.-M., and Tsung, F. S., "Generating energetic electrons through staged acceleration in the two-plasmon-decay instability in inertial confinement fusion," *Phys. Rev. Lett.*, Vol. 108, No. 17, apr 2012, pp. 175002.

[56] Ebrahim, N., Baldis, H., Joshi, C., and Benesch, R., "Hot electron generation by the two-plasmon decay instability in the laser-plasma Interaction at 10.6 μm," *Phys. Rev. Lett.*, Vol. 45, No. 14, 1980.

[57] Michel, D. T., Maximov, A. V., Short, R. W., Delettrez, J. A., Edgell, D., Hu, S. X., Igumenshchev, I. V., Myatt, J. F., Solodov, A. A., Stoeckl, C., Yaakobi, B., and Froula, D. H., "Measured hot-electron intensity thresholds quantified by a two-plasmon-decay resonant common-wave gain in various experimental configurations," *Phys. Plasmas*, Vol. 20, No. 5, 2013, pp. 315–318.

[58] Rosen, M. D., "Electron transport and preheat," Tech. rep., Lawrence Livermore National Laboratory, Livermore, CA.

[59] Drake, R. P., *High Energy Density Physics: Fundamentals, Inertial Fusion, and Experimental Astrophysics*, Springer-Verlag, Berlin, 1st ed., 2006.

[60] Smalyuk, V. A., Betti, R., Boehly, T. R., Craxton, R. S., Delettrez, J. A., Edgell, D. H., Glebov, V. Y., Goncharov, V. N., Harding, D. R., Hu, S. X., Knauer, J. P., Marshall, F. J., McCrory, R. L., McKenty, P. W., Meyerhofer, D. D., Radha, P. B., Regan, S. P., Sangster, T. C., Seka, W., Short, R. W., Shvarts, D., Skupsky, S., Soures, J. M., Stoeckl, C., Yaakobi, B., Frenje, J. a., Li, C. K., Petrasso, R. D., and Seguin, F. H., "Cryogenic-target performance and implosion physics studies on OMEGA," *Phys. Plasmas*, Vol. 16, No. 5, 2009, pp. 056301.

[61] Regan, S. P., Meezan, N. B., Suter, L. J., Strozzi, D. J., Kruer, W. L., Meeker, D., Glenzer, S. H., Seka, W., Stoeckl, C., Glebov, V. Y., Sangster, T. C., Meyerhofer, D. D., McCrory, R. L., Williams, E. A., Jones, O. S., Callahan, D. A., Rosen, M. D., Landen, O. L., Sorce, C., and MacGowan, B. J., "Suprathermal electrons generated by the two-plasmon-decay instability in gas-filled Hohlraums," *Phys. Plasmas*, Vol. 17, No. 2, 2010, pp. 020703.

[62] Dewald, E. L., Hartemann, F., Michel, P., Milovich, J., Hohenberger, M., Pak, A., Landen, O. L., Divol, L., Robey, H. F., Hurricane, O. A., Döppner, T., Albert, F., Bachmann, B., Meezan, N. B., Mackinnon, A. J., Callahan, D., and Edwards, M. J., "Generation and Beaming of Early Hot Electrons onto the Capsule in Laser-Driven Ignition Hohlraums," *Phys. Rev. Lett.*, Vol. 116, No. 7, 2016, pp. 1–5.

[63] Kuranz, C. C., Drake, R. P., Dannenberg, K. K., Susalla, P. J., Kremer, D. J., Boehly, T., and Knauer, J., “Preheat issues in hydrodynamic Hedla experiments,” *Astrophys. Space Sci.*, Vol. 298, No. 1-2, 2005, pp. 267–271.

[64] Zhang, Y., Drake, R. P., and Glimm, J., “Numerical evaluation of the impact of laser preheat on interface structure and instability,” *Phys. Plasmas*, Vol. 14, No. 6, 2007, pp. 1–10.

[65] Fein, J. R., Peebles, J. L., Keiter, P. A., Holloway, J. P., Klein, S. R., Kuranz, C. C., Manuel, M. J.-E., and Drake, R. P., “Investigation of the hard x-ray background in backlit pinhole imagersa),” *Rev. Sci. Instrum.*, Vol. 85, No. 11, nov 2014, pp. 11E610.

[66] Fournier, K. B., May, M. J., Colvin, J. D., Kane, J. O., Schneider, M., Dewald, E., Thomas, C. a., Compton, S., Marrs, R. E., Moody, J., Bond, E., Michel, P., Fisher, J. H., Newlander, C. D., and Davis, J. F., “Multi-keV x-ray source development experiments on the National Ignition Facility,” *Phys. Plasmas*, Vol. 17, No. 8, 2010, pp. 082701.

[67] Fein, J. R., Keiter, P. A., Holloway, J. P., Klein, S. R., Davis, J. S., and Drake, R. P., “Mitigation of hard x-ray background in backlit pinhole imagers,” *Rev. Sci. Instrum.*, Vol. 87, No. 11, 2016.

[68] Rosenbluth, M., “Parametric Instabilities in Inhomogeneous Media,” *Phys. Rev. Lett.*, Vol. 29, 1972.

[69] Kruer, W. L., *The Physics of Laser Plasma Interactions*, Westview Press, Boulder, CO, 2nd ed., 2003.

[70] Turner, R. E., Estabrook, K., Kauffman, R. L., Bach, D. R., Drake, R. P., Phillion, D. W., Lasinski, B. F., Campbell, E. M., Kruer, W. L., and Williams, E. A., “Evidence for collisional damping in high-energy Raman-scattering experiments at 0.26 um,” *Phys. Rev. Lett.*, Vol. 54, No. 3, 1985, pp. 189–192.

[71] Fernández, J. C., Cobble, J. A., Failor, B. H., DuBois, D. F., Montgomery, D. S., Rose, H. A., Vu, H. X., Wilde, B. H., Wilke, M. D., and Chrien, R. E., “Observed Dependence of Stimulated Raman Scattering on Ion-Acoustic Damping in Hohlraum Plasmas.” *Phys. Rev. Lett.*, Vol. 77, No. 13, sep 1996, pp. 2702–2705.

[72] Kirkwood, R. K., MacGowan, B. J., Montgomery, D. S., Afeyan, B. B., Kruer, W. L., Moody, J. D., Estabrook, K. G., Back, C. A., Glenzer, S. H., Blain, M. A., Williams, E. A., Berger, R. I., and Lasinski, B. F., “Effect of Ion-Wave Damping on Stimulated Raman Scattering in High-Z Laser-Produced Plasmas.” *Phys. Rev. Lett.*, Vol. 77, No. 13, sep 1996, pp. 2706–2709.

[73] Seka, W., Edgell, D. H., Myatt, J. F., Maximov, A. V., Short, R. W., Goncharov, V. N., and Baldis, H. A., “Two-plasmon-decay instability in direct-drive inertial confinement fusion experiments,” *Phys. Plasmas*, Vol. 16, No. 5, 2009, pp. 052701.

[74] Russell, D. A. and DuBois, D. F., "$3\omega0/2$ Radiation from the Laser-Driven Two-Plasmon Decay Instability in an Inhomogeneous Plasma," *Phys. Rev. Lett.*, Vol. 86, No. 3, jan 2001, pp. 428–431.

[75] Boehly, T. R., Craxton, R. S., Hinterman, T. H., Kelly, J. H., Kessler, T. J., Kumpan, S. A., Letzring, S. A., McCrory, R. L., Morse, S. F. B., Seka, W., Skupsky, S., Soures, J. M., and Verdon, C. P., "The upgrade to the OMEGA laser system," *Rev. Sci. Instrum.*, Vol. 66, No. 1, 1995, pp. 508.

[76] Waxer, L.J., Kessler, T.J., Maywar, D.N., Kelly, J., McCrory, R.L., Kruschwitz, B.E., Loucks, S., Stoeckl, C., Meyerhofer, D.D., Morse, S., and Zuegel, J., "High-Energy Petawatt Capability for the Omega Laser," *Opt. Photonics News*, Vol. 16, No. 7, 2005, pp. 30.

[77] Boehly, T. R., Smalyuk, V. a., Meyerhofer, D. D., Knauer, J. P., Bradley, D. K., Craxton, R. S., Guardalben, M. J., Skupsky, S., and Kessler, T. J., "Reduction of laser imprinting using polarization smoothing on a solid-state fusion laser," *J. Appl. Phys.*, Vol. 85, No. 7, 1999, pp. 3444.

[78] Kruer, W. L., Wilks, S. C., Afeyan, B. B., and Kirkwood, R. K., "Energy transfer between crossing laser beams," *Phys. Plasmas*, Vol. 3, No. 1, 1996, pp. 382.

[79] Figueroa, H., Joshi, C., Azechi, H., Ebrahim, N. A., and Estabrook, K., "Stimulated Raman scattering, two-plasmon decay, and hot electron generation from underdense plasmas at 0.35 μm," *Phys. Fluids*, Vol. 27, No. 7, jul 1984, pp. 1887.

[80] Liu, C. S. and Rosenbluth, M. N., "Parametric decay of electromagnetic waves into two plasmons and its consequences," *Phys. Fluids*, Vol. 19, No. 7, 1976, pp. 967.

[81] Simon, A., Short, R.W., Williams, E.A., Dewandre, T., "On the inhomogeneous two-plasmon instability," *Phys. Fluids*, Vol. 26, No. 10, 1983, pp. 3107.

[82] Yan, R., Maximov, A. V., Ren, C., and Tsung, F., "Growth and Saturation of Convective Modes of the Two-Plasmon Decay Instability in Inertial Confinement Fusion," *Phys. Rev. Lett.*, Vol. 103, No. 17, oct 2009, pp. 175002.

[83] Michel, D. T., Maximov, A. V., Short, R. W., Hu, S. X., Myatt, J. F., Seka, W., Solodov, A. A., Yaakobi, B., and Froula, D. H., "Experimental Validation of the Two-Plasmon-Decay Common-Wave Process," *Phys. Rev. Lett.*, Vol. 109, No. 15, oct 2012, pp. 155007.

[84] Michel, P., Divol, L., Dewald, E., Milovich, J., Hohenberger, M., Jones, O., Hopkins, L. B., Berger, R., Kruer, W., and Moody, J., "Multibeam Stimulated Raman Scattering in Inertial Confinement Fusion Conditions," *Phys. Rev. Lett.*, Vol. 115, No. 5, 2015, pp. 055003.

[85] Stoeckl, C., Bahr, R., Yaakobi, B., Seka, W., Regan, S., Craxton, R., Delettrez, J., Short, R., Myatt, J., Maximov, A. V., and Baldis, H., "Multibeam Effects on Fast-Electron

Generation from Two-Plasmon-Decay Instability," *Phys. Rev. Lett.*, Vol. 90, No. 23, jun 2003, pp. 235002.

[86] Froula, D. H., Yaakobi, B., Hu, S. X., Chang, P.-Y., Craxton, R. S., Edgell, D. H., Follett, R., Michel, D. T., Myatt, J. F., Seka, W., Short, R. W., Solodov, A. A., and Stoeckl, C., "Saturation of the Two-Plasmon Decay Instability in Long-Scale-Length Plasmas Relevant to Direct-Drive Inertial Confinement Fusion," *Phys. Rev. Lett.*, Vol. 108, No. 16, apr 2012, pp. 165003.

[87] Froula, D. H., Michel, D. T., Igumenshchev, I. V., Hu, S. X., Yaakobi, B., Myatt, J. F., Edgell, D. H., Follett, R., Glebov, V. Y., Goncharov, V. N., Kessler, T. J., Maximov, A. V., Radha, P. B., Sangster, T. C., Seka, W., Short, R. W., Solodov, A. A., Sorce, C., and Stoeckl, C., "Laserfi?!plasma interactions in direct-drive ignition plasmas," *Plasma Phys. Control. Fusion*, Vol. 54, No. 12, dec 2012, pp. 124016.

[88] Follett, R. K., Edgell, D. H., Henchen, R. J., Hu, S. X., Katz, J., Michel, D. T., Myatt, J. F., Shaw, J., and Froula, D. H., "Direct observation of the two-plasmon-decay common plasma wave using ultraviolet Thomson scattering," *Phys. Rev. E*, Vol. 91, No. 3, 2015, pp. 1–5.

[89] Bellan, P. M., *Fundamentals of Plasma Physics*, Cambridge University Press, New York, 1st ed., 2006.

[90] Miyahara, J., Takahashi, K., Amemiya, Y., Kamiya, N., and Satow, Y., "A new type of X-ray area detector utilizing laser stimulated luminescence," *Nucl. Inst. Methods Phys. Res. A*, Vol. 246, No. 1-3, 1986, pp. 572–578.

[91] Izumi, N., Snavely, R., Gregori, G., Koch, J. A., Park, H. S., and Remington, B. A., "Application of imaging plates to x-ray imaging and spectroscopy in laser plasma experiments (invited)," *Rev. Sci. Instrum.*, Vol. 77, No. 10, 2006.

[92] Amemiya, Y., Matsushita, T., Nakagawa, A., Satow, Y., Miyahara, J., and Chikawa, J.-i., "Design and performance of an imaging plate system for X-ray diffraction study," *Nucl. Inst. Methods Phys. Res. A*, Vol. 266, No. 1-3, 1988, pp. 645–653.

[93] Maddox, B. R., Park, H. S., Remington, B. A., Izumi, N., Chen, S., Chen, C., Kimminau, G., Ali, Z., Haugh, M. J., and Ma, Q., "High-energy x-ray backlighter spectrum measurements using calibrated image plates." *Rev. Sci. Instrum.*, Vol. 82, No. 2, feb 2011, pp. 023111.

[94] Hu, S. X., Michel, D. T., Edgell, D. H., Froula, D. H., Follett, R. K., Goncharov, V. N., Myatt, J. F., Skupsky, S., and Yaakobi, B., "Hydrodynamic simulations of long-scale-length two-plasmonfi?!decay experiments at the Omega Laser Facility," *Phys. Plasmas*, Vol. 20, No. 3, 2013, pp. 032704.

[95] Follett, R. K., Delettrez, J. A., Edgell, D. H., Goncharov, V. N., Henchen, R. J., Katz, J., Michel, D. T., Myatt, J. F., Shaw, J., Solodov, A. A., Stoeckl, C., Yaakobi, B., and

Froula, D. H., “Two-plasmon decay mitigation in direct-drive inertial-confinement-fusion experiments using multilayer targets,” *Phys. Rev. Lett.*, Vol. 116, No. 15, 2016, pp. 1–6.

[96] Smalyuk, V. A., Betti, R., Delettrez, J. A., Glebov, V. Y., Meyerhofer, D. D., Radha, P. B., Regan, S. P., Sangster, T. C., Sanz, J., Seka, W., Stoeckl, C., Yaakobi, B., Frenje, J. A., Li, C. K., Petrasso, R. D., and Séguin, F. H., “Implosion Experiments using Glass Ablators for Direct-Drive Inertial Confinement Fusion,” *Phys. Rev. Lett.*, Vol. 104, No. 16, apr 2010, pp. 165002.

[97] Myatt, J. F., Vu, H. X., DuBois, D. F., Russell, D. A., Zhang, J., Short, R. W., and Maximov, A. V., “Mitigation of two-plasmon decay in direct-drive inertial confinement fusion through the manipulation of ion-acoustic and Langmuir wave damping,” *Phys. Plasmas*, Vol. 20, No. 5, 2013, pp. 052705.

[98] Vu, H. X., DuBois, D. F., Russell, D. A., and Myatt, J. F., “Hot-electron generation by ”cavitating” Langmuir turbulence in the nonlinear stage of the two-plasmon-decay instability,” *Phys. Plasmas*, Vol. 19, No. 10, 2012, pp. 102708.

[99] Solodov, A.A., Yaakobi, B., Edgell, D.H., Follett, R.K., Sorce, C., and Froula, D., “Measurements of hot-electron temperature in laser-irradiated plasmas,” *Phys. Plasmas*, Vol. 102707, 2016.

[100] Berger, M., Hubbell, J., Seltzer, S., Chang, J., Coursey, J., Sukumar, R., Z., and D.S., Olsen, K., “XCOM: Photon Cross Section Database (version 1.5),” 2010.

[101] Workman, J. and Kyrala, G. A., “Scaling of x-ray K-shell sources from laser-solid interactions,” *Proc. SPIE*, Vol. 4504, nov 2001, pp. 168–179.

[102] McCall, G. H., “Calculation of x-ray bremsstrahlung and characteristic line emission produced by a Maxwellian electron distribution,” *J. Phys. D Appl. Physics.*, Vol. 15, 1982, pp. 823–831.

[103] Drake, R., Turner, R., and Lasinski, B., “X-ray emission caused by Raman scattering in long-scale-length plasmas,” *Phys. Rev. A*, Vol. 40, No. 6, 1989.

[104] Myatt, J., Theobald, W., Delettrez, J. A., Stoeckl, C., Storm, M., Sangster, T. C., Maximov, A. V., and Short, R. W., “High-intensity laser interactions with mass-limited solid targets and implications for fast-ignition experiments on OMEGA EP,” *Phys. Plasmas*, Vol. 14, No. 5, 2007, pp. 056301.

[105] Estabrook, K. and Kruer, W. L., “Properties of Resonantly Heated Electron Distributions,” *Phys. Rev. Lett.*, Vol. 40, No. 1, 1978.

[106] Chen, C. D., King, J. A., Key, M. H., Akli, K. U., Beg, F. N., Chen, H., Freeman, R. R., Link, A., Mackinnon, S. J., MacPhee, A. G., Patel, P. K., Porkolab, M., Stephens, R. B., and Van Woerkom, L. D., “A Bremsstrahlung spectrometer using k-edge and differential filters with image plate dosimeters.” *Rev. Sci. Instrum.*, Vol. 79, No. 10, oct 2008, pp. 10E305.

[107] Glenzer, S. H., Rozmus, W., Bychenkov, V. Y., Moody, J. D., Albritton, J., Berger, R. L., Brantov, A., Foord, M. E., MacGowan, B. J., Kirkwood, R. K., Baldis, H. A., and Williams, E. A., "Anomalous absorption of high-energy green laser light in high- z plasmas." *Phys. Rev. Lett.*, Vol. 88, No. 23, 2002, pp. 235002.

[108] Bychenkov, V. Y. and Rozmus, W., "A model of anomalous absorption of laser light on ion acoustic turbulence," *Phys. Plasmas*, Vol. 24, No. 1, 2017, pp. 012701.

[109] Ivancic, S., *Channeling Experiments on OMEGA EP*, Dissertation, University of Rochester, 2015.

[110] Goodman, J. W., *Introduction to Fourier Optics*, Roberts & Co., Englewood, CO, 3rd ed., 2005.

[111] Murakami, M., Kang, Y. G., Nishihara, K., Fujioka, S., and Nishimura, H., "Ion energy spectrum of expanding laser-plasma with limited mass," *Phys. Plasmas*, Vol. 12, No. 6, 2005, pp. 062706.

[112] Drake, R. P., "Isothermal, mass-limited rarefactions in planar and spherical geometry," *Phys. Plasmas*, Vol. 18, No. 10, 2011, pp. 104506.

[113] Rosen, M. D., Phillion, D. W., Rupert, V. C., Mead, W. C., and Kruer, W. L., "The interaction of 1.06 μm laser radiation with high Z disk targets," *Phys. Fluids*, Vol. 2020, No. 1979, 1979.

[114] De Groot, J. S., Cameron, S. M., Mizuno, K., Estabrook, K. G., Drake, R. P., Kruer, W. L., and Young, P. E., "Density and temperature profiles in strongly absorbing plasma with distributed absorption," *Phys. Fluids B Plasma Phys.*, Vol. 3, No. 5, 1991, pp. 1241.

[115] *PrismSPECT Spectral Analysis Code, v. 7.1.0*, Prism Computational Sciences, Inc., Madison, WI 53711, 2013.

[116] van der Holst, B., Tóth, G., Sokolov, I. V., Powell, K. G., Holloway, J. P., Myra, E. S., Stout, Q., Adams, M. L., Morel, J. E., Karni, S., Fryxell, B., and Drake, R. P., "Crash: a Block-Adaptive-Mesh Code for Radiative Shock Hydrodynamics-Implementation and Verification," *Astrophys. J. Suppl. Ser.*, Vol. 194, No. 2, 2011, pp. 23.

[117] Da Silva, L., Barbee, Jr., T., Cauble, R., Celliers, P., Ciarlo, D., Libby, S., London, R., Matthews, D., Mrowka, S., Moreno, J., Ress, D., Trebes, J., Wan, a., and Weber, F., "Electron Density Measurements of High Density Plasmas Using Soft X-Ray Laser Interferometry," *Phys. Rev. Lett.*, Vol. 74, No. 20, 1995, pp. 3991–3994.

[118] Ress, D., Suter, L. J., Gabl, E. F., and Failor, B. H., "Plasma evolution from laser-driven gold disks . II . Computational design and analysis," Vol. 2448, No. 1990, 1996.

[119] Luciani, J. F., Mora, P., and Virmont, J., "Nonlocal heat transport due to steep temperature gradients," *Phys. Rev. Lett.*, Vol. 51, No. 18, 1983, pp. 1664–1667.

[120] Otani, K., Shigemori, K., Sakaiya, T., Fujioka, S., Sunahara, A., Nakai, M., Shiraga, H., Azechi, H., and Mima, K., "Reduction of the Rayleigh-Taylor instability growth with cocktail color irradiation," *Phys. Plasmas*, Vol. 14, No. 12, 2007.

[121] Hu, S. X., Smalyuk, V. A., Goncharov, V. N., Skupsky, S., Sangster, T. C., Meyerhofer, D. D., and Shvarts, D., "Validation of thermal-transport modeling with direct-drive, planar-foil acceleration experiments on OMEGA," *Phys. Rev. Lett.*, Vol. 101, No. 5, 2008.

[122] Sanz, J., Betti, R., Smalyuk, V. A., Olazabal-Loume, M., Drean, V., Tikhonchuk, V., Ribeyre, X., and Feugeas, J., "Radiation hydrodynamic theory of double ablation fronts in direct-drive inertial confinement fusion," *Phys. Plasmas*, Vol. 16, No. 8, 2009, pp. 082704.

[123] Drean, V., Olazabal-Loumeffi, M., Sanz, J., and Tikhonchuk, V. T., "Dynamics and stability of radiation-driven double ablation front structures," *Phys. Plasmas*, Vol. 17, No. 12, 2010, pp. 122701.

[124] Vu, H. X., DuBois, D. F., Myatt, J. F., and Russell, D. A., "Hot-electron production and suprathermal heat flux scaling with laser intensity from the two-plasmon-decay instability," *Phys. Plasmas*, Vol. 19, No. 10, 2012, pp. 102703.

[125] Zhang, J., Myatt, J. F., Short, R. W., Maximov, A. V., Vu, H. X., DuBois, D. F., and Russell, D. A., "Multiple Beam Two-Plasmon Decay: Linear Threshold to Nonlinear Saturation in Three Dimensions," *Phys. Rev. Lett.*, Vol. 113, No. 10, sep 2014, pp. 105001.

[126] Labaune, C., Baldis, H. A., Bauer, B. S., Tikhonchuk, V. T., and Laval, G., "Time-resolved measurements of secondary Langmuir waves produced by the Langmuir decay instability in a laser-produced plasma," *Phys. Plasmas*, Vol. 5, No. 1, 1998, pp. 234.

[127] Bezzerides, B., Dubois, D. F., and Rose, H. A., "Saturation of stimulated Raman scattering by the excitation of strong Langmuir turbulence," *Phys. Rev. Lett.*, Vol. 70, No. 17, 1993, pp. 2569–2572.

[128] Williams, E. A., Berger, R. L., Drake, R. P., Rubenchik, A. M., Bauer, B. S., Meyerhofer, D. D., Gaeris, A. C., and Johnston, T. W., "The frequency and damping of ion acoustic waves in hydrocarbon (CH) and twofifftionfifftspecies plasmas," *Phys. Plasmas*, Vol. 2, No. 1, jan 1995, pp. 129–138.

[129] Williams, E. A., "Convective growth of parametrically unstable modes in inhomogeneous media," *Phys. Fluids B Plasma Phys.*, Vol. 3, No. 6, 1991, pp. 1504.

[130] Afeyan, B. and Williams, E., "Stimulated Raman sidescattering with the effects of oblique incidence," *Phys. Fluids*, Vol. 28, No. 11, 1985, pp. 3397–3408.

[131] Fein, J., Holloway, J., Edgell, D., Froula, D., Keiter, P., and Drake, R., "Mitigation of hot electrons from laser-plasma instabilities in high-Z, highly ionized plasmas," .

[132] Henke, B. L., Uejio, J. Y., Stone, G. F., Dittmore, C. H., and Fujiwara, F. G., "High-energy x-ray response of photographic films: models and measurement," *J. Opt. Soc. Am. A*, Vol. 3, No. 11, 1986, pp. 1540–1550.

[133] Dozier, C. M., Brown, D. B., Birks, L. S., Lyons, P. B., and Benjamin, R. F., "Sensitivity of x-ray film. II. Kodak No-Screen film in the 1-100-keV region," *J. Appl. Phys.*, Vol. 47, No. 8, 1976, pp. 3732.

[134] Kyrala, G. A., "Cross calibration of AGFA-D7 x-ray film against direct exposure film from 2 to 8.5 keV using laser generated x-rays," *Rev. Sci. Instrum.*, Vol. 77, No. 5, 2006, pp. 055104.

[135] Kirkpatrick, P., "On the theory and use of Ross filters," *Rev. Sci. Instrum.*, Vol. 10, No. 6, 1939, pp. 186–191.

[136] Tierney, Thomas E, Swift, Damian C, Vigil, Billy N, Paisley, Dennis L, Luo, S.-N., Johnson, R. P., and Letzring, S. A., "Temporally-resolved, area-imaged velocimeter system for dynamic materials experiments," *Proc. SPIE*, Vol. 5920, 2005.

[137] Stutman, D. and Finkenthal, M., "Talbot-Lau x-ray interferometry for high energy density plasma diagnostic," *Rev. Sci. Instrum.*, Vol. 82, No. 11, 2011, pp. 113508.

[138] Valdivia, M. P., Stutman, D., and Finkenthal, M., "Moiré deflectometry using the Talbot-Lau interferometer as refraction diagnostic for High Energy Density plasmas at energies below 10 keV," *Rev. Sci. Instrum.*, Vol. 85, No. 7, 2014, pp. 073702.

[139] Malamud, G., Di Stefano, C. A., Elbaz, Y., Huntington, C. M., Kuranz, C. C., Keiter, P. A., and Drake, R. P., "A design of a two-dimensional, multimode RM experiment on OMEGA-EP," *High Energy Density Phys.*, Vol. 9, No. 1, 2013, pp. 122–131.

[140] Johnson, L. C. and Chu, T. K., "Measurements of electron density evolution and beam self-focusing in a laser-produced plasma," *Phys. Rev. Lett.*, Vol. 32, No. 10, 1974, pp. 517–520.

[141] Young, P. E., Baldis, H. A., Drake, R. P., Campbell, E. M., and Estabrook, K. G., "Direct evidence of pondermotive filamentation in la laser-produced plasma," *Phys. Rev. Lett.*, Vol. 61, No. 20, 1988, pp. 2336–2339.

[142] Labaune, C., Baton, S., Jalinaud, T., Baldis, H. A., and Pesme, D., "Filamentation in long scale length plasmas: Experimental evidence and effects of laser spatial incoherence," *Phys. Fluids B Plasma Phys.*, Vol. 4, No. 7, 1992, pp. 2224.